

Ph.D. DISSERTATION

**Investigation of image quality optimization methods for
Positron Emission Tomography in hybrid medical
imaging**

**Áron Krisztián Krizsán
Supervisor: László Balkay PhD**



UNIVERSITY OF DEBRECEN

DOCTORAL SCHOOL OF MOLECULAR MEDICINE

Debrecen, 2016

1. Contents	Page
2. Abbreviations	4
3. Introduction	5
4. Theoretical background	10
4.1 Technical advancements of PET	10
4.2 PET performance parameters	14
4.2.1 Spatial Resolution	14
4.2.2 System sensitivity	16
4.2.3 Coincidence time window.....	17
4.2.4 Count rates and attenuation.....	18
4.2.5 Recovery Coefficient and Spill Over Ratio	20
4.2.6 Image Contrast	21
4.3 Quantitative PET	22
4.4 Signal to Noise Ratio (SNR) of PET/CT and PET/MRI	24
5. Aims	29
6. Materials and Methods	30
6.1 Performance Comparison of the MiniPET-2 and MiniPET-3 preclinical PET systems	30
6.1.1 Scanner Description	30
6.1.2 Position encoding and energy resolution evaluation	33
6.1.3 Coincidence Time Window Optimization	33
6.1.4 Spatial Resolution Measurement	34
6.1.5 Sensitivity Measurement.....	35
6.1.6 Image Quality Phantom Study	35
6.1.7 Scatter Fraction and Count Rate Performances	36
6.1.8 Small Animal Studies	36
6.2 Human brain PET scanner simulation based on MiniPET concept	36
6.2.1 The GATE simulation environment.....	38
6.2.2 Definition of the scanner geometry.....	38
6.2.3 Simulation of position maps and energy resolution.....	38
6.2.4 Simulation of the count rate capability and system sensitivity	39
6.3 Whole body PET image SNR optimization using variable acquisition times ...	39
6.3.1 PET/CT System	39
6.3.2 SNR Simulations.....	39
6.3.3 Acquisition Time Adjustment.....	40
6.3.4 Phantom and Patient Scans	41
7. Results	43
7.1 Performance Comparison of the MiniPET-2 and MiniPET-3 preclinical PET systems	43
7.1.1 Position encoding and energy resolution	43
7.1.2 Coincidence Time Window	44
7.1.3 Spatial Resolution and Sensitivity	45
7.1.4 Image Quality, Scatter Fraction and Count Rates.....	47
7.1.5 Small Animal Imaging Results	49
7.2 Human brain PET scanner simulation based on MiniPET concepts	49
7.2.1 Position maps and energy resolution	49
7.2.2 System count rate and sensitivity.....	50
7.3 Whole body PET image SNR optimization using variable acquisition times ...	52
7.3.1 Simulations	52
7.3.2 Phantom and Patient Scans	54
8. Discussion	58

9. Summary	62
10. Acknowledgements	63
11. Keywords	64
11. References	65
12. Online references	73
13. List of publications that serve as the basis of this dissertation.....	74
14. List of other publications	75
15. List of further publications and abstracts.....	76
16. Prints of publications that serve as the basis of this dissertation.....	78

2. Abbreviations

APD: *Avalanche Photodiodes*

CT: *Computer Tomography*

CT-AC: *CT Attenuation Correction*

FBP: *Filtered Backprojection*

FMT: *Fluorescence Molecular Tomography*

FOV: *Field Of View*

FPGA: *Field Programmable Gate Array*

FRI: *Fluorescence Reflectance Imaging*

FWHM: *Full Width at Half Maximum*

LOR: *Line Of Response*

LSO: *Lutetium Oxyorthosilicate*

LYSO: *Lutetium-Yttrium Oxyorthosilicate*

M3I: *MultiModal Medical Imaging*

ML-EM: *Maximum Likelihood Expectation Maximization*

MRI: *Magnetic Resonance Imaging*

NEC: *Noise Equivalent Count*

NEMA: *National Electrical Manufacturers Association*

OI: *Optical Imaging*

OSEM: *Ordered Subsets Expectation Maximization*

PET: *Positron Emission Tomography*

PMT: *Photomultiplier Tube*

PSF: *Point Spread Function*

PVC: *Partial Volume Correction*

PVE: *Partial Volume Effect*

RC: *Recovery Coefficient*

saPET: *Small Animal PET*

SiPM: *Silicon Photomultiplier*

SNR: *Signal to Noise Ratio*

SOR: *Spill Over Ratio*

SPECT: *Single Photon Emission Computer Tomography*

SSRB: *Single-Slice Rebinning*

SD: *Standard Deviation*

TOF: *Time Of Flight*

UCLA: *University of California at Los Angeles*

US: *Ultra Sound*

3. Introduction

Positron Emission Tomography (PET) is a non-invasive functional imaging method that has become widely used in the nuclear medicine field during the last three decades. PET incorporates the unique characteristics of radionuclides decay with positron emission. Such radionuclides are usually produced in a cyclotron and then used to label a medically interested molecule for the purpose of tracing its metabolism processes. Therefore, these labeled molecules are frequently called radiotracers. The labeled molecules (typically 10^{13} – 10^{14}) are introduced into the body by intravenous injection and distributed according to the same metabolism as the non-labeled compounds [1]. When a positron is ejected from a radionuclide following β^+ decay, it loses kinetic energy by inelastic interactions with atomic electrons. Then a temporary particle called positronium is formed with a final electron. This is followed by the annihilation process, while the mass of the positron and the electron is converted into two 511 keV γ -photons, which are emitted simultaneously at about 180 degrees with respect to each other [2]. When both γ -photons are detected in the scintillation crystal ring surrounding the patient within a short time interval (typically 5 – 10 ns), the scanner registers a line-of-response (LOR) connecting the two signaling detectors. These unique decay characteristics make it possible to reject those coincidence photon detections that are occurring outside of this time limit; hence their origin was not the same positron emission. From the useful signals the scanner makes corrections for many distortion effects (Attenuation, Scattered- and Random coincidences) and then reconstructs the images using mathematical iterative algorithms. The reconstructed images represent the distribution of the radioactive labeled molecules in the body of the patient; and therefore, give information on the metabolism of these compounds.

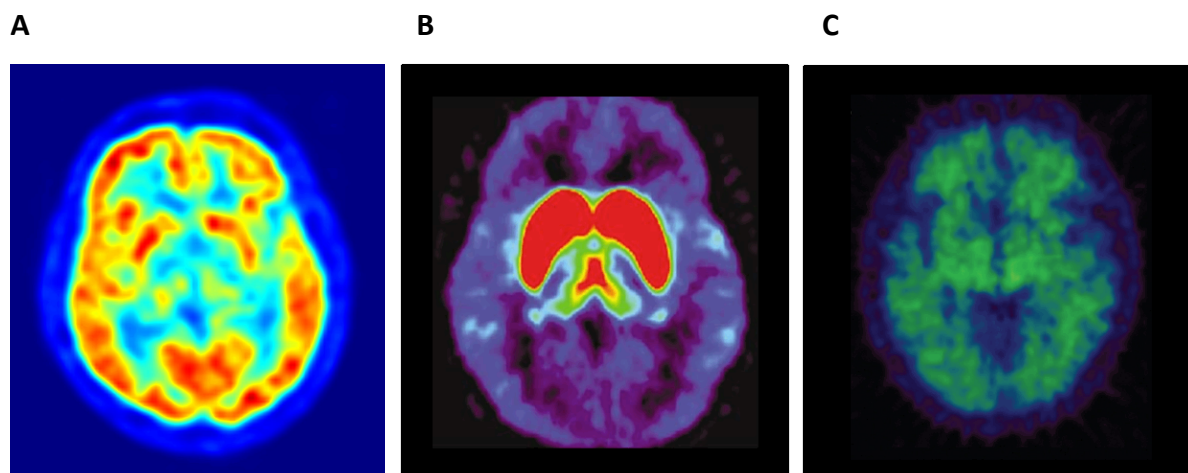


Figure 1. PET images with different radiotracers: (A) ^{18}F -FDG uptake in the normal brain showing glucose accumulation in the gray matter [http1]; (B) ^{18}F -Fallypride uptake in the normal brain indicating dopamine D2 receptors in the striatum [3]; (C) ^{11}C -PiB of a healthy individual with low signal owing to little or no specific binding to amyloid- β [http2]. In case of Alzheimer disease, pathological uptake could be seen with this radiotracer.

Based on the biological interest, a large variability of organic molecules is possible to be labeled and therefore different biological metabolisms could be followed even in the same patient. However, these measurements could not be performed simultaneously just in separate scans, since the positron annihilation characteristics are closely alike for the different radiotracers. As examples of these, representative normal brain PET images are displayed in Figure 1. with different radiotracers including ^{18}F -FDG, ^{18}F -Fallypride and ^{11}C -PiB. These images reveal also the potential of the method to track a variety of metabolism processes even in the healthy body. Furthermore, an important characteristic of PET is that the method is quantitative. If the scanner is correctly calibrated and all necessary corrections on the raw data are performed (Detector normalization, Attenuation-, Scatter- and Random corrections), the image pixel or voxel¹ units (counts per second per pixel) could be converted to activity concentration units (kBq/ml). This information is then used to detect pathological uptakes and plan on the appropriate therapy. All of these characteristics fostered the capabilities of PET to be one of the leading functional imaging techniques. While both anatomical and functional imaging techniques had many developments in the last two decades, the demand of using PET in hybrid imaging was rising.



Figure 2. PET/CT study of 44-y-old man (BMI=16) with recent diagnosis of lung cancer. The images demonstrated multiple bilateral pulmonary nodules, including medial right upper lobe nodule surrounding pulmonary vessels on the PET (A), and capability of combining functional images of ^{18}F -FDG to the accurate anatomical images of CT (B).

For the clinical applications, the concept of combining imaging techniques in a single hybrid device promised many advantages since PET has outstanding sensitivity ($\sim 10^{-12}$ mol/L), while CT or MRI provides excellent spatial resolution (~ 0.5 mm). However, before the arrival of the first PET/CT system in 2000, much skepticism existed about the clinical

¹ A pixel is the 2D plane image element and a voxel is similarly a 3D volume element of the image. Within a pixel or a voxel the image intensity is uniform.

workflows and the too long scans, the high expense of PET/CT scanners. It was also questionable, that two physicians would read the images as patient data result in two reports, while the inclusion of CT could lead to unnecessary extra radiation and that CT attenuation correction (CT-AC) would lead to significant artifacts. The realism after 15 years reveal that the overall PET/CT costs are comparable than PET only, combined PET/CT scans can be performed in about 15 – 25 minutes, many physicians are dual-boarded and usually write a single report, clinics use standard low-dose CT protocols and optimized CT-AC is used routinely. The introduction of PET/CT induced the use of PET to be expanded as well. In approximately five years after the introduction of PET/CT, the PET only examinations decreased with 40%, while the total number of PET scans increased with 90% for 5 university PET centers in Germany only [4]. As mentioned above, the use of PET/CT had many effects on the clinical protocols as well in terms of scanning time since the CT derived attenuation correction is much easier shorter than the conventional rotating source methods [5],[6].

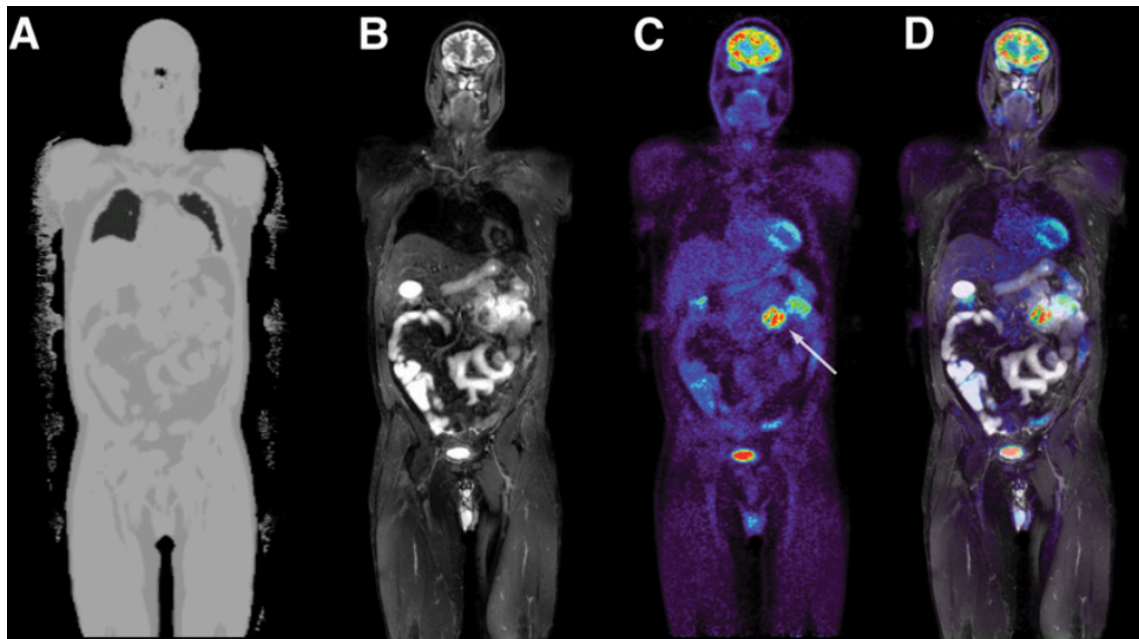


Figure 3. PET/MR image of patient with enteric melanoma metastasis (arrow): MR-based attenuation map (A), T2-weighted short- τ inversion recovery sequence (B), ^{18}F -FDG PET image (C), and PET overlaid on short- τ inversion recovery image (D). Data were acquired on a Biograph mMR system [7].

While the use of PET/CT has been already reached worldwide, the concept of combining PET with MRI revealed greater challenges on both the engineering and clinical sides. After more than ten years of development, focusing greatly on new PET photo-detector technology and the hardware integration of a PET scanner into an MRI system, PET/MRI has recently rapidly emerged from the first prototype systems into clinical scanners [7]. Various integrated systems have recently been introduced to provide improved clinical assessments of cancers in case of soft tissues that give better image contrast with

MRI imaging than with CT. PET/MRI may also reduce radiation exposure for patients, especially for children and women of child-bearing age [8]. In addition to the many developments focusing on the scanning protocols of the hybrid imaging systems (e.g. PET/CT and PET/MRI) there is still room for optimization even on the acquisition time and image quality. The inclusion of CT or MRI gave challenges but promising features as well and the improvement of PET image quality in the last decade is remarkable.

For the comparison of the PET imaging devices an international standard is needed including performance measurements (e.g. System Sensitivity, Scatter Fraction, True- and Random Coincidence Rate, Noise Equivalent Count Rate) and imaging capabilities (e.g. Spatial Resolution, Recovery Coefficients, Spill over Ratios, Image Uniformity, Signal to Noise Ratio). For standardization purposes and to be able to compare nuclear medicine imaging systems the National Electrical Manufacturers Association (NEMA) recommendation became a gold standard worldwide in the last years (NEMA NU 1 for SPECT cameras, NEMA NU 2 for PET cameras).

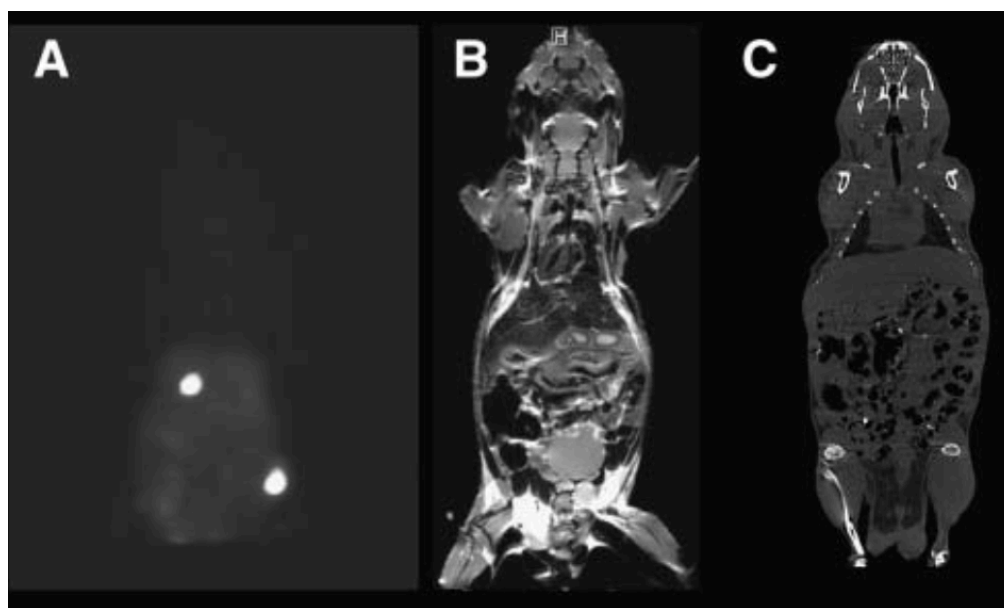


Figure 4. (A) Functional information at highest sensitivity is provided by PET images. (B) MRI provides superior anatomic information with excellent soft-tissue contrast. (C) High-resolution animal CT also provides good anatomic information but has poorer soft-tissue contrast and requires significant radiation dose [9].

Along with the developments of hybrid systems, in the last fifteen years many dedicated PET scanner concepts were also arrived for human breast imaging called Positron Emission Mammography (PEM) and for preclinical drug research called small animal PET (saPET) or preclinical PET. The first commercially available full ring preclinical PET camera, the Concorde microPET was designed and developed at the University of California at Los Angeles. In those years the determination of imaging characteristics for preclinical PET systems was possible only by a specific application of the NEMA standard of human

PET systems. A strong demand was rising for a standardization of measurements that are essential for preclinical PET cameras. The imaging capabilities and the reliability of these scanners are important issues in the preclinical PET field and the main steps to gain this information were finally introduced as the NEMA NU 4 guideline in 2008. This recommendation includes a group of measurements that are used as a gold standard for comparison of performance and imaging capabilities of preclinical PET scanners [10]–[14].

A new preclinical PET scanner, the MiniPET-3, was developed at our institutions recently, based on the former gantry parameters of MiniPET-2 [14] with Lutetium-Yttrium Oxyorthosilicate (LYSO) crystal detectors. However, the conventional PMT photo-detectors of MiniPET-2 were replaced with new SiPM technology (ST Microelectronics) in the MiniPET-3. In addition, the readout boards have been slightly altered in terms of signal encoding of SiPM and PMT, while the scintillation crystal geometry in the gantry remained the same for both systems. Since the only significant difference between the two scanners is the photo-detector technology, the systems provide us the possibility to compare the imaging capabilities and system performance of the new MRI compatible SiPM photo-sensors (on the MiniPET-3) and the conventional PMTs (on the MiniPET-2).

4. Theoretical background

4.1 Technical advancements of PET

Positron Emission Tomography (PET) is a molecular imaging technique that was invented in the end of the 1970s. After some initial approaches of other scientists [17]–[23], a research group from Washington University School of Medicine in St. Louis including Michael E. Phelps, Edward J. Hoffman, Nizar A. Mullani, and Michel M. Ter-Pogossian introduced the first full ring tomographic equipment using annihilation coincidence detection from a positron emitter. They reported on the performance of the scanner and the imaging of a living animal [24]. After many developments, PET became an important clinical investigation method for oncology and brain studies during the following years. The concept of Whole Body PET was first proposed by scientists of the University of California at Los Angeles in the beginning of the 1990s [25] (Figure 5. Panel A). Whole Body PET images are typically acquired as a series of image sets collected at discrete axial positions that covers most or all of the body. These image sets are then reconstructed and assembled into a 3-D image volume that can be viewed as transaxial, coronal, or sagittal images. PET

Table 1. Comparison of Medical Imaging Technologies [15], [16].

Imaging Modality	Spatial Resolution	Temporal Resolution	Sensitivity (mol/L)	Quantitative	Target
PET	1 – 2 mm	sec – min	$10^{-11} - 10^{-12}$	yes	Physiological, molecular
SPECT	0.3 – 1 mm	min	$10^{-10} - 10^{-11}$	yes	Physiological, molecular
Optical					
Bioluminescence	3 – 5 mm	sec – min	$10^{-15} - 10^{-17}$	no	Molecular
FRI	2 – 3 mm	sec – min	$10^{-9} - 10^{-12}$	no	Physiological, molecular
FMT	1 – 3 mm	min	$10^{-6} - 10^{-12}$	yes	Physiological, molecular
MRI	10 – 250 μm	min - hours	$10^{-3} - 10^{-5}$	yes	Anatomical, physiological, molecular
CT	25 – 150 μm	sec – min	-	relative	Anatomical, physiological
X-ray	25 – 150 μm	sec	-	no	Anatomical
Ultrasound	30 – 500 μm	sec – min	$10^{-6} - 10^{-9}$	yes	Anatomical, physiological

FRI indicates fluorescence reflectance imaging; FMT, Fluorescence molecular tomography

has an inferior spatial resolution compared to CT or MRI in the range between 1 mm and 4 mm (FWHM: full width at half maximum) depending mainly on the detector ring diameter. However, PET scanners have superior sensitivity compared to these imaging techniques or even to Single Photon Emission Computer Tomography (SPECT) in the range of 10^{-11} – 10^{-12} mol/L [15], [16]. A detailed comparison with SPECT, CT, MRI, X-ray, ultra sound (US) and optical imaging (OI) including temporal resolution, medical target is displayed in Table 2 [15].

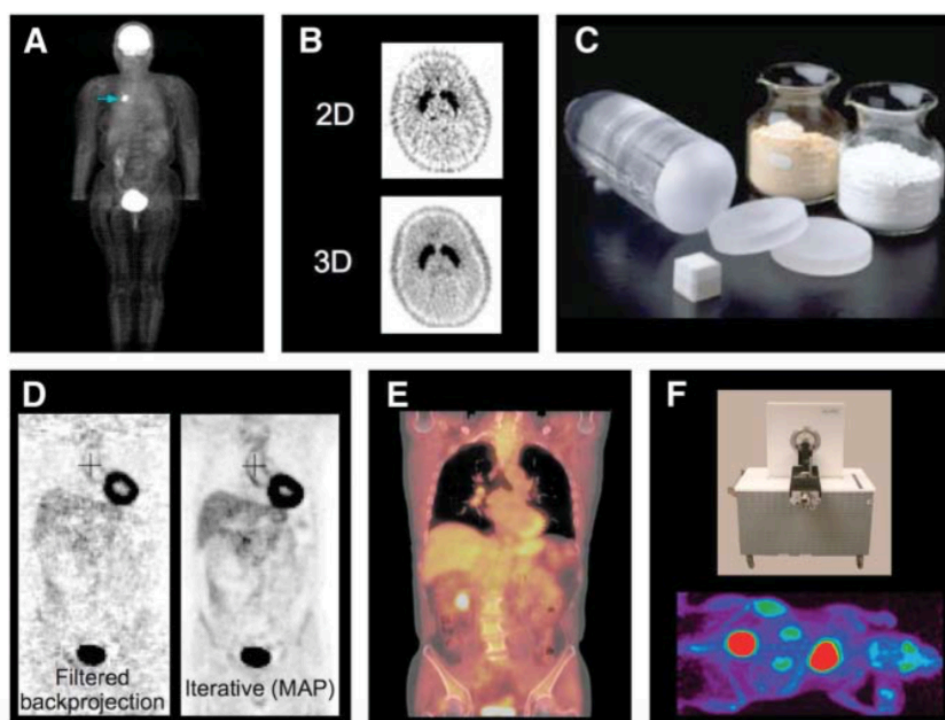


Figure 5. Some major advances in PET instrumentation and methods since the arrival of whole-body PET (A), 3D PET (B), LSO and related scintillators (C), iterative reconstruction methods (D), PET/CT (E), and preclinical PET (F) [26].

In the last two decades, PET went through numerous developments, while image quality was improved and patient scanning protocols were optimized. The conventional 2D image acquisition protocol was changed to a fully 3D acquisition with the removal of septa used between the detector rings (Figure 5. Panel B). This resulted in an increase of sensitivity of about an order of magnitude [1], however the random- and scatter rates are increased significantly as well. In terms of detector technology the former Bismuth Germanate (BGO) scintillation crystals were replaced with faster Luthetium Oxy-ortho Silicium (LSO) or Luthetium Yttrium Oxy-ortho Silicium (LYSO) crystals in almost every PET systems (Figure 5. Panel C). LSO and LYSO have an approximately triple times greater light yield and seven times faster decay time compared to BGO. There have been many improvements in the reconstruction methods of the raw data acquired during the PET acquisitions (Figure 5. Panel D). The raw data of PET measurements was formerly binned into an angle and offset representation of the LORs called sinogram. Today in many cases the camera uses list-mode data acquisition and 3D LOR binning without the production of

sinograms. The PET raw data was reconstructed using Filtered Back Projection (FBP) in the past. However, for better image quality of the relatively few events in PET imaging (e.g. compared to CT), iterative reconstruction algorithms were introduced such as the Maximum Likelihood Expectation Maximization (ML-EM). The more faster method using subsets of the list-mode raw data the Ordered Subsets Expectation Maximization (OSEM) reconstruction was also introduced [27]. Reconstructions combining expectation maximization and a-priori information were also investigated and tested [28]. We already mentioned the developments of hybrid PET/CT and preclinical PET imaging (Figure 5. Panel E and F) in the Introduction chapter.

For many years Time-Of-Flight (TOF) information was proposed to receive better coincidence detection and improved signal to noise ratio, however detector technology was not sufficient in terms of timing resolution to incorporate the idea.

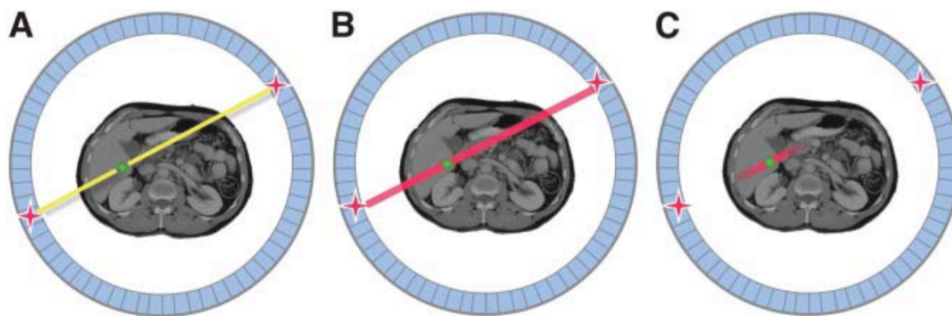


Figure 6. The concept of TOF: In the conventional method true coincidence occurs along an LOR (A), while a uniform probability weighting is applied during reconstruction (B). With TOF information used in the reconstruction, the probability weighting is more focused around the annihilation site (C) [26].

In the conventional method a uniform probability line is used along the LOR connecting the two detectors in which the coincidence occurred. By using the measured time difference between the arrivals of the two gamma photons (that belong to the same coincidence event), this time information can contribute to the image reconstruction as a probability-weighting kernel on the site of the annihilation. The very basic idea of TOF is displayed in Figure 6. The first concept of TOF PET was mentioned by Hall O. Anger in 1966 [29] and after many concepts and predictions a summary on TOF PET was written by Budinger in 1983 [30]. During the period of active research and development, more than two decades of advent the first clinically available concepts arrived. In 2007 Surti et al. published on the performance of the first clinically available TOF-PET, the Gemini TF PET/CT system [31].

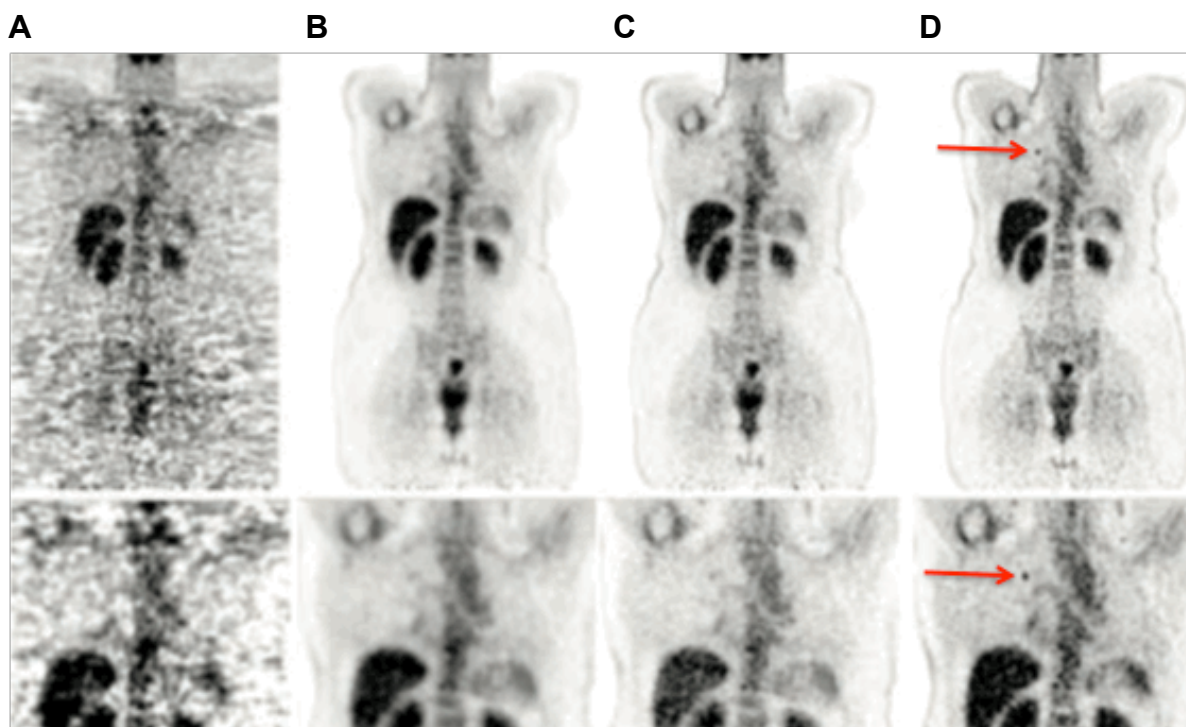


Figure 7. Different reconstruction algorithms using the very same list-mode raw data: Filtered Backprojections (A), 3D Iterative (B), 3D Iterative + PSF correction (C), 3D Iterative + PSF correction + TOF (D). The red arrows show the significant benefit from TOF and PSF correction: the improved Signal to Noise Ratio allows a clear interpretation of a lung lesion that unsure on the image set of the conventional method.

The point spread effect causes spatial resolution distortion towards the radial edges of the images. Benefits of point spread function (PSF) correction used in the reconstruction process combined with TOF information on several image quality parameters has been also reported [32]–[36]. Demonstration of the improvements provided by TOF and PSF correction on images using the very same list mode raw data is displayed in Figure 7. Another limiting factor, the partial volume effect (PVE) results in suppressed signal for objects smaller than three times the spatial resolution (FWHM). Partial volume correction (PVC) can be used to improve brain and myocardial images, as well as the quantitative accuracy of tumor tissue images [37], [38].

For many years researchers and clinicians had doubts and hopes about the arrival of PET systems combined with CT or MRI. The first approach to combine PET with a CT was developed by Teruo Negai and his colleagues at the Department of Radiology, Gunma University in Japan in 1984. The device incorporated a CT and a PET scanner (Hitachi Inc.) and the patient bed moved on floor-mounted rails between the PET and CT. This initial device was used in the daily clinical routine, and therefore this scanner should be called the first hybrid PET/CT system. Without knowing the existence of this combined scanner, researchers at the University of Pittsburgh and at CTI PET Systems developed an integrated PET/CT scanner and published their findings on the system performance and clinical studies [39]. After the introduction of the first clinical hybrid PET/CT system, these devices became used worldwide. With PET/CT the clinical protocols changed as well: a PET scan took at

about 45 minutes in a PET-alone scanner because of the lower sensitivity and the rotating positron source used for attenuation correction. A total combined scan takes about 15-25 minutes in a PET/CT scanner while optimized CT-based attenuation correction is used routinely. In the years of hybrid PET/CT systems there have been many more attempts to optimize the scanning protocols. Higher PET sensitivity and less bed positions to cover the same length of the body became available by using wider axial field of view [40]. Respiration gating PET by belt or infrared light methods resulted in less motion artifacts were observed, especially in case of thorax images. The acquisition time plays a very important role in the patient protocols. Many optimizations were focused on the impact of patient weight and emission scan duration, comparison of protocols on administered dose versus scan duration, as well as optimizing imaging protocols for overweight and obese patients. As mentioned above, for proper clinical protocols it is critical to use radionuclides that have half-life short enough to decay away quickly after the patient examination but long enough to do not decay significantly during the time of the PET acquisition. Some radionuclides that meet these criteria are listed in Table 2. along with their physical properties (such as branching fraction, positron range) and the radiotracers they have been labeled with.

Table 2. Positron emitter radioisotopes useful for PET imaging and some important characteristics: half-life, maximum positron energy, positron range and radiotracer applications [1] [41].

Radioisotope	Half-life	Maximum positron energy (MeV)	Positron range FWHM (mm)	Radiotracers
¹⁸ F	109.8 min	0.63	0.54	¹⁸ F-FDG, Na ¹⁸ F, ¹⁸ F-Fallypride
¹¹ C	20.4 min	0.96	0.92	¹¹ CO ₂ , ¹¹ CO, ¹¹ C-Methionin
¹³ N	9.97 min	1.20	1.49	¹³ NH ₃ , ¹³ N ₂
¹⁵ O	122 sec	1.73	2.48	¹⁵ O ₂ , C ¹⁵ O ₂ , C ¹⁵ O
⁶⁸ Ga	67.6 min	1.89	2.83	⁶⁸ Ga-DOTATATE, ⁶⁸ Ga-BAPEN

4.2 PET performance parameters

4.2.1 Spatial Resolution

At any imaging system the spatial resolution term is basically tend to express the best ability in distinguishing two separate target points from each other (peak-to-peak resolution). However, among some other imaging modalities, in the PET field the measurement definition is the full-width-at-half-maximum value (FWHM) on the profile

curve of a single activity point source. There are several physics factors that have an impact on the spatial resolution of the scanner, such as positron range (r), non-colinearity ($0.0022 \times D$, where D is the ring diameter), crystal pitch (d), position map coding uncertainty (b), parallax error (p) and the reconstruction method (k). These contribute to the final FWHM with a square root function as showed in Equation 1.

$$FWHM = k \times \sqrt{\left(\frac{d}{2}\right)^2 + b^2 + (0.0022 \times D)^2 + r^2 + p^2} \quad \text{Eq. 1}$$

Crystal pitch means the width of a single crystal including the width of the reflective material between the crystals. The parallax error is a mispositioning of events caused by the lack of information on depth of interaction (DOI) for photons penetrating the scintillation crystals. This smearing effect results in the widening of PSF and more prominent towards the radial edges of the FOV [1]. The reason of this error originates from the wider scintillation crystal coverage of a certain LOR as it can be observed in Figure 8.

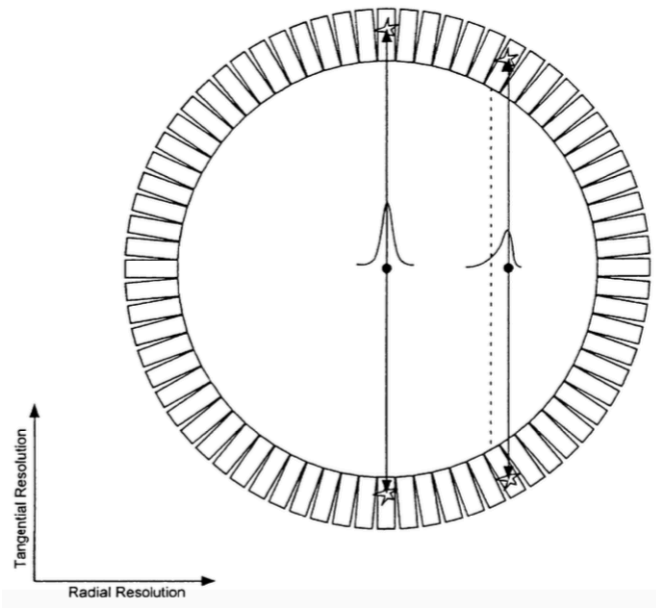


Figure 8. For the ring geometry scanners the point spread function becomes asymmetrical in case of increasing radial offset [1].

In case of ^{18}F studies probably the greatest contribution is from the non-colinearity, which means that the gamma photons fly apart not exactly 180 degrees with respect to each other. This effect is the result of the annihilation process, where the velocity of the positron is not exactly zero. The non-colinearity is more emphasized when the scanner ring diameter (D) is wider. The effects of three factors from those mentioned above (positron range, non-colinearity, crystal scatter) are displayed in Figure 9 in case of two scenarios: an 80 cm diameter human- and an 8 cm diameter small animal PET scanner [26].

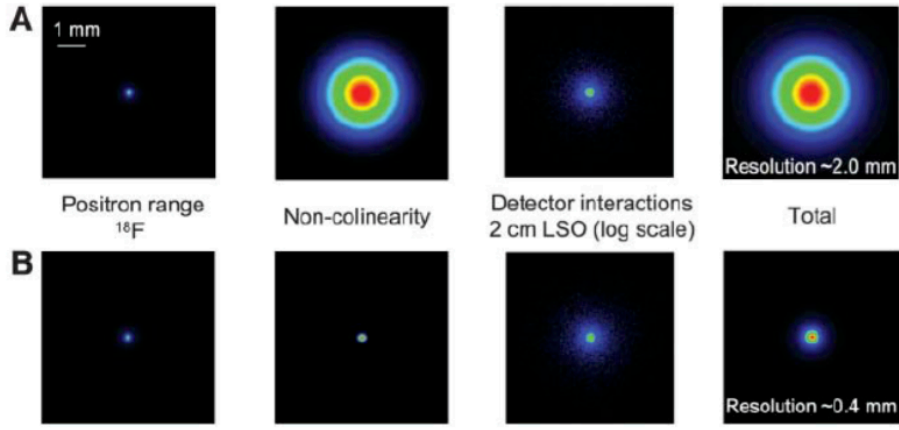


Figure 9. Simulation of a clinical PET scanner with diameter of 80 cm (A) and a small animal PET scanner with a diameter of 8 cm both consisting of 2 cm thick LSO detector crystals and imaging the same size ^{18}F point-source. In each case, the effects of positron range, non-colinearity and detector scatter are shown separately and together as well. It can be observed, that the effect of non-colinearity is very sensitive to the detector diameter, and thus it gives a limiting factor for the achievable minimal spatial resolution in case of the human PET scanners [26].

It is not evident why almost all of the annihilations are resulted in two γ -photons that can be detected by the PET system. In terms of spin orientations two types of positroniums can be formed: ortho- (o-Ps) and para-positroniums (p-Ps). The o-Ps has a higher ratio of 3:1, and while p-Ps results in an even number of photons the o-Ps results in odd number photons [42]. The two types of positroniums have significantly different decay times in vacuum and therefore the lifetime (the inverse of the decay rates) is about 125 ps for p-Ps and about 142 ns for o-Ps. The formed p-Ps is observed to decay in liquids with the vacuum lifetime. However, the lifetime of o-Ps measured in liquids is considerably shorter than its vacuum value due to the so-called pick-off annihilation. During this pick-off annihilation an opposed spin second electron reacts with the o-Ps resulting in a two-photon annihilation. Furthermore, the pick-off rate is influenced by the dissolved gases, and decreasing in the presence of oxygen. As a result of the effects mentioned above the observed lifetime of o-Ps in water is 1800 ps compared to the much longer vacuum lifetime of 140 ns. Thus, we can state that most annihilations in tissue result in a useful two-gamma ray emission despite the larger amount of o-Ps that is initially formed.

4.2.2 System sensitivity

Sensitivity (η) of a positron emission tomography is defined as a function of solid angle (Ω), packing fraction (φ), and the detection efficiency (ϵ) as follows:

$$\eta = 100 \times \frac{\epsilon^2 \varphi \Omega}{4\pi} \quad \text{Eq. 2.}$$

The detector efficiency is a product of the fraction of events (Φ) fall into the energy window and the detection probability of the incoming photon in a single detector element:

$$\varepsilon = (1 - e^{-\mu d}) \times \Phi \quad \text{Eq. 3}$$

The packing fraction describes the crystal geometry and pitch using the axial width and height of the scintillation crystal element as follows:

$$\varphi = \frac{\text{width} \times \text{height}}{(\text{width} + \text{deadspace}) \times (\text{height} + \text{deadspace})} \quad \text{Eq. 4.}$$

The solid angle coverage determines the geometrical efficiency and in case of a ring scanner using a point source in the center of the FOV defined as:

$$\Omega = 4\pi \sin [\tan^{-1}(A/D)] \quad \text{Eq. 5}$$

where D is the diameter of the scanner and A depends on the maximal acceptance angle in the axial direction over which data is collected [1]. Almost every recent PET scanners have a 3D imaging mode, which means all axial cross planes are used for the coincidence detection. This greatly improves sensitivity, but also causes the triangle shape axial sensitivity profile displayed in Figure 10.

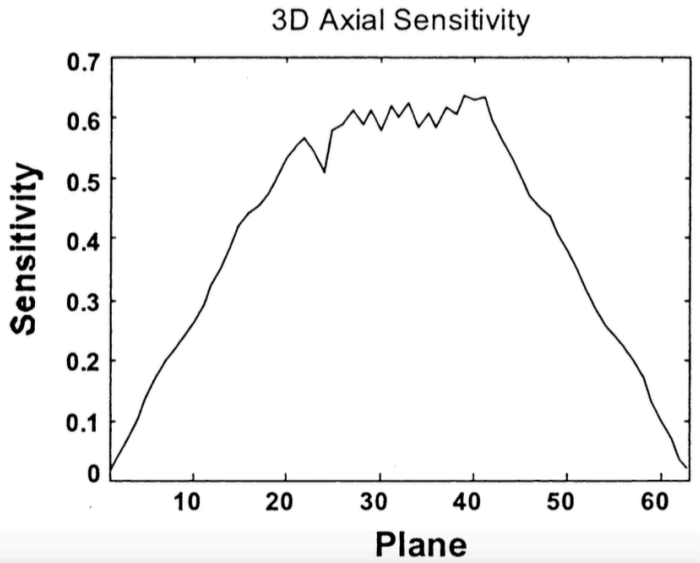


Figure 10. Representative axial sensitivity profile of a typical PET scanner operating in 3D mode. The solid angle coverage causes a triangle shape in this imaging mode [1].

4.2.3 Coincidence time window

In PET imaging numerous performance parameters are affected by the value of τ , the coincidence time window. Aiming to find the optimal τ -value an appropriate range should be defined that is need to be involve the plateau of the true coincidence count rate (that is mainly depend on the used source activity and detection efficiency). In addition, the random count rate should be reasonably low at the optimal τ value. The coincidence time window is usually a couple times longer than the time resolution of the PET system.

4.2.4 Count rates and attenuation

The coincidence events registered during the data acquisition in a PET system are not only coming from true coincidences only, but biased by the so-called scattered and random events. The γ -photons (originating from the annihilation process) with 511 keV energy have low probability for Photoelectric-absorption (PEA) but a significant probability to go through Compton-scattering (CS) (approximately 5% PEA, 95% CS). This scatter can occur in the body changing the direction of the γ -photon while the coincidence is signed to a misleading LOR (Figure 11.) Scatter in the scintillation material may cause the detection in an adjacent crystal that leads to a misplaced LOR as well. The ration of the body scatter/crystal scatter is around 1:5 in case of small animal systems [43], while more body scatter can be detected in case of human scanners. During 3D PET acquisition, not just direct planes but many cross planes are used for coincidence detections between the detector rings. Therefore, a very large number of single γ -photons arrive in the detector ring even from sections of the body outside of the field of view. Because the coincidence time window is not infinitely narrow in case of such many single γ -photons there is a high chance for two photons to arrive during the given coincidence time window and a random coincidence event happens. Then these random events contribute to the noise level of the final images.

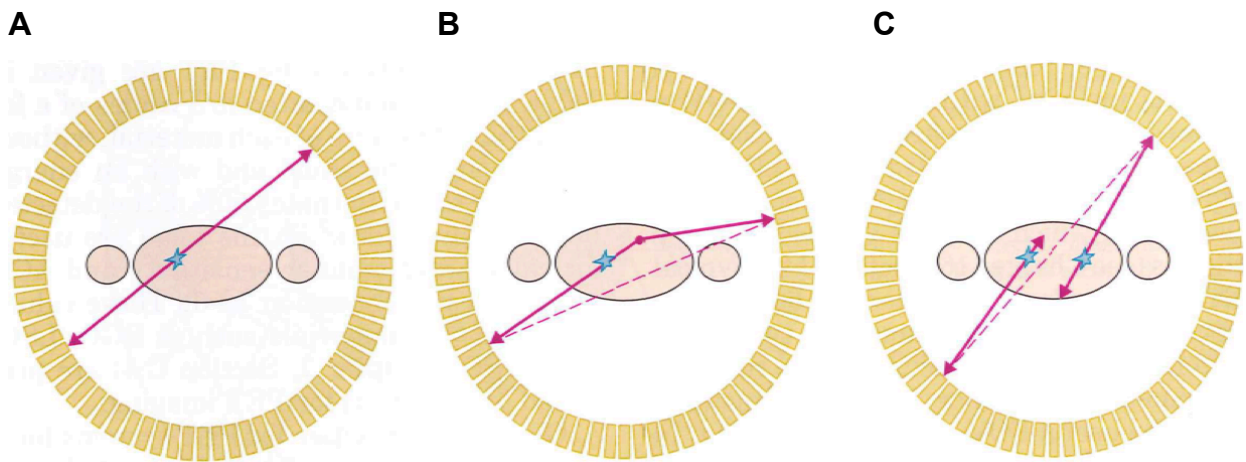


Figure 11. Schematic figures about the true (A), scatter (B) and random (C) coincidence events [44].

The final detected count rate will consist of the count rates mentioned above as:

$$M = Norm \times (Atten \times T + S + R) \quad \text{Eq. 6.}$$

where M is the measured count rate, $Norm$ is the normalization correction, $Atten$ is the attenuation effect, T is the true count rate, S is the scatter count rate and R is the Random count rate. Although, count rate measurements give important information on the performance limits of PET scanners, they do not directly indicate image signal-to-noise in

case of relatively changing trues, randoms and scatter rates. A more informative measure of signal-to-noise can be provided by the *noise equivalent count rate* (NEC).

$$NEC = \frac{T^2}{T+S+2fR} \quad \text{Eq. 7.}$$

where f is the fraction of the sinogram covered by the phantom region and the factor of 2 comes from the random subtraction method. The Random events, Attenuation and Compton-scatter will result in a distorted PET signal and therefore has a great impact on the image data. Because of the geometry of the patient, these interactions will cause severe attenuation that is more prominent in the inner parts of the body and lower at the surface. As discussed above, the results of these interactions are the removal of primary photons from a given LOR and the potential detection of scattered photons in a different LOR. Thus, attenuation and scatter are side effects of the same physical process. Corrections are necessary and include removing scattered events from the LORs. Moreover, it is needed to subsequently correct each LOR for the fraction of events missing from that LOR.

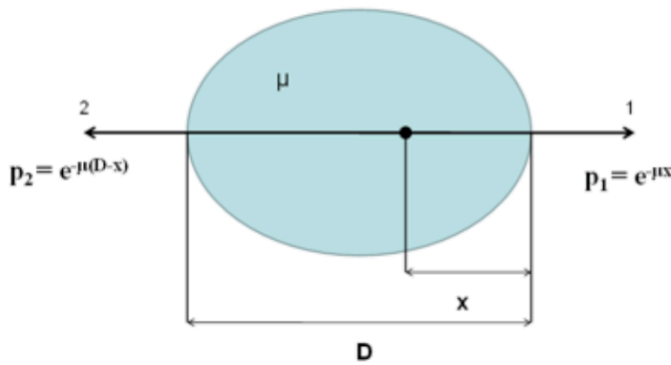


Figure 12. Attenuation probability of a given LOR: because of the coincidence detection, the probability of the detection of both photons ($p = p_1 * p_2$) depends on the attenuation coefficient (μ) and the diameter (D) along the LOR and independent from the distance of the annihilation site from the surface (x).

The probability of a γ -photon to escape the body depends on the distance between the annihilation site and the surface (x) multiplied by the attenuation coefficient of the tissue (μ). The probability to detect both photons is the product of the individual probabilities of photons to escape the body. Therefore, only the diameter (D) of the patient along the LOR contributes to the equation (Equation 6.) of this probability regardless the distance of the annihilation site from the surface.

$$p = p_2 \times p_1 = e^{-\mu(D-x)} \times e^{-\mu x} = e^{-\mu D} \quad \text{Eq. 8.}$$

Attenuation of the signal from a given LOR can be measured with different algorithms from CT or MRI images of the same patient. This so-called μ -map is gained from a bi-linear scaling method in case of a CT images. For MRI segmentation algorithms are used

routinely, using a Dixon sequence. The effect of attenuation and the image after attenuation correction can be observed in Figure 13. Besides the attenuation correction, detector normalization, scatter- and random corrections are performed on the raw data of the PET images.

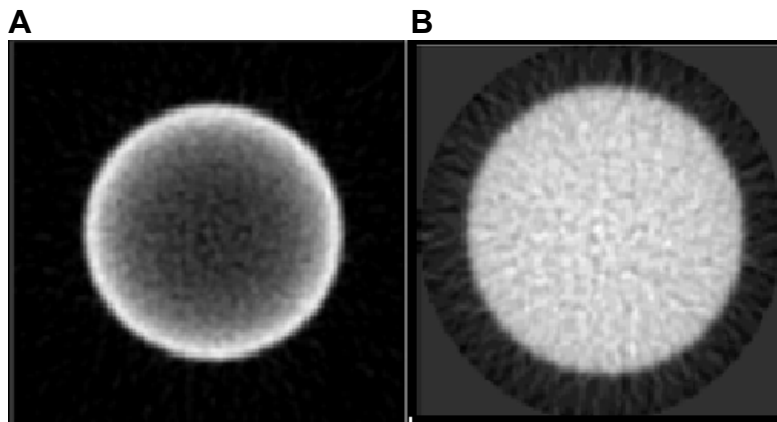


Figure 13. Uniform cylinder without (A) and with normalization, attenuation-, random- and scatter corrections (B).

The count rate protocol allows determination of the source activity dependence on the scatter rate, the random ratio and the Noise Equivalent Count (NEC) rate, that are important especially at human studies and real animal experiments. These measurements need to include activity levels high enough to cause significant dead time in the scanner. Therefore, based on the peak values one can determine the limits of the scanner in terms of optimal activity for the scans. The measurements have to be performed using cylindrical scattering phantoms with a line source insert. From the same measurement an important factor could be also determined: the scatter fraction. This represents the percent ratio of the scatter coincidences compared to the total coincidence counts. From the long count rate measurement the last portion of the acquired data, where the random ratio is tend to be negligible. Scatter fraction measures the scatter events both from the target subject and the scintillation crystals.

4.2.5 Recovery Coefficient and Spill Over Ratio

The Recovery Coefficient (RC) is such a measure that gives information on the suppression of peak activity concentration when the sources are comparable in size with the spatial resolution of the scanner. In larger size objects the activity concentration is usually accurately measured, however when the sources are close to the spatial resolution in size the scanner underestimates the activity concentration of the source. This is the PVE (partial volume effect) mentioned above. The degree of this suppression depends on the object size as well as the reconstructed image resolution of the scanner [1]. The effect of PVE is illustrated in Figure 14. This underestimation effect can be measured and corrections could be applied accordingly. However, even if the RC value is estimated, the very same smearing

effect from high activity concentrations around the region of interest will cause a so-called spill over. This cross contamination should be measured with the ratio of the mean voxel intensities calculated from VOIs of a uniform activity concentration area of the object and a neighboring area where no activity concentration is present. Examples of this “spillover” effect are the contribution to the signal in gray matter regions of the brain from activity in the white matter, or the contribution to the signal of myocardial activity concentrations from the large blood pool in the heart [1].

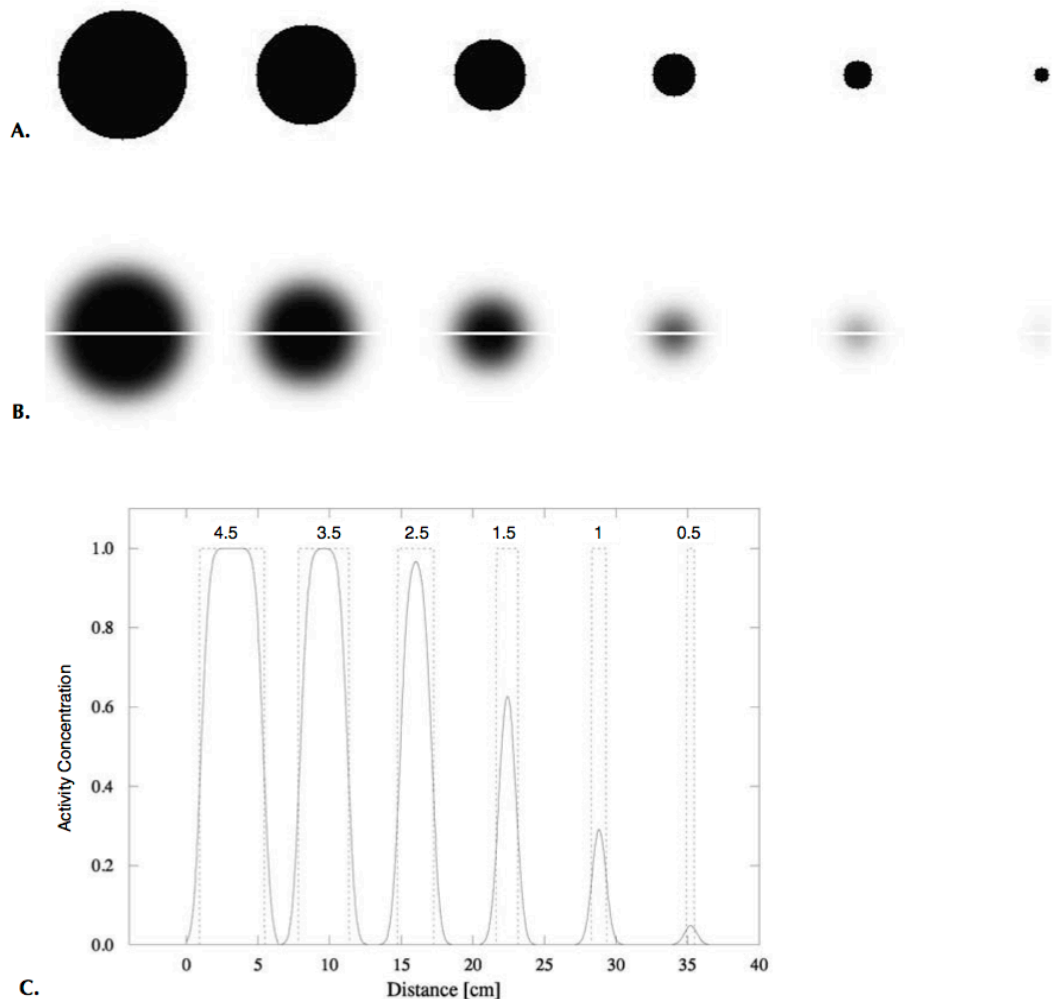


Figure 14. The data displayed here represents spherical activity sources (diameter ranging from 0.5 cm to 4.5 cm) of uniform activity concentration (A). Due to the partial volume effect (10-mm Gaussian smearing), the activity concentration in the smaller spheres appears to be lower (B) and a line-profile on these simulated images show this suppression even in a more emphasized manner (C)[1].

4.2.6 Image Contrast

Image contrast is an important measure because it has a high impact on the final depiction of pathology during the medical reading process. If a known activity concentration is filled in a phantom sphere and the surrounding activity concentration (background) is known as well, the ideal contrast can be defined as the following:

$$Ideal\ Contrast = \frac{Aconc_{sphere}}{Aconc_{background}} \quad Eq. 9.$$

where $Aconc_{sphere}$ and $Aconc_{background}$ are the activity concentrations filled in the phantom spheres and the background cavity. In ideal conditions the image contrast would result the very same value as the ratio of these two activity concentrations. In real PET measurements because of the PVE this will not be the case, and we would need again a recovery coefficient to be determined. Because the ideal contrast is different from the measured, real contrast of the images, it is reasonable to use the Contrast Recovery Coefficients (CRCs) that can be determined as:

$$CRC_{sphere} = \frac{\frac{C_{sphere}-C_{background}}{C_{background}}}{Ideal\ Contrast-1} = \frac{\frac{C_{sphere}}{C_{background}}-1}{Ideal\ Contrast-1} \quad Eq.10.$$

where C_{sphere} and $C_{background}$ the voxel mean from the applied VOIs on the sphere and background regions of the reconstructed images [43]. In Figure 15 three different imaging situations are displayed: a cylinder filled with uniform activity concentration (a), varied diameter rods filled with the same activity concentration in no background activity (b) and the same rods but in a hot background of a different activity concentration (c). The PVE effect is visible on panel b for the smallest rod diameter that is close to the resolution of the PET scanner in which the imaging measurements were performed.

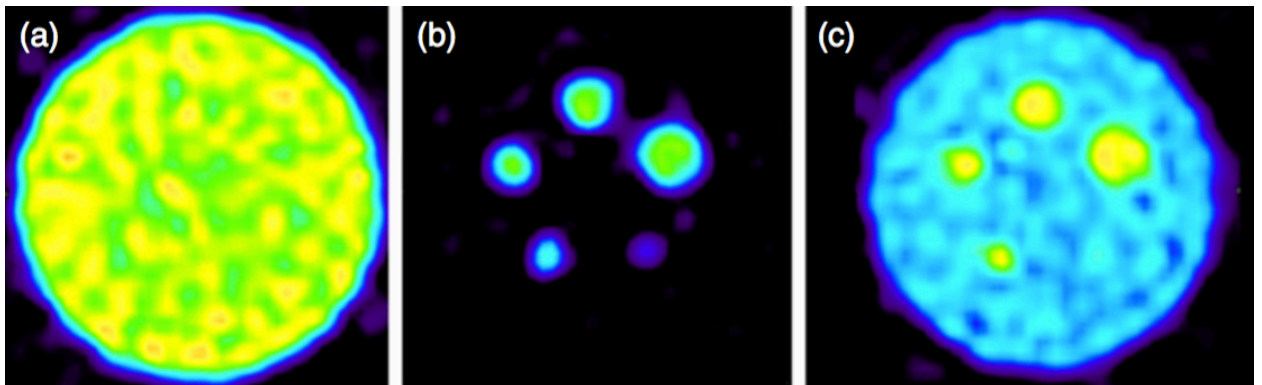


Figure 15. Uniform and RC regions of the NEMA NU-4 image quality phantom (a and b). The third panel (c) displays an artificially combined images of the former two [43].

4.3 Quantitative PET

PET became widely used in case of oncological studies mainly because of the high sensitivity, diagnostic efficiency and the ability that the images can be used quantitatively. It is important to emphasize, that among all tomographic modalities only PET and CT can be

used in all cases as quantitative method, while MRI is just in some cases. As the importance of comparing the image data before and after therapy was rising, physicians were looking for useful quantitative and semi-quantitative measures that would describe tumor characteristics and help staging. Usually for such a comparison of scans a semi-quantitative measure called standardized uptake value (SUV) is used. If all distortions have been corrected during the reconstruction process and the scanner is correctly calibrated with a measurement of a uniform cylinder filled with known activity concentration, the voxel units can be converted from counts per second (CPS) per voxel to activity concentration (kBq/ml). For the calculation of SUV units, the activity concentration intensities in the voxels are corrected with the weight of the patient and the activity dose that was administered into the patient. Therefore we receive a numeric measure that gives comparable information on two PET scans of the same patient without the bias effects of different amount of injected dose or weight changes between the scans. One can conclude that SUV results an average value of 1 in case of a uniform uptake in the total volume and in non-uniform cases it can vary depending on the uptake of the specific tissue. By definition SUV can be calculated as:

$$SUV = A_T \times \frac{V_T}{W_T} \times \frac{1}{D_{inj}} \times W_{subj} \quad \text{Eq. 11.}$$

where A_T is the radioactivity in the tissue region derived from the ROI on the images, V_T and W_T are the volume and weight of the target tissue respectively (and their ratio is the density of the tissue that can be assumed as 1), D_{inj} is the injected dose, W_{subj} is the weight of the subject (e.g. patient). In the earlier years of quantitation, SUVmax values were only in use, calculated as the maximum value of a certain ROI delineated by the physician. Because of the limitations of SUVmax and its sensitivity depending on the reconstruction pixel size made it difficult to compare images acquired on different scanners. The mean value of the same ROI (called as SUVmean) is also an attractive measure, however it is still limited on the delineation method and size of the ROI used. To overcome this problem standard size sphere shaped VOIs were proposed called as SUVpeak, which could give more correct information on the target tissue response. However, even this method has some limitations with larger or smaller variations in case of different tumor types and stages [45].

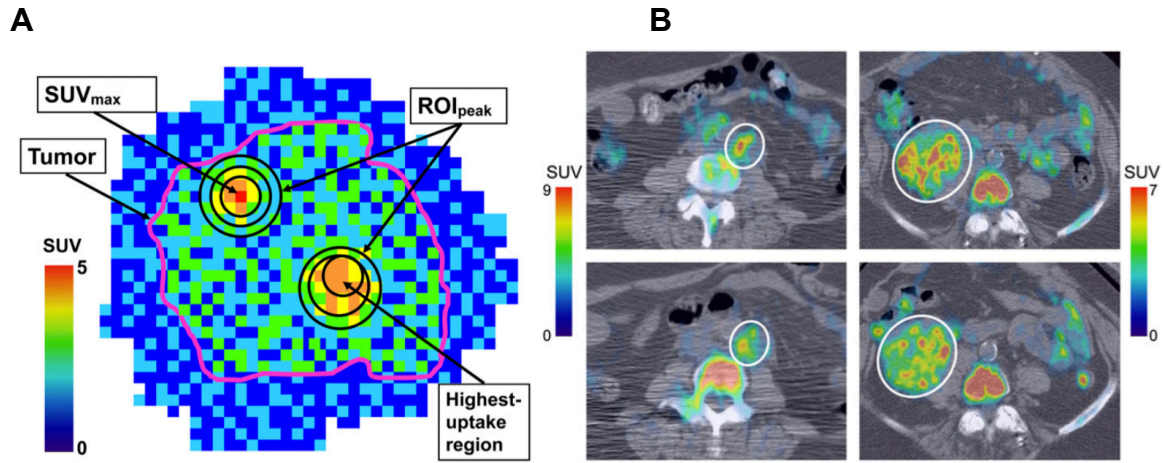


Figure 16. The multiple forms of SUV_{peak} are displayed on this figure along with the SUV_{max} within a delineated tumor (purple line, Panel A). Different tumor SUV_{peak} response variation on ^{18}F -FLT PET/CT images of a periaortic lesion (Panel B left) and a pelvic tumor (Panel B right). The top row shows the baseline and the bottom row the phase during treatment [45].

To assess appropriate SUV evaluations high image quality is needed with reasonably low noise and acceptable image contrast. Therefore, techniques that could improve image quality and hence give more accurate information are greatly welcomed.

4.4 Signal to Noise Ratio (SNR) of PET/CT and PET/MRI

Among other performance parameters mentioned above, image noise, especially in terms of Signal to Noise Ratio (SNR) plays a very important role in describing the quality of medical images. For measuring and describing noise, several methods could be used based on the focus of the study and the depth of information needed. The noise of medical images is called in several contexts as image uniformity, or background variability and even SNR or Contrast to noise Ratio (CNR). As mentioned above the NEC rate gives a numeric information about the noise propagated into the raw data, therefore it is giving a global measure on SNR, but it is not sensitive to the regional activity distribution of the images [1]. However, even NEC can give information that could be used as a first step to optimize imaging protocols [46]. The NEC as a global noise parameter is able to predict local noise of the actual images, however it is somewhat limited to conventional FBP and non-TOF reconstructions [47]. When evaluating reconstructed images, in some cases it is enough to calculate the ratio of the Mean and Standard Deviation (SD) values for the pixels of a predefined ROI on a fairly homogenous background region (e.g. liver). This measure is many times named as image uniformity. When the comparison of different activity uptake regions is important, the ROI mean of the target tissue (e.g. lesion) subtracted by the mean of a background ROI (e.g. liver ROI) and all of these divided by the SD of the background ROI could be used [48]. This measure is many times also called as SNR [49], however sometimes referred to be CNR as well.

$$CNR = \frac{Mean_{target} - Mean_{background}}{St.Dev_{background}} \quad \text{Eq. 12.}$$

Calculating CNR in this manner many times gives appropriate information on the recognition of the target tissue (e.g. lesion). This definition of CNR (at that time called as SNR) was first given by Rose, who was interested in the in the quality of television images. He showed that a small object is distinguishable from its background if the CNR value is larger or equal than 5. This is known as the Rose criterion in the imaging field. However, depending on the imaging task and the size, in many cases the target tissues are still detectable on medical image sets with lower CNR values [49]. The representation of CNR determination along with the distribution functions is displayed in Figure 17.

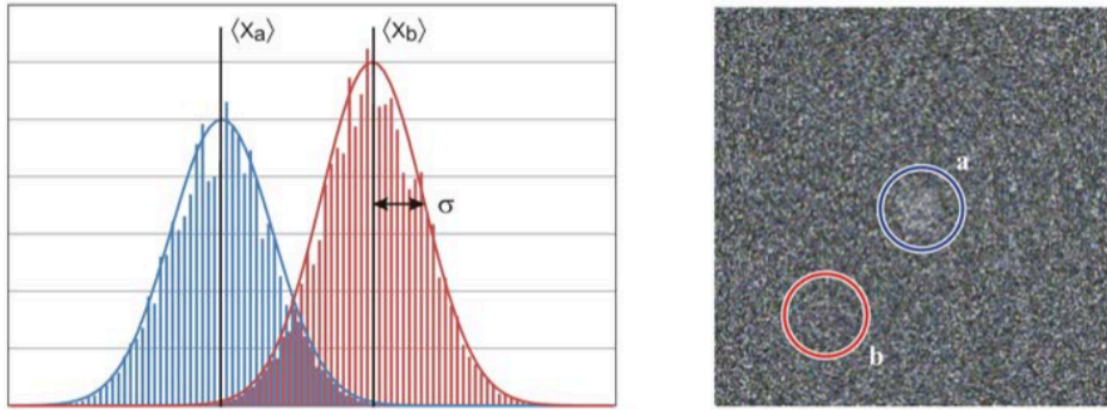


Figure 17. Target tissue ROI (a) and the background tissue ROI (b) of an investigated image (right) and their intensity distributions (left). X_a and X_b are the mean values of the target and the background ROI pixel intensities respectively, s is the St.Dev of the background ROI [49].

Moreover, calculating the SNR as the Mean/SD values for each pixel or voxel using a series of image sets is usually the most straightforward way to receive accurate information on the noise characteristics of the given image set:

$$SNR = \frac{Mean_{voxel}}{St.Dev_{voxel}} \quad \text{Eq. 13.}$$

Although, this calculation is many times limited to phantom scans and cannot be performed in the daily routine of the clinical level. However, in some cases using a single raw data set with the so-called bootstrap method these image series and their noise properties could be determined [50]. Another SNR measure, the noise power spectrum (NPS) is a very sophisticated method, which gives spatial frequency information about each pixel of the given image slice using Fourier-transform. NPS has been shown to measure image noise texture for different medical imaging modalities including PET [51]–[53] while giving detailed information on image SNR.

As mentioned before SNR is affected by several factors including scanner sensitivity, spatial resolution, NEC rate etc. A system with high spatial resolution should

typically produce images of higher SNR compared to a system of lower spatial resolution, assuming an equal number of acquired counts. Therefore, the better spatial resolution may result in images with worse uniformity (SNR) [33], [34]. On the other hand higher NEC means more counts and causes better noise properties. Therefore, these two effects counteract each other and contribute to a final balance in the image SNR.

The SNR is depending on the detector technology, including the detection efficiency and the readout logic of the scintillator crystals. Among the new hybrid medical imaging technologies, the introduction of PET/MRI had great attention in the medical imaging field worldwide. The inclusion of both imaging modalities in a single device demanded solutions of complex engineering challenges, especially in terms of PET detectors to operate in high magnetic fields. Conventional PMT detectors benefit from high signal gain in the range of $10^5 - 10^7$ [1], [54]. Low noise and fast transit time (~ 100 ps) are also available today, and has made this photo-sensor the first candidate for application involving the TOF PET technology. However, in strong magnetic fields PMT technology is not able to produce acceptable position maps for imaging purposes. New photo-detector concepts using semi-conductors called Avalanche Photodiodes (APDs) provided a solution for this problem and has ben already used efficiently as a photo-sensor for PET near strong magnets [9], [12], [56], [55]. However the SNR performance of these applications is lower compared to former PET technology because APDs have significantly higher rise times (up to 2-3 ns) [54] that prevent adequate timing resolution for TOF. The SNR gain from the TOF capability can be described as:

$$SNR_{TOF} = \sqrt{\frac{2D}{c\Delta t}} \times SNR_{non-TOF} \quad \text{Eq. 14.}$$

where D is the diameter of the imaged object, c is the speed of light, and Δt is the timing resolution of the system [26]. Furthermore the low gain ($\sim 10^2$) remained a disadvantage of APDs as well [9], [54]. Coupling LSO crystals with newly introduced SiPM technology resulted in timing resolution sufficient for TOF measurements [57]. The considerably lower noise of SiPMs (compared to the APDs) and high gain ($\sim 10^6$) are the additional promising features of SiPM, which made this technology suitable for PET photo-detectors for advanced PET/MRI systems. It is need to be noted that PMTs have lower noise characteristics compared to APDs or SiPMs [54]. Some approaches for the inclusion of SiPM in a full-ring PET detector system have already been introduced successfully [58]–[60]. These developments were mainly focusing on preclinical PET imaging devices, however the human applications are already in the production phase and will be available in the near future.

Another great advantage of SiPMs is the possible one-to-one coupling with scintillation crystals that could eliminate the position map coding error of the conventional analog PMT method, and therefore contribute to better spatial resolution (Figure 18.). This has an impact even on the time resolution of the scanner and therefore gives an improvement compared to former TOF gained SNR with a factor of two [http3]. These advancements apply for both PET/CT and PET/MRI techniques and therefore are very promising in case of recently introduced and future hybrid systems. One can observe the improved SNR characteristics of a whole body PET scan in Figure 19.

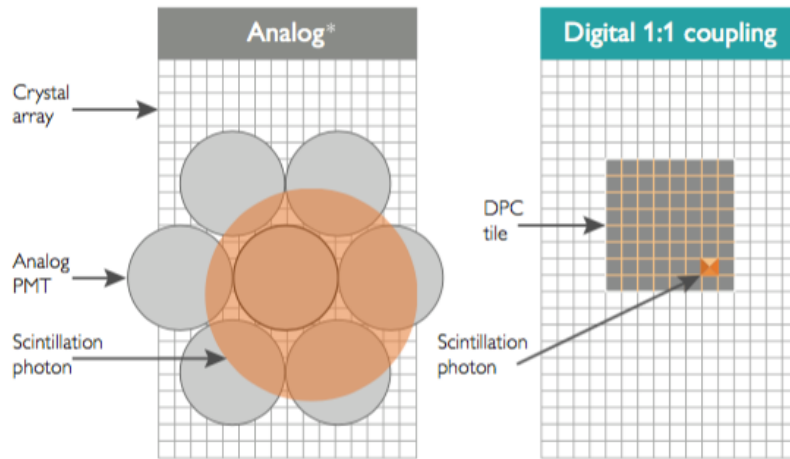


Figure 18. Conventional analog PMT readout of the scintillation crystals with the well known Anger logic concept (left) and the new digital one-to-one readout concept offered by SiPM photosensors also called as Digital Photon Counting (DPC, right) [61].

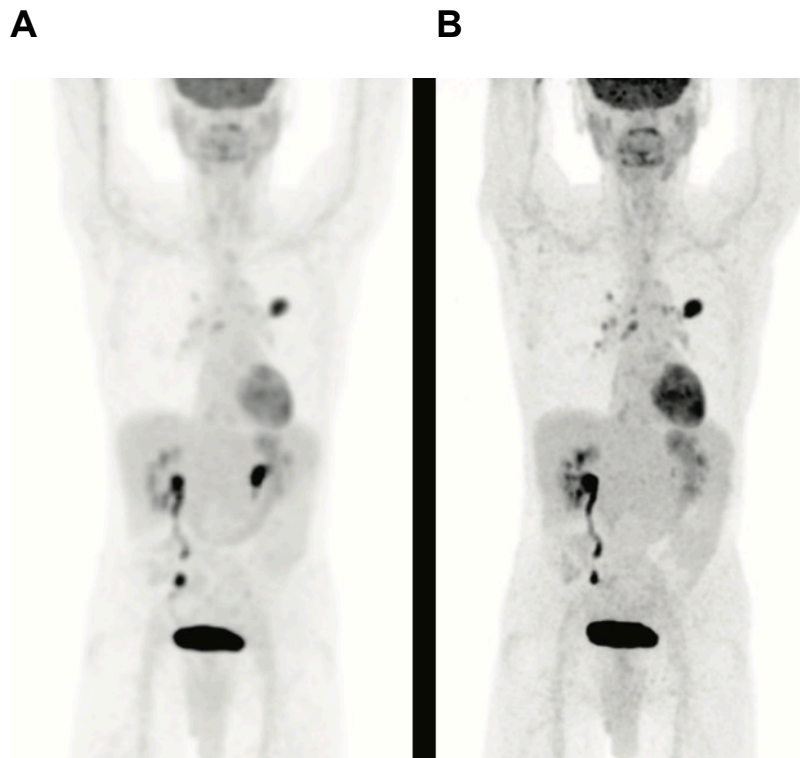


Figure 19. Whole Body PET images acquired with the conventional Anger logic readout based scanner (A). The new SiPM based one-to-one coupling provides improved SNR characteristics throughout the whole 3D image volume [61].

Besides using appropriate detector technology in hybrid imaging, it is important to optimize the scanning protocols and the reconstruction methods for both patient

characteristics and scanner properties [62]. In the clinical PET/CT protocols the acquisition time necessary to collect enough counts to produce images of high diagnostic quality depends on several factors, including scanner sensitivity, imaging mode (2-D or 3-D) and patient weight [63]. Both, the number of total counts acquired during the acquisition and the quality of PET images are negatively correlated with the weight of the patient [64]. Extended acquisition times are typically required for heavier patients (rather than increasing administered dose) in order to maintain image quality [65]. However, the lengthening of acquisition time per bed position over a certain limit would not necessarily improve lesion detection [63]. Image data for PET studies are typically collected in discrete axial bed positions in most cases. The acquisition scan duration is usually adjusted according to the weight or the Body Mass Index (BMI) of the patient (1-5 min/bed position for non-TOF and 1-3 min/bed position for TOF scanners). Although the total acquisition time is adjusted to the patient body properties, the acquisition time at each bed position is kept constant. This means that a body section where there is less attenuation (head and neck) will have the same acquisition time as a section where there is more significant attenuation (abdomen). As the different sections of the body have various gamma radiation attenuation factors and activity distribution as well, it is expected that the image SNR will vary accordingly. During the clinical reading process of the images the constant SNR would be preferable, therefore methods to optimize acquisition durations of bed positions would be necessary for the harmonization of SNR axially. This concept of varying the acquisition time durations of different bed positions may be seen as analogous to the Tube Current Modulation (also known as Automatic Exposure Control) used in X-ray CT for dose reduction [66]–[68]; however, in PET the time modulation could be used to equalize image SNR axially.

5. Aims

While many research groups reported on good results of SiPM PET applications, our institutions also started to work on the direct comparison of SiPM with conventional PMT technology on PET scanner performance and imaging capabilities. We developed two preclinical imaging systems: the MiniPET-2 with PMT technology and the MiniPET-3 using SiPM detectors. The geometrical parameters, the scintillation crystal material, data acquisition system, image reconstruction methods of the two systems were kept the same. We aimed to:

1. Compare the imaging capabilities of two small animal imaging systems with the same crystal geometry but different photo-sensors.
2. Perform the direct comparison by measurements as specified by the NEMA NU 4-2008 measurement protocols, extended with energy resolution and coincidence time window optimization measurements.
3. Report on the first complete performance and imaging capability evaluation of a SiPM based PET scanner using this NEMA standard
4. Evaluate the imaging and performance data with the same software environment
5. Perform computer simulations, aiming to describe the characteristics of a human scale scanner based on the MiniPET concepts.

We started to work on the optimization of patient scanning protocols of Whole Body PET scans to harmonize image noise axially. While many approaches are available to determine SNR for human whole body PET imaging, we used pixel-wise the Standard Deviation/Mean (St.Dev/Mean) values on series of image sets, hence this measure gives the appropriate depth of information for this study. We aimed to:

1. Investigate the possibility of varying the acquisition time for different sections of the body such that the image SNR is kept relatively constant for all slices.
2. To estimate the acquisition times for the different sections of the body we propose to use the sinogram of attenuation correction factors (ACFs) generated from the CT scan that is typically acquired prior to the PET scan.
3. Perform both computer simulations (based on real CT patient data) and evaluations of phantom and patient PET data for the proof of this new concept.

6. Materials and Methods

6.1 Performance Comparison of the MiniPET-2 and MiniPET-3 preclinical PET systems

6.1.1 Scanner Description

The technical and geometrical parameters for both MiniPET scanners compared to some currently available commercial preclinical PET scanners are listed in Table 3. The two MiniPET systems include the same-sized gantry, detector crystal material, crystal size, crystal pitch and detector module configuration. The significant difference between the systems lies in the photo-sensors: the MiniPET-2 system includes conventional PMTs, while the MiniPET-3 system includes SiPMs (Figure 21) and a readout system optimized for this type of detectors (Figure 23). A row-column readout of the SiPM matrix was used without applying individual signal processing channels to each matrix element. Weighting circuits were connected directly to the row and column outputs as proposed by Y. Wang et al. [72], but modified in such a way as to reduce the dark noise. The overlap between the crystals and the SiPM sensitive areas were determined during the design of the SiPM sensors for the purpose of optimal position encoding. The LYSO crystal matrix and the SiPM sensor board were attached together with a light-guide designed to receive light from every scintillation crystal.

Table 3. Basic physical and technical parameters of the MiniPET-3 and MiniPET-2 detector systems compared with available preclinical PET systems from different vendors.

Category	MiniPET-2 and MiniPET-3 scanners	Inveon [11], [69], [70]	NanoPET [71]	LabPET8 [12]
Detector module				
Scintillator Material	LYSO	LSO	LYSO	LYSO and LGSO
Crystal Size (mm ³)	1.27×1.27×12	1.5×1.5×10	1.12×1.12×13	2×2×11.9 and 2×2×13.3
Crystal array size	35×35	20×20	81×39	16×16
Photon sensor	SiPM for MiniPET-3 PMT for MiniPET-2	PMT	PMT	APD
System				
Number of detector modules	12	64	12	12
Number of detector rings	35	80	81	32
Inner diameter of detector ring (mm)	211	161	181	162
Solid angle / 4π	0.22	0.62	0.32	0.42
Axial FOV (mm)	48	127	94.8	75
Trans-axial FOV (mm)	100	100	123	100

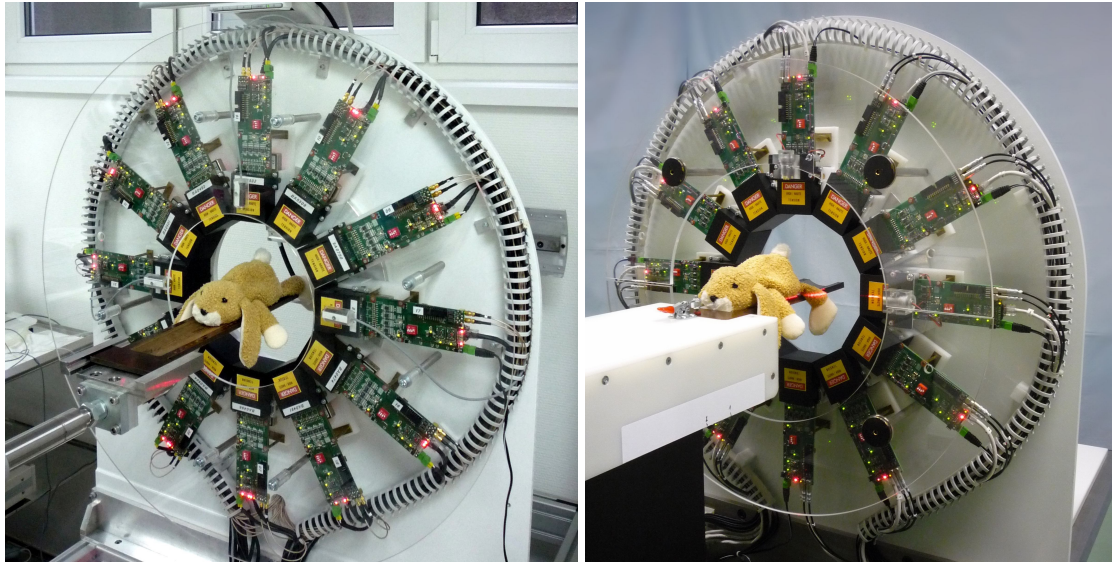


Figure 20. Representative photo images of the MiniPET-2 (left) and MiniPET-3 (right) preclinical PET systems.

SiPM sensors were arranged to overlap with crystal clusters of three rows and three columns. Light from these clusters was collected at a relatively high efficiency compared to crystal elements, which did not overlap with the SiPM as shown in Figure 22. Among all crystal elements, 59.5% were located at regions of relatively high light collection efficiency, while 40.5% were located in regions of relatively low light collection efficiency. A total of 324 SiPM sensors (18×18) were arranged in 2×2 blocks, and these quads were produced in a 9×9 configuration. The SiPM matrix active area is $48 \times 48 \text{ mm}^2$ and the size of each SiPM sensor is $1.95 \times 2.2 \text{ mm}^2$. The number of microcells in each sensor is 833. An epoxy light guide (Philips Research, Eindhoven) was used between the SiPM tile and the crystal matrix with a thickness of 1.3 mm.

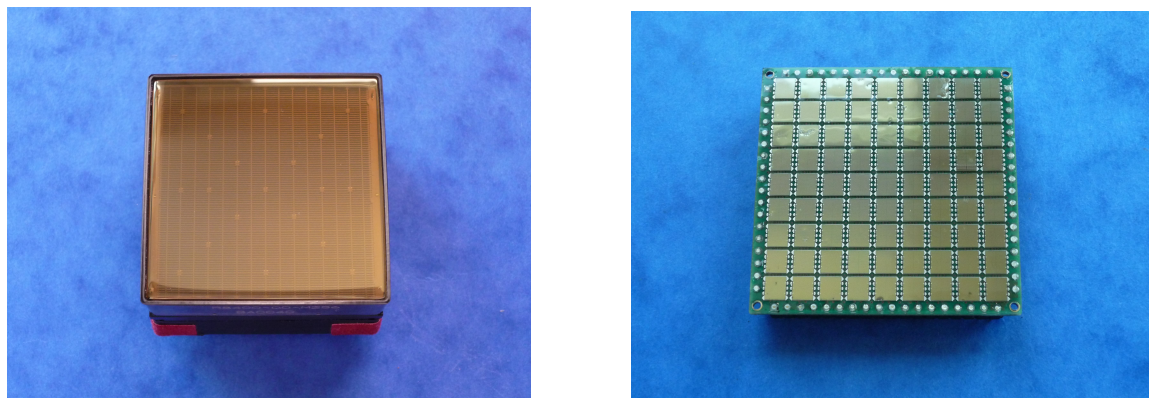


Figure 21. Photodetectors: PSPMT used in case of the MiniPET-2 (left) and SiPM tile for the MiniPET-3 (right).

In the case of MiniPET-2, the PMTs were attached to the LYSO scintillation crystal matrixes with a special optical coupling compound called Visilox V-788. In this case the thickness of the optical coupling remained under 0.5 mm. Digital signals were fed into a Xilinx Vertex4 Field Programmable Gate Array (FPGA) board, where time stamp

generation, energy calculation, signal recognition and status check processes took place [14]. Data from the detector modules were transmitted to the data acquisition computer via the 100BASE-TX Ethernet network system. The custom made MultiModal Medical Imaging (M3I) software library was developed [http4] for the tasks of data collection and processing such as primary data processing, scanner calibration, image reconstruction, image processing and evaluation of performance parameters. This software tool arranges the data into 3D Line Of Response (LOR) or single events list-mode data files that can be histogrammed into 2D sinograms. The M3I performs 2D Maximum Likelihood Expectation Maximization (ML-EM) [27] that we used in case of the image quality measurements.

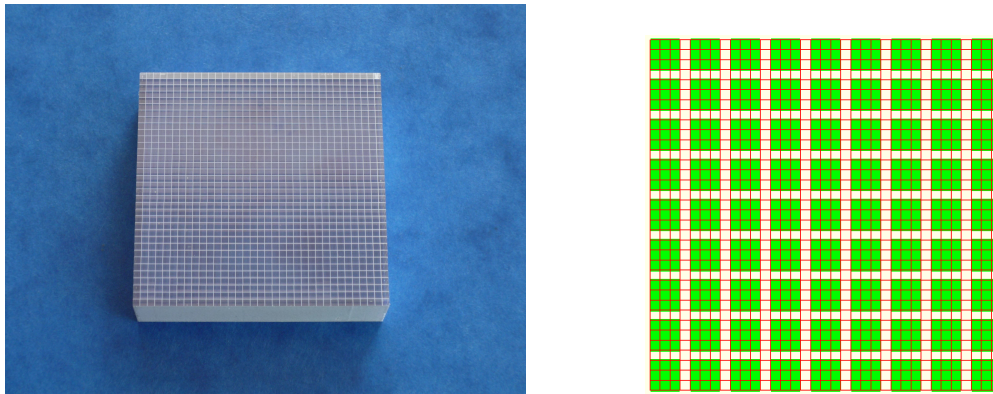


Figure 22. LYSO scintillation crystals (left): 35×35 element array, pixels: 1.27 mm, gap: 0.076 mm, pitch: 1.347 mm, finish: all crystal surfaces polished, internal reflector, external reflector, overall dimensions: $47.17 \text{ mm}^2 \times 12 \text{ mm}$ thick. Schematic image (right) of the LYSO Scintillation Crystal (red) and SiPM sensor (green) overlap positions in the MiniPET-3 detector module.

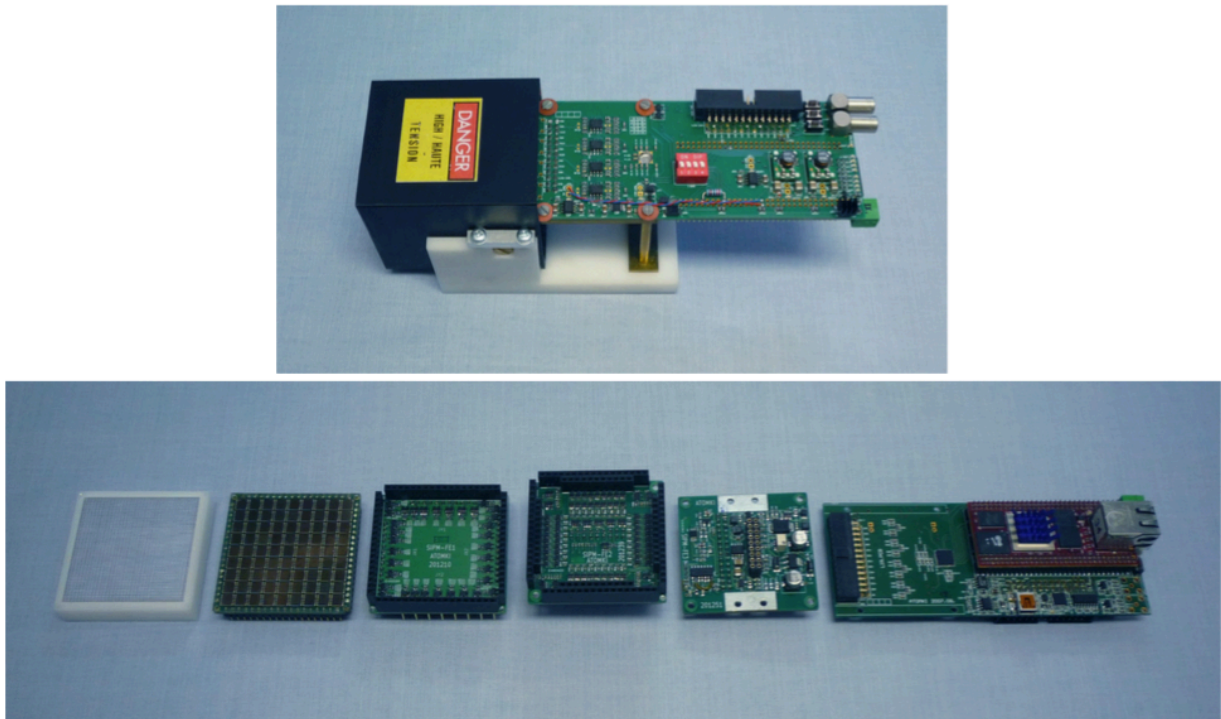


Figure 23. MiniPET-3 detector module assembled (top) and disassembled (bottom). On the disassembled image we can see from the left to the right: LYSO scintillation crystal matrix, SiPM photo-detector module, front end electronics No. 1, 2, 3 and the LIR (Local area network based Interface for Readout) card.

For the evaluation of spatial resolution of the systems, Filtered Backprojection (FBP) was used. All other images in this evaluation were reconstructed using ML-EM, as implemented in M3I, using 20 iterations without any post-reconstruction filtering. The same system matrix was used for both systems during this study.

6.1.2 Position encoding and energy resolution evaluation

Measurements performed for position encoding and energy resolution were conducted with an ^{18}F point source of 4 MBq activity, while positioned in the center of the Field of View (FOV) axially and transaxially. A 1200 sec list mode dataset was acquired in each case. From the list-mode data, events were sorted into energy histograms for every crystal element, and the FWHM values of the 511 keV peaks were calculated. The ^{18}F energy resolution was calculated as the FWHM value divided by the peak channel number times 100. Measurements performed on the MiniPET-3 took into account the non-linearity between SiPM signals and photon energies. The lower energy threshold was set to 360 keV using ^{131}I measurements, while the upper energy threshold to 662 keV with ^{137}Cs . These isotopes have definite signal peaks at the mentioned energies. For position encoding purposes this same measurement protocol was used, and the position maps for each detector modules were determined.

6.1.3 Coincidence Time Window Optimization

The FWHM of the timing resolution were 3.29 ns for the MiniPET-2 and 3.76 ns for the MiniPET-3. In the MiniPET systems each detector module is in coincidence with 3 other modules on the opposite side of the gantry. Therefore, the total number coincidence connections are 18. Time alignment for all 18 detector-connections were performed with appropriately shifting the coincidence time histograms in case of both MiniPET systems. Without any optimization the measured time spectra can be seen in the representative plots of Figure 24. We defined the spectral average for the coincidence time histogram between the i^{th} and j^{th} module as T_{ij} . In addition we introduced new offset parameters for each detector and the following equation to set any new arbitrary T_{ij}' histogram mean values:

$$T_{ij}' = T_{ij} + t_i + t_j \quad (i, j = 1 - 12) \quad \text{Eq.15.}$$

with the special condition that all T_{ij}' has to be equal. In this way there are 18 equations for the 12 unknown t_i , which is a typical over-determined system of linear equations that can be solved. Presuming that all T_{ij}' should be zero, we solve the above equation and use the

resulted t_i parameters as timing offsets for the detectors.

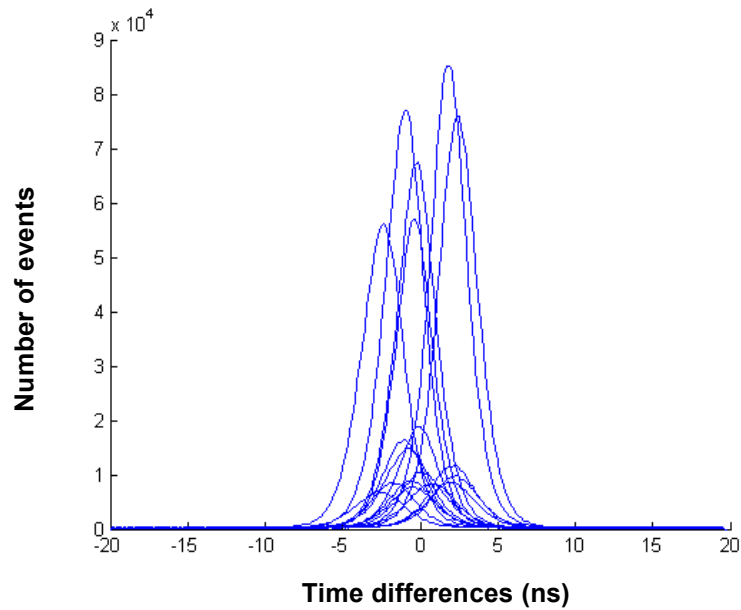


Figure 24. Coincidence spectra of the 18 detector connections without proper time alignment.

An optimal coincidence time window (τ -value) must balance the need to maximize the true coincidence count rate while minimizing the randoms count rate. This optimization is dependent on the source activity as well as the FWHM of the coincidence time histogram. In order to determine the optimal τ -value on the MiniPET-3, a cylinder phantom (inner diameter: 45 mm, length: 200 mm) filled with ^{68}Ga was used. Raw data was acquired at an initial activity level of 17.05 MBq for two-minutes using a τ -value of 2 ns. Nineteen subsequent measurements were repeated with increasing the τ -value in 2 ns increments, resulting in a total of 20 measurements. The actual true and random coincidence rates were obtained during the measurement. In addition, we calculated a parameter that is similar to Noise Equivalent Count (NEC) rate defined as: $\text{True}^2/(\text{True}+2*\text{Random})$, which was used to find the optimal τ -value. For the MiniPET-2 the optimal τ -value was determined in a previous study [14].

6.1.4 Spatial Resolution Measurement

For the purpose of measuring spatial resolution, usually ^{22}Na that has half-life long enough to be used for a few years. The measurements are performed with this point source placed in different predefined locations along the axial and radial directions. The spatial resolution for both the MiniPET systems was measured using a $1 \times 1 \times 1 \text{ cm}^3$ cast acrylic cube (Eckert & Ziegler Isotope Products Inc.). The center of the cube included a 0.25 mm^3 spherical ^{22}Na point source. Individual measurements using this point source were performed at separate locations: 0 mm, 5 mm, 10 mm, 15 mm, 25 mm and 35 mm radial offset from the central axis of the scanner. These measurements were repeated using the

same radial locations, but shifted to $\frac{1}{4}$ from the axial center. The 3D data were then rebinned into 2D LORs using the Single-Slice Rebinning (SSRB) algorithm. As proposed by the NEMA standard, we used 2D FBP for the image reconstructions of the spatial resolution acquisitions. For each of the 12 measurements, a profile through the point was obtained. The FWHM of this profile was then used to determine the spatial resolution for each image.

6.1.5 Sensitivity Measurement

Sensitivity is technically measured as the ratio of the true coincidence rate and the used source activity. Determination of the sensitivity requires an activity source in which the rate of the annihilations is precisely known [14]. For the sensitivity measurement a line source or a point source needs to be used in case of the human and the preclinical scanners respectively. The measurements have to be performed in the radial center of the FOV, and covering the entire axis of the scanner until the edges of the detector ring is reached. The sensitivity measurement was performed on both MiniPET systems using a ^{22}Na point source initially placed in the center of the FOV. Subsequent images were taken by shifting the point source axially towards the edge of the detector ring in 1.35 mm increments, resulting in a total of 35 scans. The absolute sensitivity for each i th ($i=1, 2, \dots, 35$) acquisition was calculated as:

$$S_{A,i} = \frac{1}{0.905} \left(\frac{R_i - R_{B,i}}{A_{\text{cal}}} \right) \times 100\% \quad \text{Eq. 16}$$

where A_{cal} is the activity of the point-source, 0.905 is the branching ratio of ^{22}Na , R_i and $R_{B,i}$ are the source and background total count rate for the i th acquisition, respectively. System peak absolute sensitivity is defined as the $S_{A,i}$ at the center of FOV [72]. Total Absolute Sensitivity ($S_{A,\text{tot}}$) was calculated using the following equation:

$$S_{A,\text{tot}} = \frac{\sum_{i=1}^n S_{A,i}}{n} \quad \text{Eq. 17}$$

where, $S_{A,i}$ is the absolute sensitivity at slice i , n is the maximal slice index (35 in our case) [14]. This formula follows the concept of some recent articles [10], [14], [69] and the extension of the NEMA NU-4 in 2011.

6.1.6 Image Quality Phantom Study

For the image quality measurements, the NEMA NU4 IQ phantom was used, which has a cylindrical shape with fillable rods of different diameters drilled in cold, solid

background for computing RC values. In addition to RC, the NEMA standard also includes protocols for the determination of image uniformity and SORs using a homogenous region and two cylindrical chambers (cold chambers) within the IQ phantom. The uniformity is calculated as $\%Stand.Dev.$ that equals to $Ustd/Umean*100\%$, where $Umean$ and $Ustd$ are the mean and standard deviation values for the homogenous region. Image acquisition, histogramming, and reconstruction were very similar when performed on the MiniPET-2 and MiniPET-3. These images were acquired from the NU 4 IQ phantom filled with ^{18}F at an initial activity of 3.7 MBq activity. One of the cold chambers was filled with water, the other with air. The phantom was positioned on the animal bed port of the scanner along its central axis. Data was acquired using 1200 sec list-mode dataset of the phantom was acquired in both cases. The list-mode raw data were binned into 3D coincidence LORs, representing in the geometry of the scanner. These 3D data were then re-binned into 2D LORs using the SSRB algorithm. Images were reconstructed from the 2D rebinned data using the ML-EM method with 20 iterations. From the reconstructed images RC, SOR and uniformity values were determined using our cross validated software.

6.1.7 Scatter Fraction and Count Rate Performances

The count rate protocol allows the determination of the true and random ratio, as well as the NEC rate. The scatter fraction was determined from the data measured at low activity levels when the random ratio is negligible. The measurements were performed using two cylindrical scattering phantoms (the so called rat and mouse phantoms) with a line source insert of high activity concentration, as recommended by the NEMA NU 4 standard.

6.1.8 Small Animal Studies

Scanning of rats on both MiniPET systems were performed with injected activity of 5.6 MBq and the acquisition scan durations of 20 minutes. Images of the brain and the heart regions were performed and evaluated.

6.2 Human brain PET scanner simulation based on MiniPET concept

The objective evaluation of the imaging capabilities of a PET system frequently needs a realistic simulation tool to model or track the data acquisition process. Monte-Carlo based simulation is an indispensable tool in modern detector engineering, depending on the available computing capacity it can be applied more-or-less efficiently. Basically, there are two different simulation strategy for this purpose: the Monte Carlo (MCS) one and the analytical simulation (AS). The AS simulations run faster but they give less realistic and precise data for the PET systems, thus we could not apply these types of simulation tools.

The MCS program follows each individual gamma-ray from the annihilation to single or multiple interaction (scatter), and final absorption or escape, both in the source and the individual scintillation detectors. The MCS can follow each individual photon inside each crystal up to the photocatode or APD sensor, with provisions for light losses due to escape, surface imperfections, and absorption. Furthermore, it can take into consideration photomultiplier characteristics in order to form the final signal. The MCS can be used to obtain information about the different processes occurring within the phantom and detectors (energy pulse-height distribution, point spread function and the scatter and scatter to total fractions in 2D and 3D modes can be obtained). Several studies have been published that address MCS of the coincidence detection processes. In the most cases the base of these MCS programs is the GEANT MCS that was originally developed in high energy physics research. There are two freely available MCS software tools and libraries in the field of emission tomography: the GATE [[http5](#)] simulator, and the SimSET package [[http6](#)].

The SimSET package uses Monte Carlo techniques to model the physical processes and instrumentation used in emission imaging. The software is written in a modular format, and the core module is the Photon History Generator or PHG, which models photon creation and transport through heterogeneous attenuators for both SPECT and PET. The Collimator Module receives photons from PHG and tracks photons through the collimator being modelled. The Detector Module receives photons either directly from the PHG module or from the Collimator module. It tracks photons through a specified detector, recording the interactions within the detector for each photon. Each module can create a Photon History File to record information on the photons it has tracked. The Binning Module is used to process photon and detection records, and can be used on-the-fly or on pre-existing history files. The PHG, Detector and Collimator modules are configured using Parameter Files and Data Tables, examples of which can be found in each of the relevant module chapters. Digital phantoms for PHG (Activity and Attenuation Objects) can be created using a utility called Object Editor. The SimSET package also comes with a range of utilities for manipulating datasets and history files. The implemented physical models are as follows: planar SPECT, dual headed PET and cylindrical PET systems.

The GATE has several additional features comparing to the SimSET, such as optical photon simulation, very complex detector geometry and gantry definition, graphical output to check the system view, complex logging and event tracking, sophisticated activity distribution and phantom definition and so on. Thus the used Monte-Carlo simulation system was based on the GATE, which is built upon the Geant4 software from CERN. The goal of this task is to set up a simulator chain and presume the imaging capability of the human PET system. This simulation rely upon a set of models coming from the preliminary

results of sub-modules and the MiniPET-3 PET system (developed by Institute for Nuclear Research, Hungarian Academy of Sciences). We specified the most important parameters of a brain human PET detector system by simulations with the use of GATE software package. The main features of the whole human PET system, like detector block quality, sensitivity profiles and count rate performance can be tested by the GATE simulation tool.

6.2.1 *The GATE simulation environment*

The GATE software environment has been set up on the High Performance Computing (HPC) cluster in our university [http7]. HPC consists of several hundred nodes with a total of 2352 for HPC in Szeged and 1536 for HPC in Debrecen.

6.2.2 *Definition of the scanner geometry*

The detectors of the human camera were simulated using similar component of MiniPET-3 (pattern and physical properties of SiPM and crystal material). During the simulation the block and crystal size was changed from the MiniPET-3 geometry to

- Crystal size: $2.1 \times 2.1 \times 20 \text{ mm}^3$,
- Crystal pitch: 2.17 mm
- 21×21 pixelated crystal matrix
- Light guide: epoxy layer (refractive index 1.5) with thickness of 1.3 mm
- Reflector material of Teflon

The $2.1 \times 2.1 \times 20 \text{ mm}^3$ crystal size matches to the Siemens HRRT brain scanner pixel size. We decided to use this geometry, because the preliminary running tests with the GATE showed that the optical photon simulation dramatically degrades the calculation speed, even on the HPC cluster. If we reduced the whole body PET geometry to the brain scanner size, the number of coincidence connections were also significantly decreased. Furthermore, we simulated two scanner geometries with different axial field of view: 45.57 mm (smallFOV simulation) and 182.28 mm (largeFOV simulation). In both case the scanner radius was 175 mm, which is the appropriate size of the HRRT brain scanner. All simulations were performed for the readout characteristics of the SiPM and LSO based PET detector module, using optical photon simulations in the GATE simulation software environment.

6.2.3 *Simulation of position maps and energy resolution*

Simulations of position maps using a point source was performed for the 21×21 scintillator detector matrix. Along with the position maps the energy spectrum of the scanner was also monitored and the energy resolution was calculated,

6.2.4 Simulation of the count rate capability and system sensitivity

For NEC parameter ($NEC = T^2/(T+S+a*R)$) and the relating NEC curve, we calculated separately the single, the true + scatter and the random rate values as follows:

$$Singles = (bkg + \eta_{si} * \alpha) * e^{-c1 * \tau * (bkg + \eta_{si} * \alpha)} \quad \text{Eq. 18.}$$

$$T + S = \eta_{true} * \alpha * \left[e^{-c2 * \tau * (bkg + \eta_{si} * \alpha)} \right]^2 \quad \text{Eq. 19.}$$

$$R = (bkg + \eta_{si} * \alpha)^2 * \Delta\tau * nlor * \left[e^{-c3 * \tau * (bkg + \eta_{si} * \alpha)} \right]^2 \quad \text{Eq. 20.}$$

where “ η_{si} ” was the singles sensitivity and “ η_{true} ” the trues+scatter coincidence sensitivity. The η_{si} and η_{true} parameters are significantly influenced by the source and the scanner geometry. Hence, the η_{si} and η_{true} were determined using GATE for the given PET geometries. The NEC parameters are depended on the measured activity distribution. Thus, we used the standard NEMA rat like phantom at both simulations. The phantom was placed in the center of the field of view of the simulated cameras. Besides the count rate performance, the system axial absolute sensitivity profile was calculated as it is required the NEMA-NU-4.

6.3 Whole body PET image SNR optimization using variable acquisition times

6.3.1 PET/CT System

The system used in the work was a Siemens Biograph 64 Truepoint PET/CT system. The PET portion has an axial field-of-view of 22 cm and an approximately isotropic intrinsic resolution of about 4.5 mm FWHM. The CT portion of the system is a 64-slice CT.

6.3.2 SNR Simulations

To estimate the effect of attenuation on image SNR a series of simulations was performed based on whole body CT scans (patient weights ranged from 54-108 kg). From the CT scans, attenuation correction factors were generated using the bi-linear scaling method [73]. Using the same CT images, a uniform activity distribution in soft tissue was generated. Using the soft tissue activity and the attenuation correction factors, emission sinograms were generated by forward projection. To estimate the noise distribution in the images, Poisson noise was added to the sinograms and 20 noise replicates were generated. Each replicate was corrected for attenuation and reconstructed using iterative image

reconstruction (Ordered Subsets Expectation Maximization with 4 iterations and 8 subsets (OSEM 4i8s)) [27]. From the 20 replicates, pixel-wise mean and standard deviation images were generated. For each axial body slice one standard deviation and mean value was calculated as the average pixel intensities within a 4 cm diameter circular ROI. In the following, we will refer to the pixel-wise calculated mean and standard deviation as Mean and SD respectively. The correlation between the SD/Mean values and the average attenuation correction factors (averaged over all angles) passing through the center of the body was also investigated. In addition to the patient simulations, circular, elliptical and patient outline simulations were performed. Cylinder diameters between 6 and 40 cm with uniform activity were simulated. Attenuation properties were simulated assuming uniform attenuation distribution with water equivalent (linear attenuation coefficient). The forward projection of the μ -maps was used for attenuation of the emission data and for attenuation correction. Attenuated emission sinograms were created by forward projecting the activity images and using the attenuation sinograms. From these sinograms, twenty noise replicates were generated with Poisson noise added to each sinogram elements. From these replicates attenuation corrected images were reconstructed using iterative reconstruction (OSEM 4i8s). Mean and SD images were calculated from the 20 noise replicates pixel-by-pixel. As an SNR parameter we calculated the SD/Mean in a 4 cm diameter circular ROI that was used on both the Mean and SD images. For the ellipse simulation, ellipses with random semi-minor and semi-major axis between 10 and 20 cm were generated. Forty different ellipses were generated and processed in the same manner as the cylinder image simulation. For refining the method and to be more close to the shape of a patient, images were generated with using the outline of real CT images of the same patients mentioned above. Uniform activity and attenuation distributions with water equivalent (linear attenuation coefficient) were assumed (same as for the cylinder and ellipse images). For each image slice along the body axis a similar process was applied as for the cylinder and ellipse simulations. In the following we will refer to this simulation as “patient outline shape simulation”.

6.3.3 Acquisition Time Adjustment

To estimate the relative acquisition times along the axial direction of the body, a 4 cm diameter circular ROI was defined on each of the reconstructed emission Mean and SD images. For each slice the square of the SD divided by the Mean was calculated (i.e., $(SD/Mean)^2$) from the average pixel intensities of the defined ROI on both image sets. Using the slice with the average $(SD/Mean)^2$ value (among all slices) as a reference, the relative acquisition time that would yield a uniform SD/Mean for all slices was calculated as:

$$T_i = \frac{T_{total}}{n} \times \frac{(SD / Mean)_i^2}{(SD / Mean)_{ref}^2} \quad \text{Eq. 21}$$

where i means the slice number, T_{total} the total scan time and n the number of axial scan positions. As a reference value, the average $(SD/Mean)^2$ along the body axis was used:

$$(SD / Mean)_{ref}^2 = \sum_i (SD / Mean)_i^2 / n \quad \text{Eq. 22}$$

The use of average $(SD/Mean)^2$ as a reference value correlates with the practical implementation of the noise equalization method, when the length of the total scan time kept the same as for the conventional scan (without the use of noise equalization). A new set of images (Mean and SD) was generated, where the acquisition time was adjusted according to Equation 22. The ROI analysis was repeated to ensure that the adjustment of the acquisition time would result in uniform SNR axially. The correlation between the SD/Mean and the average attenuation correction factor (averaged over all angles) passing through the center of the body was also investigated. If there is a correlation, then this could be used to quickly estimate the relative acquisition times.

6.3.4 Phantom and Patient Scans

Based on the results from the simulations, a PET scan with a set of different diameter phantoms was acquired on the Siemens Biograph 64 Truepoint PET/CT system. Three cylinders with different diameters (7.4 cm, 17.5 cm and 21.0 cm), a NEMA image quality phantom with no activity in the spheres or in the lung insert, and an Anthropomorphic Phantom (Data Spectrum Corporation, Hillsborough, NC), with no activity in the lungs and the liver and without the cardiac insert, was filled with ^{18}F -Fluoro-Deoxy-Glucose (i.e. ^{18}F -FDG), with activity concentration of $0.163 \pm 0.002 \mu\text{Ci/mL}$ at the start of the acquisition. The phantoms were placed on the scanner bed in the order indicated on Figure 25. A 300s list mode dataset was acquired of each cylinder from which 20 bootstrap replicates (120s and variable times) were generated. For noise estimation we used the bootstrap method, since in this case the resulting noise patterns correlate well with the results of repeated measurements [50].

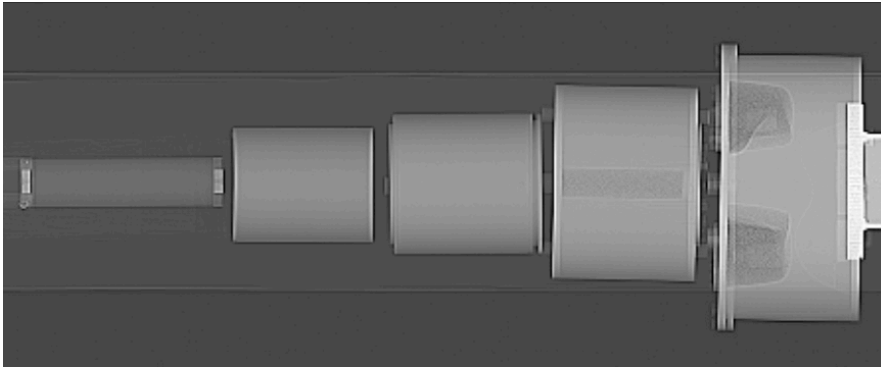


Figure 25. Topogram of the phantom set used for the study. The figure shows in order from left to right: Small, Medium and Large cylinders (diameters: 7.4, 17.5, 21.0 cm respectively), NEMA Image Quality Phantom and the Anthropomorphic phantom.

Each bootstrap replicate was reconstructed using OSEM (4i8s with a 2mm post reconstruction Gaussian filter). Mean and SD images were generated pixel-by-pixel from the set of replicate images. A 4 cm ROI analysis was performed for both the Mean and SD images and central average AC factors were also calculated from the CT derived attenuation correction. A patient scan was also acquired (5 bed positions, 240s each). Data were acquired as prompts and randoms, from which a pseudo-list mode data set was generated. Using the pseudo list mode data set, 20 bootstrap replicates (120s and variable times) were generated. Each replicate was reconstructed using OSEM (4i8s with a 5mm post reconstruction Gaussian filter) from which Mean and SD images were generated.

7. Results

7.1 Performance Comparison of the MiniPET-2 and MiniPET-3 preclinical PET systems

7.1.1 Position encoding and energy resolution

The flood field images of both MiniPET scanners are shown in Figure 26. These images illustrate the difference between the position mapping capabilities of the LYSO crystal elements when used with PMTs versus SiPM detectors. Although the position map of MiniPET-2 seems to be more homogenous, fewer crystals can be identified at the border area. On the other hand, non-uniform patterns can be seen in the MiniPET-3 position maps. This effect is due to the periodically changing overlaps between the crystal elements and the sensitive area of SiPMs. Moreover, some of the crystal elements are arranged in 3x3 clusters overlapping the SiPM sensors, while other crystal elements are located in between the sensitive areas of SiPM sensors.

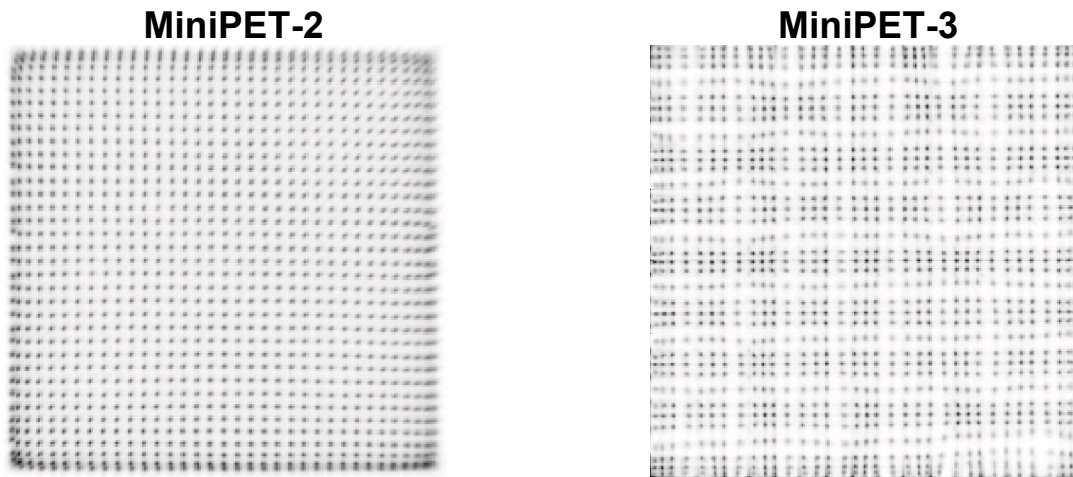


Figure 26. Position maps of the MiniPET-2 (left) and the MiniPET-3 (right) scanners.

Two representative profiles from both MiniPET-2 and MiniPET-3 position maps are shown in Figure 27. The average top/valley (T/V) ratios for the MiniPET-2 and MiniPET-3 detector modules are 5.20 ± 0.21 and 5.73 ± 1.03 , respectively. The highest T/V of the MiniPET-3 is more pronounced if we consider only the crystals in the high light collection position. In this case the average T/V is 6.6 ± 0.43 .

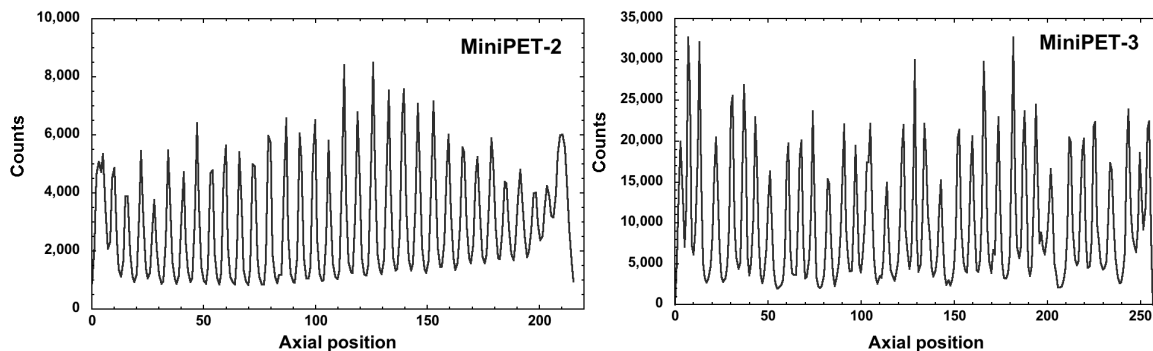


Figure 27. Line profiles of the MiniPET-2 and the MiniPET-3 scanners.

The energy spectra for each crystal position were also investigated and the related energy resolutions were calculated. For both MiniPET systems the energy resolution value related to each crystal element in case of two representative detector modules are displayed in Figure 28. The system average energy resolution values were measured to be $19.98 \pm 7.59\%$ and $31.74 \pm 11.30\%$ for the MiniPET -2 and MiniPET-3 respectively. The energy resolution pattern of the MiniPET-3 correlates well with the flood field image. Furthermore, the energy resolutions are higher for the crystal positions with high light collection and lower for the crystal positions with low light collection.

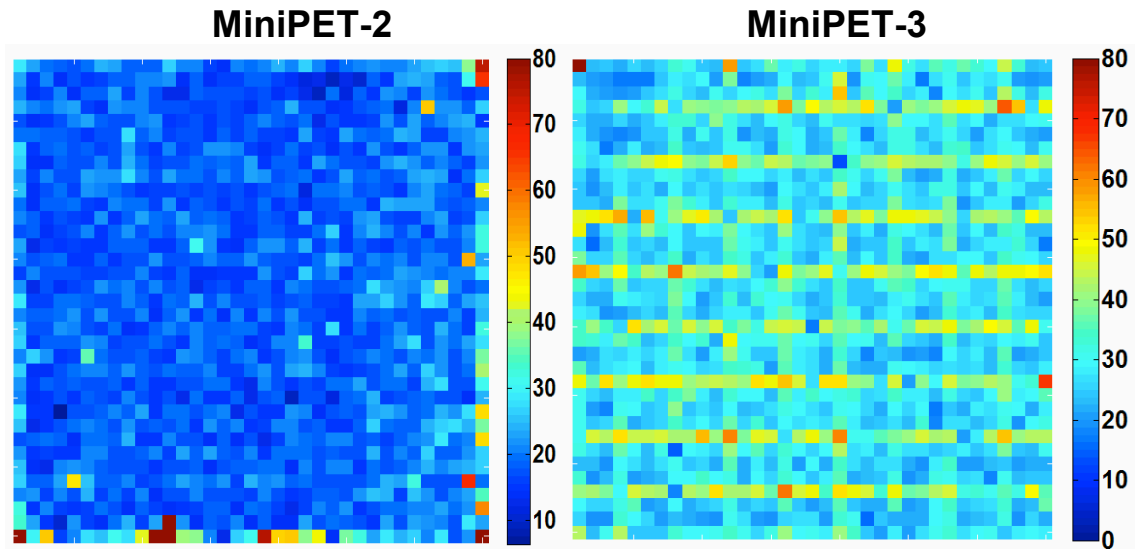


Figure 28. Energy resolution maps of the MiniPET-2 scanner and the MiniPET-3 scanner are displayed.

7.1.2 Coincidence Time Window

The timing offset values were precisely calculated and the time alignment method was applied for the 18 detector connections. This resulted a series of aligned coincidence spectra including all the detector connections (Figure 29).

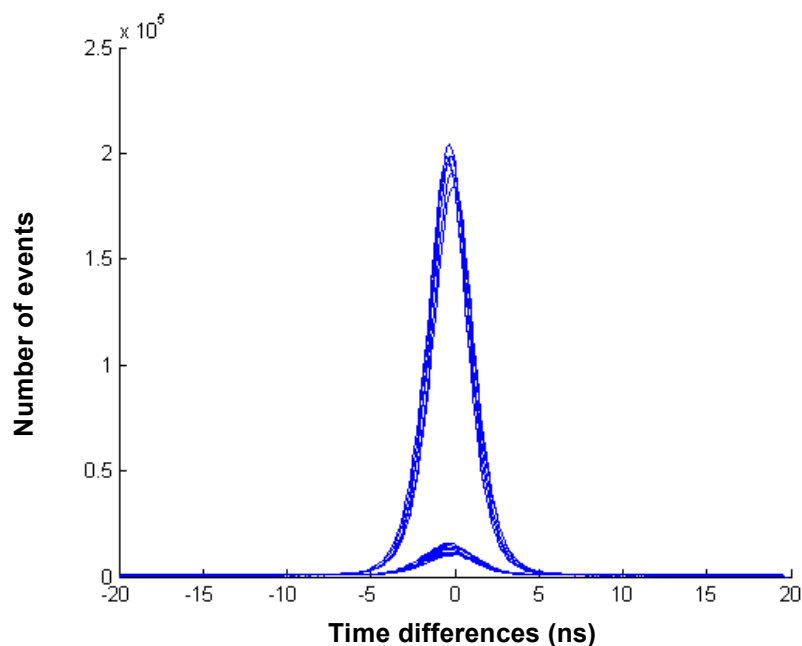


Figure 29. Coincidence spectra of the 18 detector connections after using the time alignment method.

The coincidence time window optimization resulted a plateau of the true coincidence rate starts between 8 ns and 12 ns (Figure 30), while the random coincidence rate is reasonably low within this range. The NEC-like measure had a maximum value close to 8 ns as observed in Figure 30. Therefore, the default τ -value was set to 8 ns to keep the random/true coincidence rate as low as possible near the close-to-optimal true event rate. In the case of the MiniPET-2 system, the optimal τ -value was found to be 6 ns based on former measurements [14].

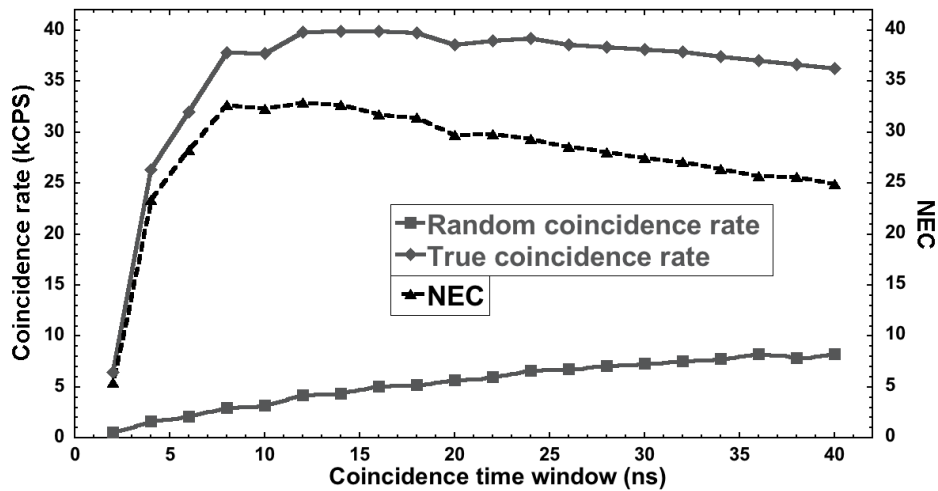


Figure 30. Coincidence Timing Window dependence on Random, True and NEC-like ($True^2/(True+2*Random)$) count rates for the MiniPET-3.

7.1.3 Spatial Resolution and Sensitivity

Spatial resolution was also measured using the FWHM of the radial, axial and tangential profiles as a function of radial distance from the axial center for MiniPET-2 and MiniPET-3 scanners at the $\frac{1}{4}$ offset from the axial center as seen in Figure 31 and 32. These values were found to be about 17% better, on average, for the MiniPET-3 system compared to the MiniPET-2. The minimal value of spatial resolution for all three directions (radial, tangential, axial) is approximately 1.35 mm for the MiniPET-2 at the center, increasing to 2.33 mm at the radial edge.

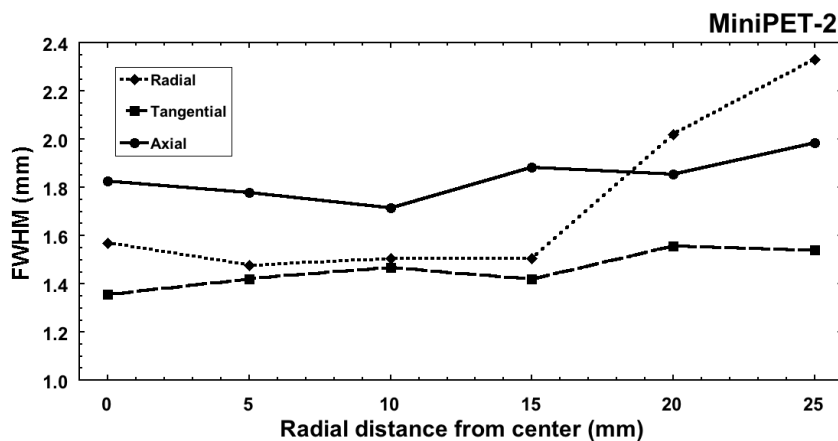


Figure 31. Dependence of the FWHM values on the radial distance, at the $\frac{1}{4}$ from the axial center for the MiniPET-2 scanner.

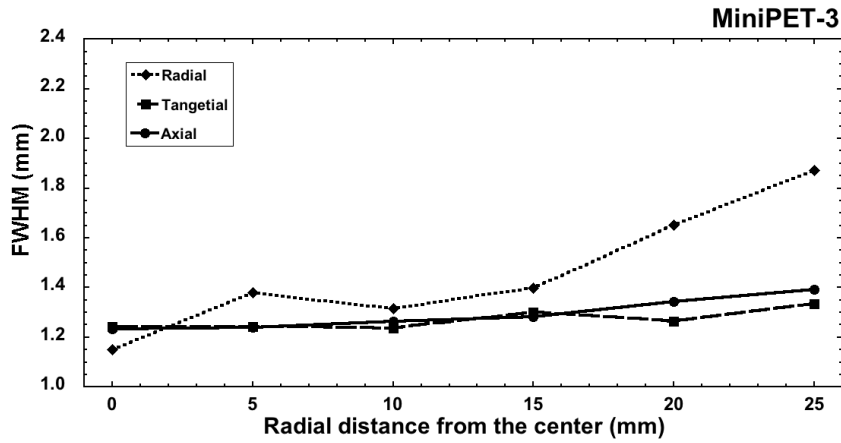


Figure 32. Dependence of the FWHM values on the radial distance, at the $\frac{1}{4}$ from the axial center for the MiniPET-3 scanner.

On the other hand, the minimal spatial resolution of the MiniPET-3 was approximately 1.15 mm and increased to 1.87 at the radial edge. The effective transaxial FWHM spatial resolution proposed by Goertzen et al. [10] was found to be 1.34 mm and 1.25 mm for the MiniPET-2 and MiniPET-3 scanners, respectively.

TABLE 3. Spatial resolution, sensitivity, image quality and count rate performance results for both MiniPET systems.

Category	MiniPET-2	MiniPET-3
Energy window (keV)	350-650	360-662
Coincidence time window (ns)	6.0	8.0
Spatial resolution at $\frac{1}{4}$ CFOV		
Tangential (mm)	1.36	1.24
Radial (mm)	1.57	1.15
Axial (mm)	1.83	1.23
Sensitivity		
Peak absolute sensitivity (%)	1.37	1.36
Total absolute sensitivity (%)	0.6	0.7
Image Quality		
Uniformity (%STD)	5.59	6.49
SOR air	0.15	0.14
SOR water	0.26	0.24
Count Rate Performance		
NEC-Peak (rat phantom)	14 kcps (at 36 MBq)	24 kcps (at 43 MBq)
NEC-Peak (mouse phantom)	55 kcps (39 MBq)	91 kcps (at 44 MBq)
Scatter Fraction (rat phantom)	17.4%	16.1%
Scatter Fraction (mouse phantom)	5.6%	4.8%

The axial absolute sensitivity profiles were also calculated as recommended in the NEMA NU 4. These results were similar for both systems. The peak absolute sensitivity and the total absolute sensitivity ($S_{A, \text{tot}}$) data are summarized in Table 2 for both MiniPET scanners.

7.1.4 Image Quality, Scatter Fraction and Count Rates

Three different sections of the NU-4 IQ phantom for both MiniPET-systems are displayed in Figure 33. The fillable rods are shown on the left, the uniform cylinder in the center, while the water and air chambers on the right.

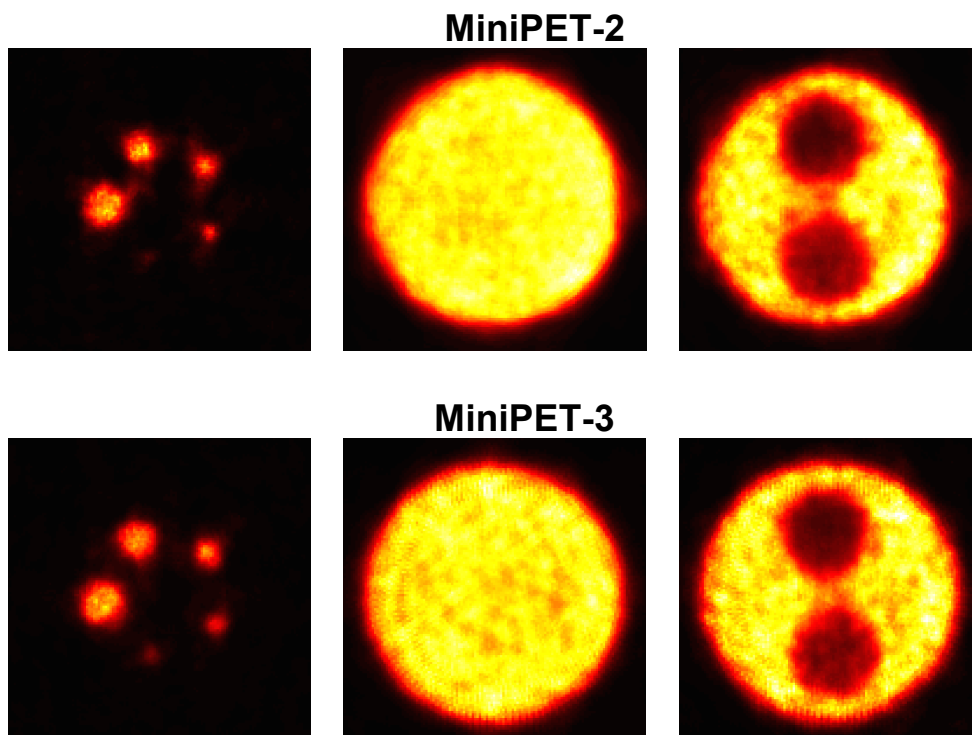


Figure 33. The reconstructed images of the NEMA NU 4 Image Quality phantom for the MiniPET-2 and MiniPET-3 scanners.

Note that the smallest rod is more visible in image acquired with the MiniPET-3 compared to that of the MiniPET-2. The SOR values found to be similar for both systems (~ 0.15 and ~ 0.25), while the uniformity was 5.59% in the case of MiniPET-2 and 6.49% in case of MiniPET-3 (Table 3). RC values showed comparable results for both of the MiniPET systems, while four rods showed slightly higher values in case of the MiniPET-3.

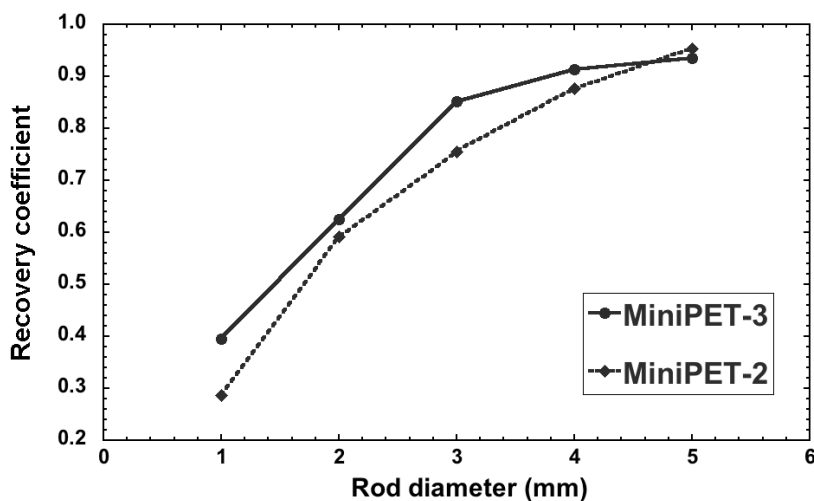


Figure 34. The corresponding RC dependences on the rod radius for the both scanners are also displayed(C).

The count rate performances measured with the larger phantom geometry on the MiniPET-2 and MiniPET-3 scanners are displayed in Figure 35 and 36.

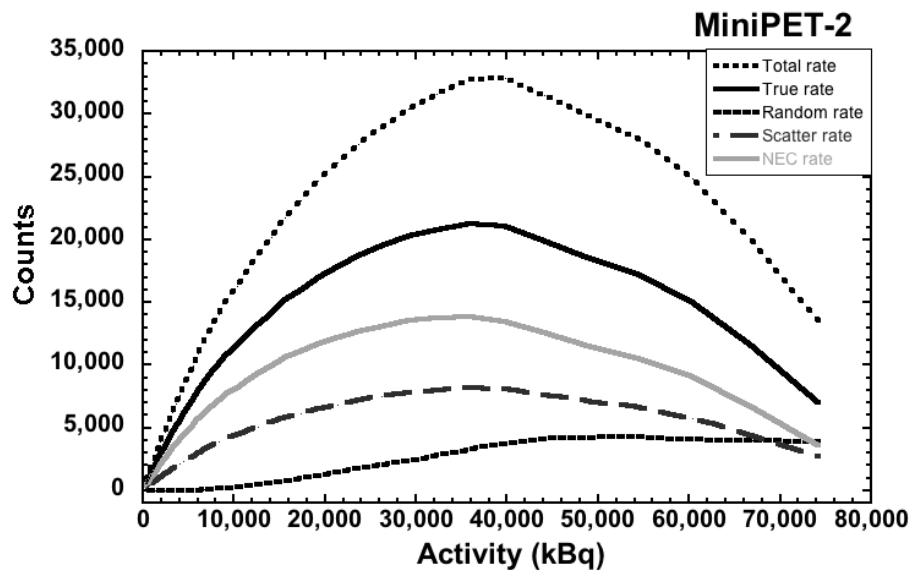


Figure 35. Count rate performance results measured with the NEMA NU 4 rat phantom for the MiniPET-2.

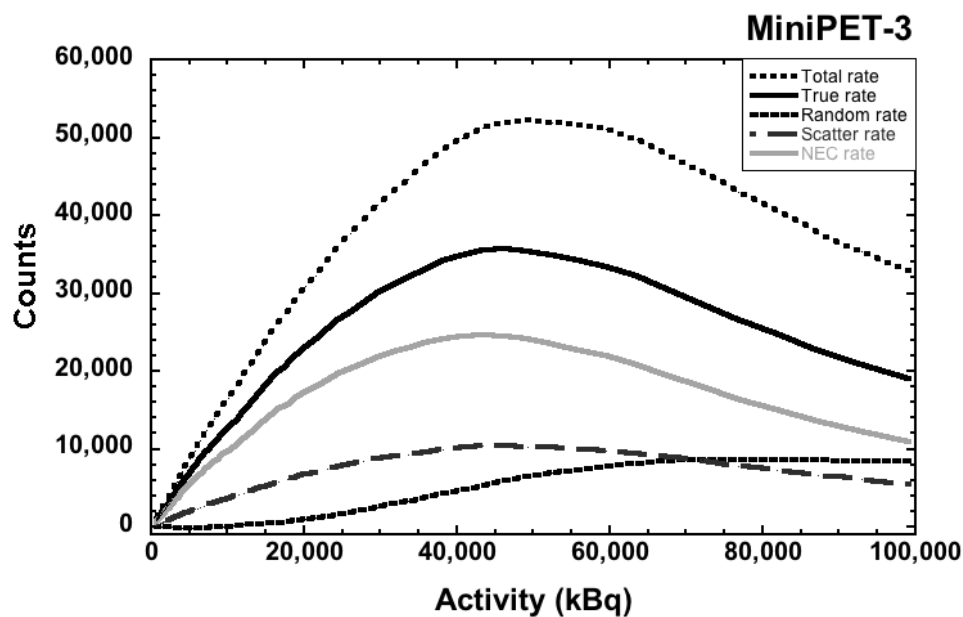


Figure 36. Count rate performance results measured with the NEMA NU 4 rat phantom for the MiniPET-3.

Although, we observed that the total count rate performances have a maximum around 50 MBq activity level for both scanners, the maximum accepted NEC count is approximately twice as high for the MiniPET-3 than for the MiniPET-2 (Figure 37). The NEC rate of the MiniPET-3 performs higher (better) than for the MiniPET-2, while the scatter fraction is slightly lower for the MiniPET-3 for both of the phantoms (Table 3).

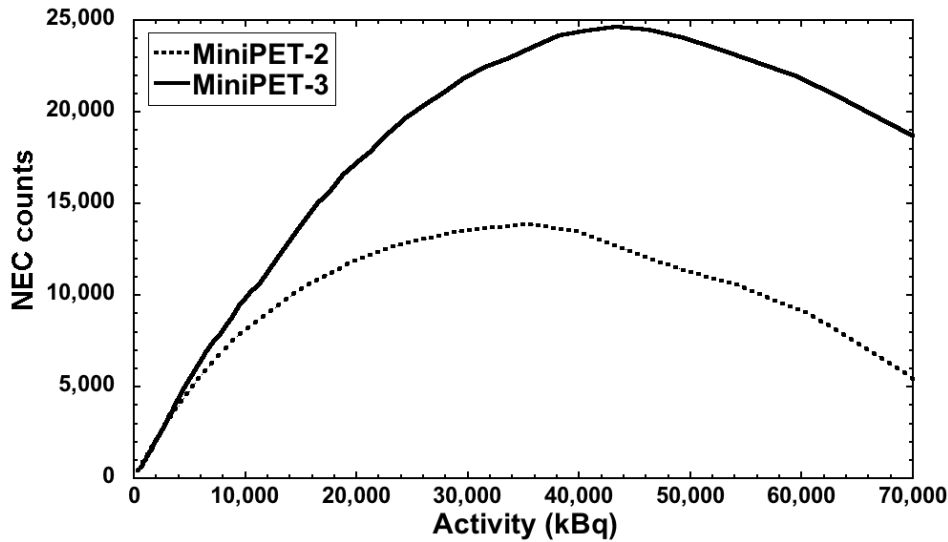


Figure 37. NEC Count rate performance results measured with the NEMA NU 4 rat phantom for the MiniPET-2 and MiniPET-3 scanners.

7.1.5 Small Animal Imaging Results

Axial, sagittal and coronal heart images of two different rats acquired on the MiniPET-2 (left) and MiniPET-3 (right) are displayed in Figure 33. The resolution and sensitivity of both scanners offers appropriate imaging conditions even to see the heart cavities. The rat studies revealed that the MiniPET-3 using SiPM photo-detectors offer comparable imaging capabilities than that of the conventional MiniPET-2 using PMTs.

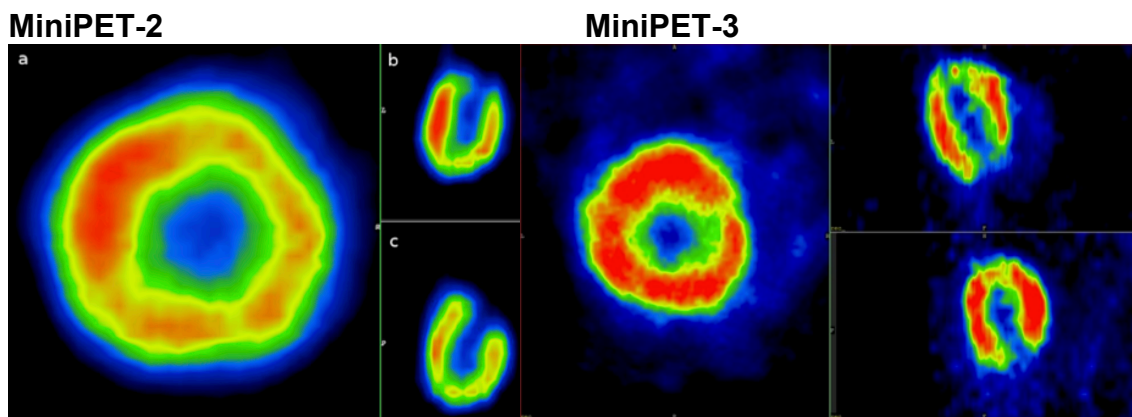


Figure 38. Heart images of two different rats acquired on the MiniPET-2 (left) and MiniPET-3 (right) systems. Axial (a), sagittal (b) and coronal (c) view images are displayed.

7.2 Human brain PET scanner simulation based on MiniPET concepts

7.2.1 Position maps and energy resolution

Representative position maps of the 21×21 detector matrix and the related profiles drawn on an arbitrary pixel rows are displayed in Figure 39. It can be seen that the peak/valley ratio is between five and ten, which is close to the MiniPET3 corresponding values. The average energy resolution of the system is $26 \pm 12\%$, which is less than the measured value (Figure 40).

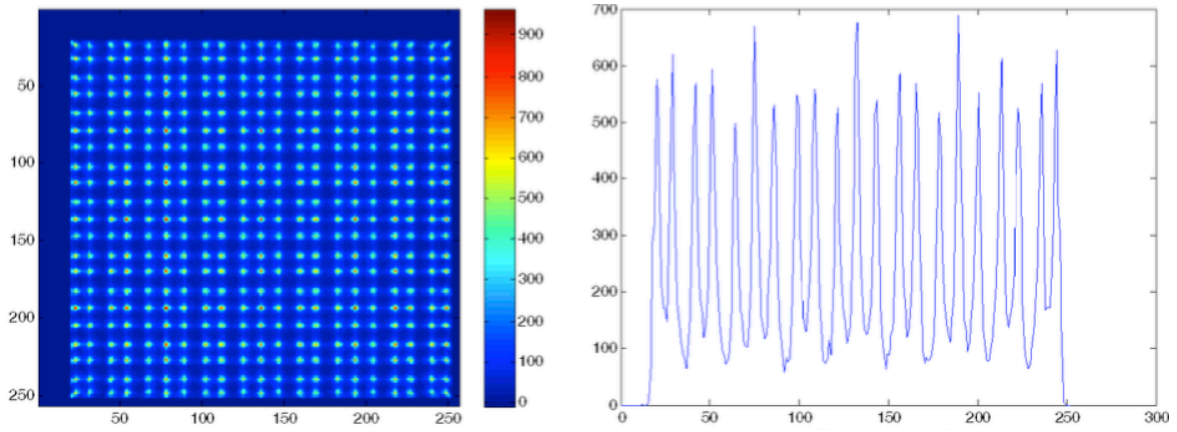


Figure 39. Simulated position map of a single detector module from the human brain PET scanner geometry (left) and a related line profile (right).

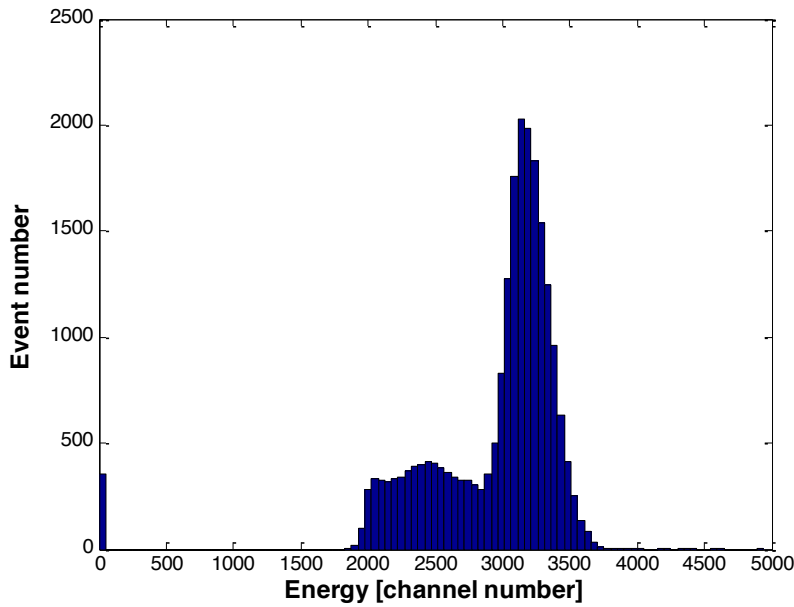


Figure 40. The relating energy distribution for a representative detector module of the simulated human brain PET scanner.

7.2.2 System count rate and sensitivity

Table 4. below displays the η_{si} , η_{true} parameters of the two simulated scanners and the MiniPET-3 camera (measured data). The table also shows the peak parameters of the estimated NEC curves. We found that the resulted scatter fraction was 27% for all geometry.

Table 4. Simulated human system count rate values compared that of the MiniPET geometry

Scanner geometry	η_{s}	η_{true}	NEC peak
smallFOV simulation	0.080	0.0014	37kcps (at 135 MBq)
largeFOV simulation	0.287	0.021	150kcps (at 38 MBq)
MiniPET-3 measured data	0.19	0.002	24 kcps (at 43 MBq)

The estimated count rate curves for the *smallFOV* and *largeFOV* simulations are shown in Figure 41 (Panels a and b). It can be observe that in the case of the extended axial field of

view the count rate saturation occurs at lower phantom activity but the maximal count is higher than the *smallFOV* simulation. In addition the random rate is higher at the *largeFOV* simulation.

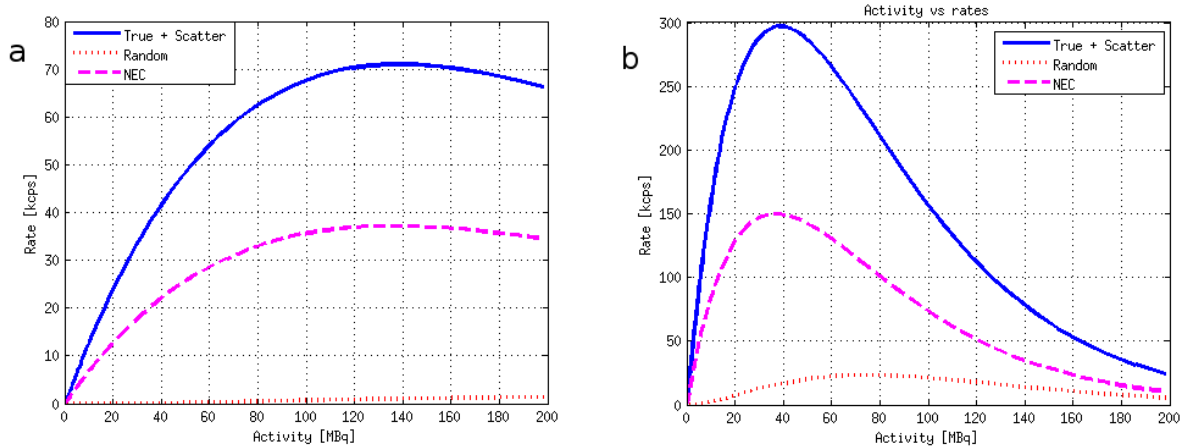


Figure 41. The estimated count rate curves for the *small FOV* geometry (Panel a) and *large FOV* geometry (Panel b) simulation.

We can conclude that if the physical radius of the MiniPET-3 is increased and larger scintillator crystals are used, the NEC parameters (peak count and activity) can be improved. Nevertheless, the sensitivity for the coincidence events of the system is reduced by 30%. Furthermore, the *largeFOV* simulation proves that the currently developed SiPM electronics and detector modules cannot process the increased amount data. Our calculation included one detector ring and only the number of crystals was increased ($\sim 4\times$ axial degree of MiniPET-3) while the data processing was performed only in one module (electronic).

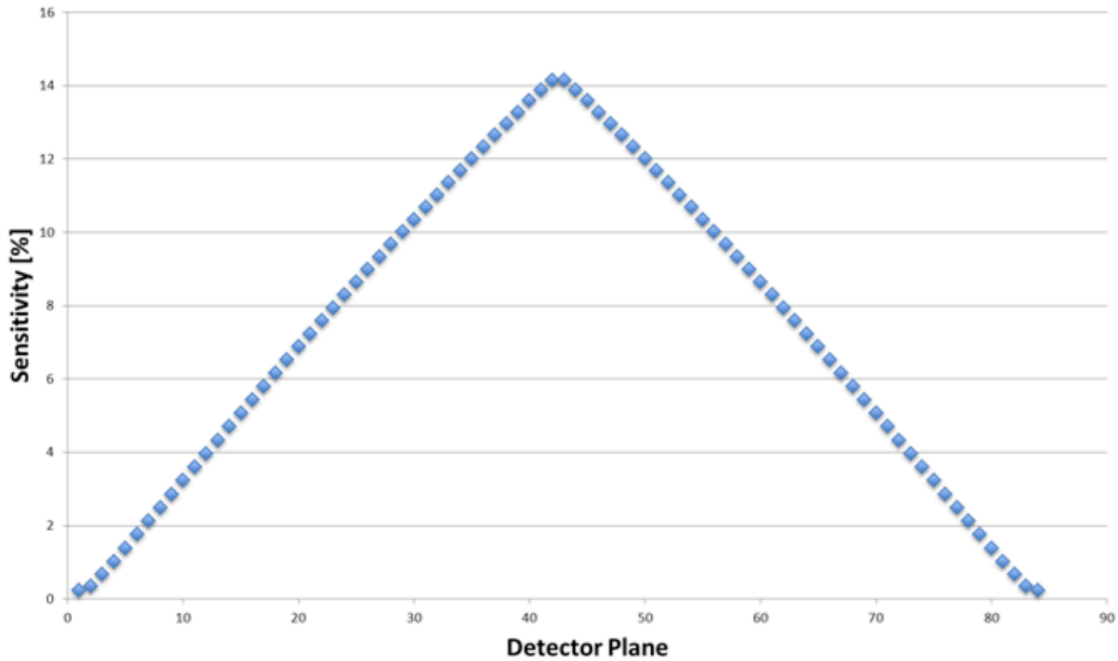


Figure 42. Axial sensitivity profile of the GATE simulated human brain PET scanner using the *largeFOV* geometry.

The system axial absolute sensitivity profile was calculated, as it is required in the NEMA NU 4. The axial sensitivity profile for the human brain PET camera with the *largeFOV*

geometry is displayed in Figure 42. The central sensitivity is $\sim 14\%$, which is definitely higher than the MiniPET-3 corresponding value, and very close to the theoretical 17.9% .

7.3 Whole body PET image SNR optimization using variable acquisition times

7.3.1 Simulations

The $(SD/Mean)^2$ plotted against the average central sonogram ACFs are displayed in Figure 43. The plot includes data for the circular simulations (green circles) and ellipse simulations (orange diamonds).

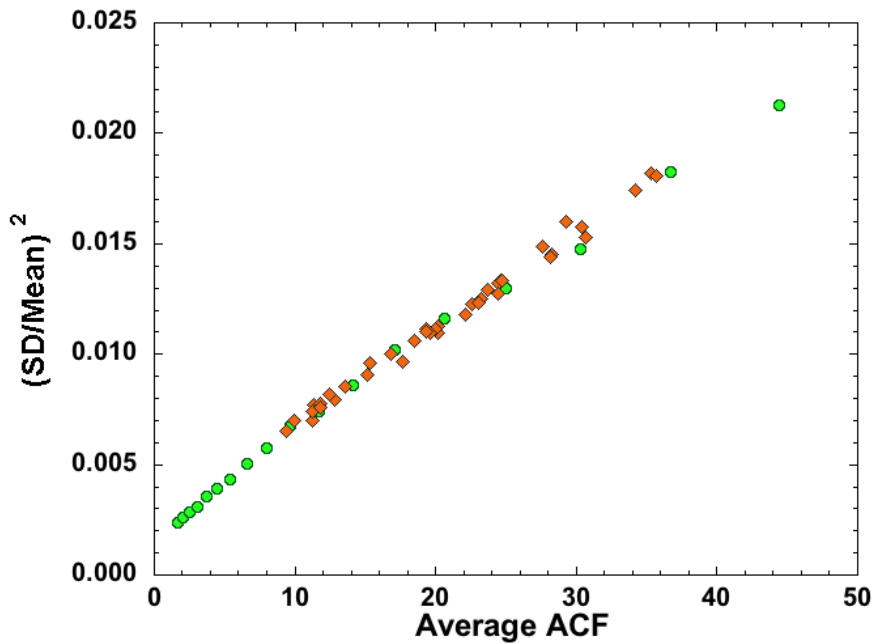


Figure 43. The square of the image noise plotted against the central average AC factors from the different diameter circular (green circles) and ellipse (orange diamonds) cylinder simulations.

Figure 44 indicates the results of the patient outline shape simulations where each marker refers to a subject of different weight categories (indicated with the different symbols as well: blue diamonds: 54.5kg, green circles: 72.6 kg, red circles: 95.3 kg, purple diamonds: 108.4 kg). A definite correlation can be recognized between image noise and the average AC factors regardless to the shape of the activity distribution. Figure 45 shows data from 4 simulations, based on patient CT images. Each colored marker indicates subjects with different weights (54.5-108.4 kg) in the same manner as on Figure 44. The data was fitted to a polynomial function, as indicated with a red line on Figure 45. The main difference between Figure 44 and 45 appears in the generating process of the images. The data presented on Figure 44 comes from homogenous activity distribution applied in-between the outline of the patients that came from CT scans (and therefore the attenuation correction factors also came from homogenous linear attenuation coefficient (μ -value) distributions. However, on Figure 45 we may see data from activity distributions applied on only the soft

tissue of the patients from segmentation of CT images (and μ -values were determined from the actual CT scans with the bilinear scaling method).

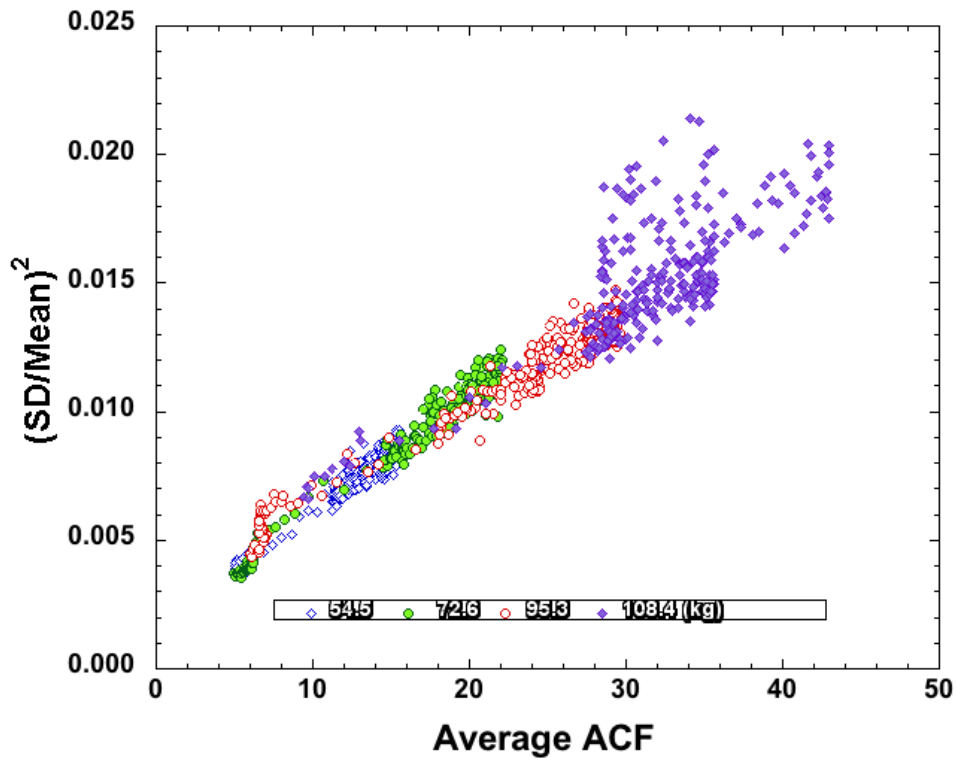


Figure 44. The square of the image noise plotted against the central average AC factors from the patient outline shape simulations where homogenous activity concentration was applied inside the outline of the patients determined from real CT images (subjects of 4 different weight category indicated with different colored symbols).

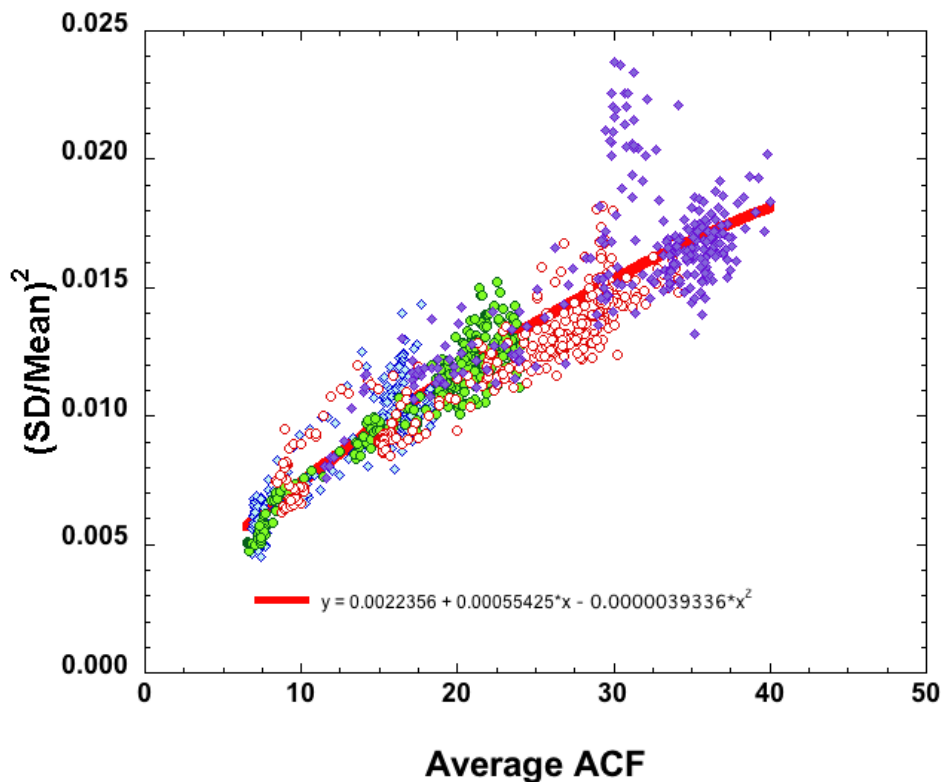


Figure 45. Simulation results for 4 different subjects resulted in a strong correlation between the square of the image noise ($SD/Mean$) and the AC factors. The data were fit to a polynomial function, as indicated with a red line in the figure. Each colored symbol refers to a different patient.

Figure 5 shows the image noise SD/Mean without equalization (orange circles) for a CT scan based simulation of a 73 kg patient. As expected, the noise level is the lowest in the head and neck region (slices 1-40) and highest in the abdomen (slices 175-235), where the attenuation is higher.

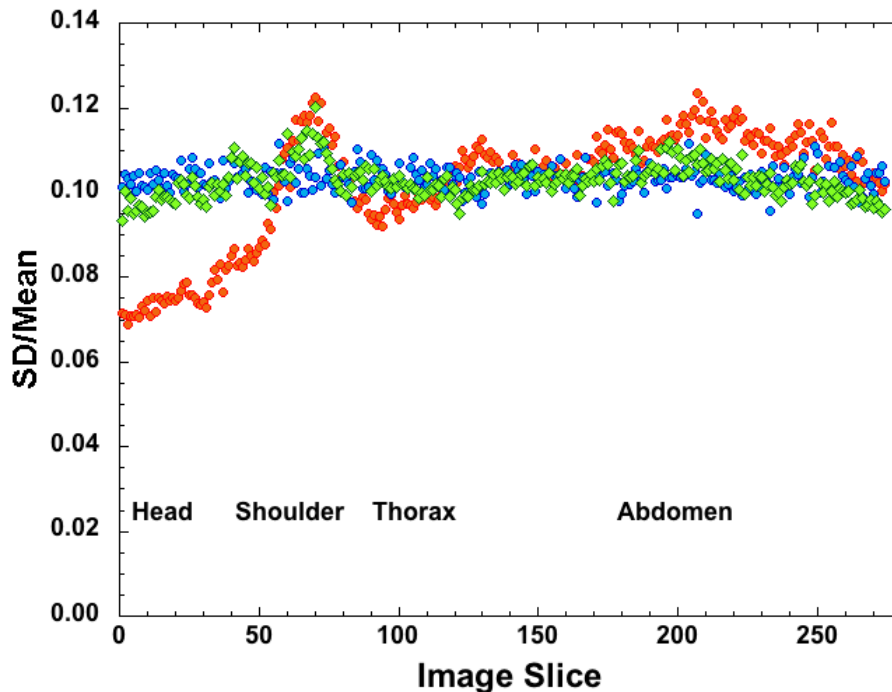


Figure 46. CT scan based simulation results for a 73 kg patient with $(SD/Mean)$ values for slices from the mid-brain to the upper thighs. The orange circles indicate $(SD/Mean)$ values if the same acquisition time was used for each slices. Results from the equalization method with use of equation (1) are shown with blue circles. Green diamonds indicate results when the correlation between $(SD/Mean)^2$ and the central AC factors from Figure 4 was used instead with equation (1) for the noise equalization method.

Using Equation 21 and the measured noise from the reconstructed noise replicates, the relative acquisition time (in form of the applied activity level on the image pixels) was adjusted. The resulting SD/Mean levels are shown as the blue circles in Figure 46. The green diamonds on the same figure refer to the resulting SD/Mean in case of using the correlation between the $(SD/Mean)^2$ and the average AC factors (the curve fit in Figure 45) and Equation 21. Both curves show a more uniform SD/Mean along the axial direction than the noise pattern resulted from the conventional method with no time adjustment (orange circles). The good agreement between the two equalized curves suggests that the Average ACF can be used to estimate the resulting image noise, at least in the case of a uniform activity distribution. The relatively flat noise pattern also indicates that this correlation can be used to adjust the acquisition time to equalize the image noise axially, in this simplified case.

7.3.2 Phantom and Patient Scans

The topogram in Figure 25 shows the positioning of the three different cylinders, the NEMA Image Quality phantom and the Anthropomorphic phantom in the scanner. $(SD/Mean)^2$ at

different positions within each phantom were derived from ROI analysis and are shown (in correlation with the AC factors generated from CT images of the scanner) as the orange diamonds in Figure 47.

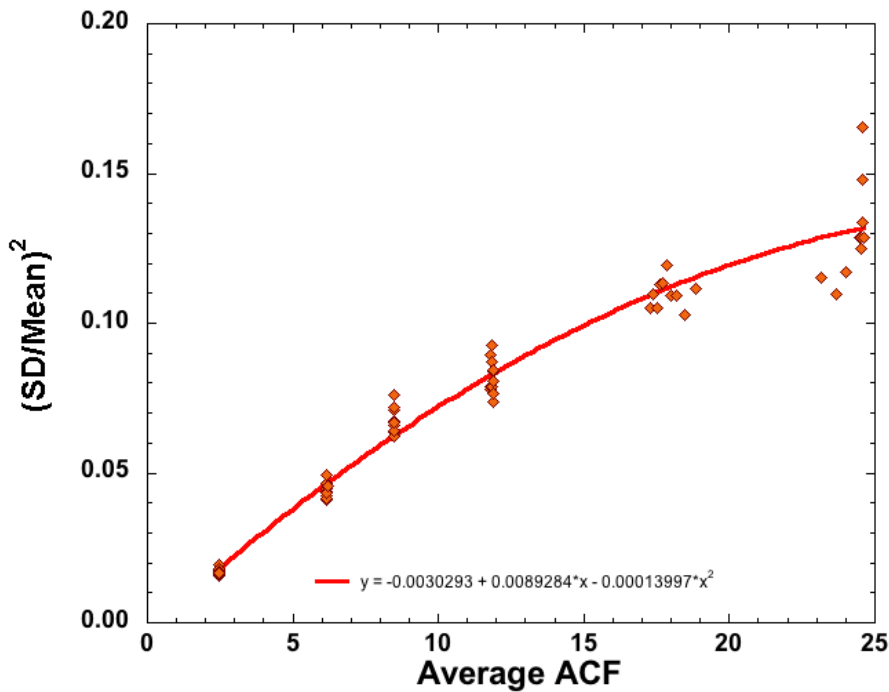


Figure 47. ROI analysis results (orange diamonds) from the Phantom measurement of different diameter cylinders, a NEMA IQ phantom and an Anthropomorphic phantom. Good correlation can be observed between the central AC factors and the $(SD/Mean)^2$ values and fitted with a polynomial function (red line curve).

The data were fit to a 2nd degree polynomial function, as shown in Figure 6 (red line curve). The SD/Mean for each phantom in case when the acquisition times are kept constant are shown in Figure 48 (orange diamonds). Using Equation 21 along with the measured correlation between $(SD/Mean)^2$ and the average ACFs (shown on Figure 47), the acquisition times that would yield a uniform image noise were calculated. Regarding the difference in fit parameters of the simulation (Figures 43 and 45) and the measured data (Figure 47) it should be mentioned that for the measured data we used the clinical reconstruction algorithm and parameters. For the initial simulation work we used different parameters. This should not make a significant difference, as long as the same reconstruction parameters are used as for the fit generation. To generate shorter/longer scan times, a smaller/larger fraction of prompt- and random counts were used in each bootstrap replicate. The resulting image noise curve is shown as the green circles in Figure 7, indicating equalized noise levels for the phantoms with different diameters.

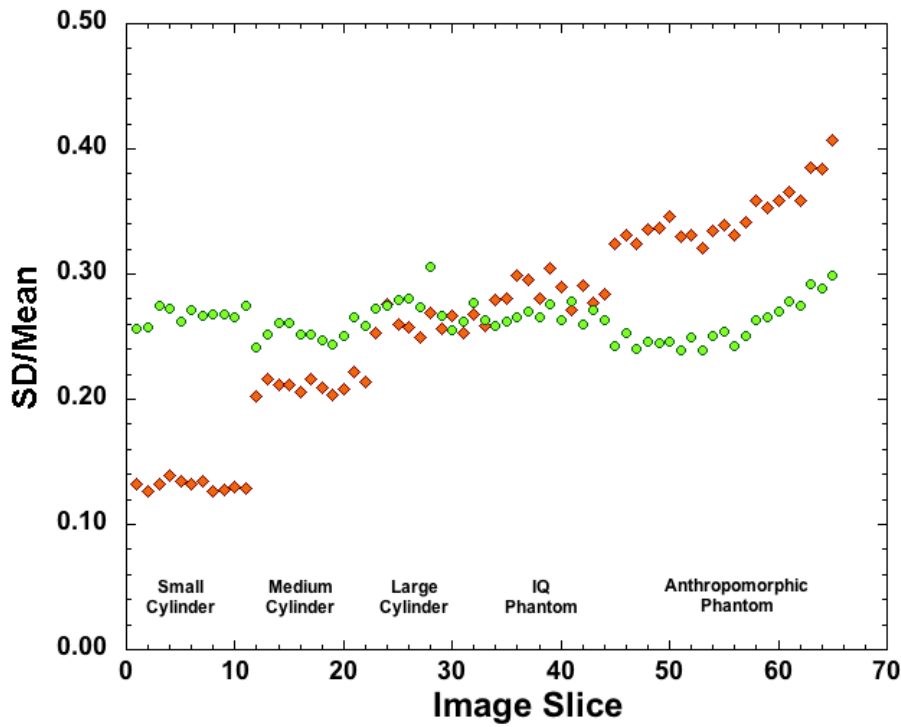


Figure 48. *SD/Mean values from ROI analysis for the Phantom Measurement, when the acquisition time for each bed position was kept fixed (gray diamonds). The black circles indicate results for the same phantom measurement, when the measured counts were adjusted to result equalized image noise. The correlation shown on Figure 6 between $(SD/Mean)^2$ and the central AC factors and equation (1) were used for the equalization method.*

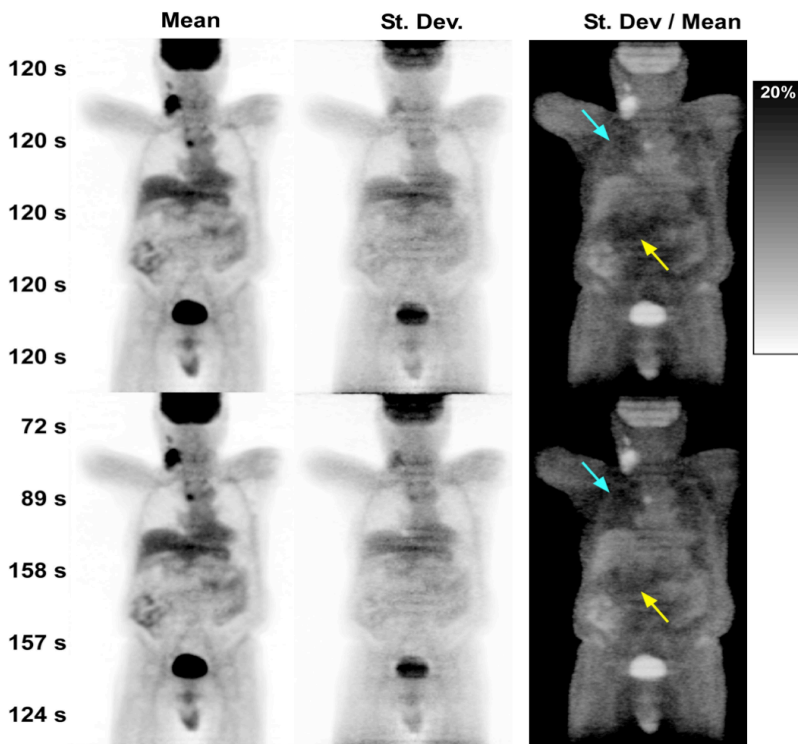


Figure 49. *Mean, Standard Deviation and SD/Mean images from an FDG whole body PET scan. The top row shows images with constant acquisition time in each bed position, the bottom row indicates images when the prompt and random counts were reduced or increased according to the correlation from Figure 47. No significant differences can be observed between the Mean images. SD/Mean is lower in the abdomen and higher in the thorax if the acquisition modulation is used instead of the conventional method.*

The top row of images in Figure 49 shows the resulting (from left to right) Mean, SD and SD/Mean images from a whole body FDG PET scan, where the acquisition time at each bed position was 120s. The lower row of images shows the corresponding images where the

acquisition time was adjusted according to the correlation between the Average ACF and $(SD/Mean)^2$. Although the Mean images do not show any appreciable difference, there are some visible differences in the SD/Mean images. Along the central axis the noise appears to be slightly more uniform. The image noise in the abdomen is reduced (yellow arrow) due to the longer acquisition time. Similarly, the image noise is higher in the lungs (blue arrow) due to the shortened acquisition time in this region.

8. Discussion

There have been many successful attempts for merging MRI systems with PET systems in recent years [57]–[60]. Some have reported on the performance parameters of SiPM-based full ring preclinical PET scanners or MRI inserts [58], [59], [74], [75]. However, only some of the NEMA NU 4 measurement protocols have been carried out on these systems. For a comprehensive comparison between a SiPM-based preclinical PET system and a conventional PMT-based system we performed all the necessary measurements recommended by the NEMA NU 4 standard on both MiniPET scanners. Comparison was facilitated by the fact that the SiPM-based MiniPET-3 and the PMT-based MiniPET-2 share nearly identical scintillation crystal geometry. Dark noise problems can be minimized if each SiPM matrix element has an individual signal-processing channel [58]–[60] but this solution would need a tremendous number of electronic channels. To reduce the number of channels, a special readout arrangement was developed in row-column manner for the SiPM matrix. In addition, appropriate weighting circuits were directly connected to the row and column outputs, allowing the 81 SiPM signals to be decoded into four outputs. From the flood-field images one can conclude that the MiniPET-3 performs about 1.5 times better in terms of peak-to-valley ratios compared to the MiniPET-2. In addition, discrepancies in light sharing for the two photo-detectors may explain the performance differences in spatial resolution between the two systems. Moreover, the MiniPET-3 exhibits superior axial, radial, and tangential spatial resolutions. This improvement is even more pronounced as the source is moved towards the radial edges. The overall axial system sensitivity shows similar characteristics between the systems as expected from the nearly identical scintillation crystal material and geometry. The image quality study is currently used as the gold standard for determining imaging characteristics of many preclinical PET systems [10], [12], [14], [71], [76], and showed similar results in terms of RC and SOR values for both MiniPET scanners. Better spatial resolution results in noisier images for the same number of counts, which explains the worse uniformity for the MiniPET-3 system. The NEC count rate peak values occur at similar activity levels, around 50 MBq for both scanners, however, these values are lower for the MiniPET-2. This is primarily because of the significantly higher dead time factor for the MiniPET-2 (680 ns) versus the MiniPET-3 (250 ns). The inferior dead time of the MiniPET-2 is a result of differences of the front-end electronics in the pulse shaping of the front-end preamplifiers as well as digital processing of each signal. The calculated scatter fractions from both the rat-sized and mouse-sized phantom experiments show comparable results, while the MiniPET-3

performs slightly better and that correlates with the somewhat better SOR values (Table 3). This seems to contradict the fact that the energy resolutions for the two systems are not the same. Indeed, the average energy resolution is about 32% (instead of 20%) for the SiPM-based system, 60% worse compared to the PMT-based system. One reason for this discrepancy is that, the calculated SF defined by the NEMA NU 4 protocol does not represent all the scattered events. In fact, it only includes only the photons scattered in the body. In addition, for preclinical PET scanners the number of scatters is definitely higher in the scintillation crystal than in the tissue (about 50% vs 10%) [43], thus the energy blurring has even less effect. A second explanation for the surprising scatter fraction results is that, no significant correlation could be found between the SF and the energy resolution in case of other preclinical systems [10]. The main disadvantage of the MiniPET-3 compared to the MiniPET-2 is the known dependence on ambient temperature of the semiconductor-based detectors [77], [78]. A limitation of this study is that we did not take into account the performance of the scanners in high magnetic fields. However, other research groups have proved the stability and proper performance of SiPMs in MRI systems already [74], [75]. Although both MiniPET systems have a relatively small FOV compared to other preclinical PET scanners [10], [11], [71], the main goal of this study was to compare SiPM with PMT technology while scanner scintillation crystal geometries, system matrices, slice rebinning algorithms, and even image reconstructions are kept identical.

Besides the performance and image quality comparison of the PMT and SiPM based preclinical PET systems, the possibility of a human brain scanner was proposed using the findings of the MiniPET concepts. There have been some limitations of these simulations as follows: the planned simulation to estimate the brain PET spatial resolution, which has not been finished, because of the unexpected computing task. The SiPM based simulation would require the inclusion of the optical photon process to the simulation chain, which dramatically increased the necessary calculation time in the GATE environment of the full ring detector system. If we wanted to use a point source with an activity of 1 MBq for a 1 sec acquisition to the above human PET system, the necessary calculation time is about 0.2 sec without simulating the optical photon process. If we apply the optical photon simulation for the same simulation case, the necessary time will be approximately 200 days. Currently we can use ~100 threads from the HPC which could be 1560 maximum. This is a factor of ~ 10 thus the minimum time to perform the simulation task is about $200/10 = 20$ days. To simulate a more complex phantom geometry such as the NEMA IQ phantom building up with at least 10000 point source, the necessary calculation would take at least 100 years.

Acquisition time plays an important role in producing PET images of high diagnostic quality. Conventional scanning protocols use adjustment of the total scan time according to

patient weight or body-mass-index (BMI) for this purpose. However, optimization for regional image noise of a single scan is not yet taken into account. We have shown in phantoms and in a patient scan that a more uniform noise pattern can be achieved by varying the scan time. Although varying the scan time did not produce an appreciable change in image quality for the patient study, the proposed technique may improve visualization of low activity lesions particularly in sections of the body with high absorption. In this work we focused only on the reliability of the main concept of axial noise equalization and present few patient data. For clinical validation a more comprehensive study should be performed including numerous patient data and probably additional computer simulations. Regional image noise can be made more uniform by adjusting the acquisition time at each bed position instead of using a fixed scan time. The acquisition time can be reduced in areas of lower attenuation (such as head, neck or thorax) and increased in more absorbing sections of the body (abdomen). The adjustment should be in inverse proportion to the square of the image noise. We have shown that there is a correlation between image noise (for uniform activity distributions) and the AC factors (derived from a CT scan). Using this relationship, the relative acquisition times can be quickly estimated routinely in the following manner. As a first step a bed position average of the ACF values shall be calculated, then the appropriate $(SD/Mean)^2$ determined using Figure 47. From the estimated noise levels at each bed position the time adjustment can be calculated with Equations 21 and 22. These relationships are partly based on the assumption of Poisson statistics of the reconstructed image. The presumed Poisson noise is obviously valid in the projection data, but this may not be correct in the reconstructed image due to the applied iterative reconstruction algorithms (such as OSEM) and the lower count rate statistics in the case of higher attenuating regions of the patients. This effect can be observed as higher deviations at ACF values larger than 30 in Figure 44 and 45, however, the overall impact of the method seems to be reliable. The axial noise equalization of our method works properly as can be seen on Figures 46 and 48. In addition, there is a potential drawback of this approach in areas where there might be a rapid change in attenuation axially (head and neck region), where acquisition time might be underestimated because the bed position average ACF will be too low. A refinement of the algorithm should probably include a check where the ACFs vary rapidly axially to ensure that risk for this is reduced. On the other hand, if continuous bed motion becomes widely available for human Whole Body PET scanners instead of the conventional fixed step bed motion, our method might work properly since the noise levels can be estimated with this new technique in each axial image planes that covers most or all of the body of the patient. For clinical practice reasons we chose the reference value in Equation 22 to result no differences in the total scan time between the new and the

conventional method. However, there are alternative approaches using Equation 21 selecting other reference values. For example, if the lowest SD/Mean value is selected the image noise in the higher absorbing regions will be decreased, although, the total acquisition time would be dramatically extended in this case. A limitation of this work is that we have only considered the time adjustment based only on the average central AC factors which is a simplification. Alternate methods could be applied such as using the prompt, random and single count rates of the actual bed position from a short, previous PET scan. In addition, we used uniform activity distributions to determine the correlation between the AC factors and image noise. Nevertheless, non-uniform activity distributions (such as in the clinical case) may lead to weaker correlation between the image noise and the average ACF in our method. Therefore, a more refined algorithm should also take into account the activity uptake and distribution.

9. Summary

Positron Emission Tomography is a very sensitive imaging method that reached worldwide use both in clinical hybrid techniques (combined with CT or MRI) or preclinical applications. New semiconductor photo-detector technologies (i.e. SiPM) play an important role in hybrid imaging and the improvement of image SNR. A preclinical PET system, the MiniPET-3 uses state-of-the-art SiPM photosensors was constructed in our institutions. We compared the MiniPET-3 with the MiniPET-2, a system with the same crystal geometry but conventional PMTs. The standard measurements proposed by the NEMA NU 4 protocols were performed on both systems. Spatial resolution was approximately 17% better on average for the MiniPET-3 than the MiniPET-2. The systems performed similarly in terms of peak absolute sensitivity ($\sim 1.37\%$), SOR for air (~ 0.15), SOR for water (~ 0.25), and RC ($\sim 0.33, 0.59, 0.81, 0.89, \text{ and } 0.94$). Uniformity was 5.59% for the MiniPET-2 and 6.49% for the MiniPET-3. The peak noise-equivalent counting rate was 14 kcps on the MiniPET-2 but 24 kcps on the MiniPET-3 using the larger phantom geometry. The optimal coincidence time window was 6 ns for the MiniPET-2 and 8 ns for the MiniPET-3. Based on these results we can conclude that the MRI-compatible SiPM-based MiniPET-3 scanner shows comparable results with the conventional technology producing images of high quality for small animal imaging. In addition, we performed computer simulation of a human brain PET based on the MiniPET concept scanner and determined position maps, energy resolution, system sensitivity and count rate performances.

We investigated the possibility of varying the acquisition time at different sections of the body such that the image SNR is kept relatively constant for all slices. To estimate the acquisition times for the different sections of the body we propose to use the AC sinogram generated from the CT scan that is acquired prior to the PET scan. Both simulations and phantom measurements of different diameter cylinders with activity distributions were performed. The image noise was estimated in every pixel from multiple replicate image sets. A simple polynomial function was found for both the simulations and the phantom measurement images to accurately describe the image noise as a function of AC factors. The findings of this work indicate that regional image SNR of human Whole Body PET scans can be made more uniform axially by adjusting the acquisition time per bed position according to the amount of attenuation. Instead of using a fixed scan time for each bed position, the acquisition can be extended in areas of high absorption and shortened in less absorbing sections of the body. The relative acquisition times can be quickly calculated using a simple functional relationship between image SNR and the AC factors.

10. Acknowledgements

First of all I am grateful for my mentor and teacher Dr. Laszlo Balkay. Thank you for believing in me and that I will be able to reach the goals we set up together. I always surprised by the fact that there is still so much I can learn from you.

I would like to express my greatest gratitude to my parents József and Ildikó Krizsán, along with my whole family: Dávid, Kriszti, Viktória, Péter, Benjámín, Adrienn, Kristóf, Etus, Mirjám, Zsombor, Énók and Zétény. I am more than grateful for your encouragement and how much you believed in my success.

I would like to express my gratitude to Helen Olah, my second mom for the tremendous help and support during the period of my work. Without you I could not reach these goals.

Special thanks to my best friends: Gábor Áron Takács and Eszter Kovács Takács, Béla and Ági Fiser, Francesco Azzolina and Klára Azzolina-Takács, Adam and Klarissza Vas, Benjámín Szabó, Csaba and Szilvia Szilágyi. Your support always helped me forward to complete what I have started.

I thank Dr. József Varga as making possible the research in the Department of Nuclear Medicine. I thank Magnus Dahlbom and Johannes Czernin for their great help and support in the first year of my research work.

I thank my colleagues Dr. Lajos Trón, Dr. Miklós Emri, Dr. Gabor Opposits, Dr. Sandor Attila Kis, Dr. Imre Lajtos, Dr. Tamás Spisák, László pohubi, Edit Györffiné Kovács, Ana Lima Oubina, Csaba Aranyi and Mariann Nagy for their strong support and handling patiently even my bad mood in the hardest days of the last four years.

Special thanks to Dr. György Trencsényi, Tamás Nagy, Judit Szabó Péliné, Dr. Ildikó Garai and Dr. László Galuska for the support and help. I thank to Dr. Pál Mikecz and the colleagues from the Radiochemistry Department for their help with the radiopharmacons for the experiments.

I give special thanks to Freddie Daver, Attila Forgács, Ferenc Nagy, Dávid Nagy and Mihály Zentai for the thoughtful conversations and great coffee times during the period of this work. These were such moments that made me feel that time was stopped.

11. Keywords

Positron Emission Tomography, MiniPET, Signal-to-Noise Ratio, SiPM, Image Quality, Whole Body PET Acquisition, Small-animal PET scanner, Image Reconstruction, Performance Evaluation, NEAMA NU 4, Instrumentation, Attenuation Correction, Molecular Imaging

11. References

- [1] S. R. Cherry and M. Dahlbom, "PET: Physics, Instrumentation and Scanners," in *PET, Molecular Imaging and Its Biological Applications*, M. E. Phelps, Ed. Springer, 2004.
- [2] N. Belcari, *Development of a Positron Emission Mammography scanner for breast cancer detection*. 2003.
- [3] P. Riccardi, R. Li, M. S. Ansari, D. Zald, S. Park, B. Dawant, S. Anderson, M. Doop, N. Woodward, E. Schoenberg, D. Schmidt, R. Baldwin, and R. Kessler, "Amphetamine-Induced Displacement of [18 F] Fallypride in Striatum and Extrastriatal Regions in Humans," *Neuropsychopharmacology*, vol. 31, pp. 1016–1026, 2006.
- [4] H. Stergar, A. Bockisch, S. Eschmann, B. Krause, R. Rödel, R. Tiling, and M. Weckesser, "Influence of PET/CT-introduction on PET scanning frequency and indications. Results of a multicenter study," *Nuklearmedizin*, vol. 46, pp. 57–64., 2007.
- [5] S. R. Meikle, D. L. Bailey, P. K. Hooper, S. Eberl, B. F. Hutton, W. F. Jones, R. R. Fulton, and M. J. Fuiham, "Simultaneous Emission and Transmission Measurements for Attenuation Correction in Whole Body PET," *J. Nucl. Med.*, vol. 36, no. 9, pp. 1680–1688, 1995.
- [6] D. W. Townsend, J. P. J. Carney, J. T. Yap, and N. C. Hall, "PET / CT Today and Tomorrow," *J. Nucl. Med.*, vol. 45, no. 1, pp. S4–S14, 2004.
- [7] J. A. Disselhorst, I. Bezrukov, A. Kolb, C. Parl, and B. J. Pichler, "Principles of PET / MR Imaging," *J. Nucl. Med.*, vol. 55, no. 6, p. 2S–10S, 2014.
- [8] J. Czernin, L. Ta, and K. Herrmann, "Does PET/MR Imaging Improve Cancer Assessments? Literature Evidence from More Than 900 Patients," *J. Nucl. Med.*, vol. 55, p. 59S–62S, 2014.
- [9] B. J. Pichler, M. S. Judenhofer, C. Catana, J. H. Walton, M. Kneilling, R. E. Nutt, S. B. Siegel, C. D. Claussen, and S. R. Cherry, "Performance test of an LSO-APD detector in a 7-T MRI scanner for simultaneous PET/MRI.," *J. Nucl. Med.*, vol. 47, no. 4, pp. 639–647, 2006.
- [10] a. L. Goertzen, Q. Bao, M. Bergeron, E. Blankemeyer, S. Blinder, M. Canadas, a. F. Chatziioannou, K. Dinelle, E. Elhami, H.-S. Jans, E. Lage, R. Lecomte, V. Sossi, S.

- Surti, Y.-C. Tai, J. J. Vaquero, E. Vicente, D. a. Williams, and R. Laforest, “NEMA NU 4-2008 Comparison of Preclinical PET Imaging Systems,” *J. Nucl. Med.*, vol. 53, no. 8, pp. 1300–1309, 2012.
- [11] Q. Bao, D. Newport, M. Chen, D. B. Stout, and A. F. Chatziioannou, “Performance evaluation of the inveon dedicated PET preclinical tomograph based on the NEMA NU-4 standards,” *J. Nucl. Med.*, vol. 50, no. 3, pp. 401–408, 2009.
- [12] R. Prasad, O. Ratib, and H. Zaidi, “NEMA NU-04-based performance characteristics of the LabPET-8TM small animal PET scanner,” *Phys. Med. Biol.*, vol. 56, pp. 6649–6664, 2011.
- [13] M. a Bahri, A. Plenevaux, G. Warnock, A. Luxen, and A. Seret, “NEMA NU4-2008 image quality performance report for the microPET focus 120 and for various transmission and reconstruction methods,” *J. Nucl. Med.*, vol. 50, no. 10, pp. 1730–1738, 2009.
- [14] I. Lajtos, M. Emri, S. a. Kis, G. Opposits, N. Potari, B. Kiraly, F. Nagy, L. Tron, and L. Balkay, “Performance evaluation and optimization of the MiniPET-II scanner,” *Nucl. Instruments Methods Phys. Res. Sect. A*, vol. 707, pp. 26–34, 2013.
- [15] A. J. Sinusas, F. Bengel, M. Nahrendorf, F. H. Epstein, J. C. Wu, F. S. Villanueva, Z. A. Fayad, and R. J. Gropler, “Advances in Cardiovascular Imaging Multimodality Cardiovascular Molecular Imaging , Part I,” *Circ. Cardiovasc. Imaging*, vol. 1, pp. 244–256, 2008.
- [16] R. Weissleder and M. J. Pittet, “Imaging in the era of molecular oncology,” *Nature*, vol. 452, no. April, 2008.
- [17] G. Brownell, C. Burnham, S. Silensky, and E. Al., “New developments in positron scintigraphy and the application of cyclotron-produced positron emitters,” *Med. Radioisot. Scintigr. Vienna, IAEA*, pp. 163–176., 1968.
- [18] G. Brownell and W. Sweet, “Localisation of brain tumors with positron emitters,” *Nucleonics*, vol. 11, pp. 40–45., 1953.
- [19] C. Burnham and G. Brownell, “A multicrystal positron camera,” *IEEE Med Sci NS*, vol. 3, pp. 201–205., 1973.
- [20] D. Chesler, “Positron tomography and three dimensional reconstruction techniques,” in *Tomographic Imaging in Nuclear Medicine*, F. GS, Ed. New York: Society of Nuclear Medicine, 1973, pp. 176–183.
- [21] D. Chesler, “Three-dimensional activity distribution from multiple positron scintigraphs,” *J Nucl Med*, vol. 12, pp. 347–348., 1971.

- [22] N. Dyson, "The annihilation coincidence method of localizing positron-emitting isotopes and a comparison with parallel counting," *Phys Med Biol*, vol. 4, pp. 376–390., 1960.
- [23] F. Wrenn, M. Good, and P. Handler, "The use of positron-emitting radioisotopes for the localization of brain tumors," *Science (80-.)*, vol. 113, pp. 525–527, 1951.
- [24] M. E. Phelps, E. J. Hoffman, N. a Mullani, and M. M. Ter-Pogossian, "Application of annihilation coincidence detection to transaxial reconstruction tomography.," *J. Nucl. Med.*, vol. 16, no. 3, pp. 210–224, 1975.
- [25] M. Dahlbom, E. J. Hoffman, C. K. Hoh, C. Schiepers, G. Rosenqvist, R. a Hawkins, and M. E. Phelps, "Whole-body positron emission tomography: Part I. Methods and performance characteristics.," *J. Nucl. Med.*, vol. 33, no. 6, pp. 1191–1199, 1992.
- [26] S. R. Cherry, "The 2006 Henry N . Wagner Lecture : Of Mice and Men (and Positrons)— Advances in PET Imaging Technology," vol. 47, pp. 1735–1745, 2006.
- [27] H. M. Hudson and R. S. Larkin, "Accelerated Image Reconstruction using Ordered Subsets of Projection Data," *IEEE Trans. Med. Imaging*, vol. 13, pp. 601–609, 1994.
- [28] J. Nuyts, P. Dupont, S. Stroobants, R. Benninck, L. Mortelmans, and P. Suetens, "Simultaneous maximum a-posteriori reconstruction of attenuation and activity distributions from emission sinograms .," *IEEE Trans. Med. Imaging*, vol. 18, no. 5, pp. 393–403, 1999.
- [29] H. O. Anger, "Survey of Radioisotope Cameras," *Trans. Instrum. Soc. Am.*, vol. 5, pp. 311–334, 1966.
- [30] T. F. Budinger, "Time-of-Flight Positron Emission Tomography: Status Relative to Conventional PET," *J. Nucl. Med.*, vol. 24, no. 1, pp. 73–78, 1983.
- [31] S. Surti, A. Kuhn, M. E. Werner, A. E. Perkins, J. Kolthammer, and J. S. Karp, "Performance of Philips Gemini TF PET/CT scanner with special consideration for its time-of-flight imaging capabilities.," *J. Nucl. Med.*, vol. 48, no. 3, pp. 471–480, 2007.
- [32] G. Akamatsu, K. Ishikawa, K. Mitsumoto, T. Taniguchi, N. Ohya, and S. Baba, "Improvement in PET/CT Image Quality with a Combination of Point-Spread Function and Time-of-Flight in Relation to Reconstruction Parameters," *J. Nucl. Med.*, vol. 53, no. 11, pp. 1716–1723, 2012.
- [33] G. Akamatsu, K. Mitsumoto, T. Taniguchi, Y. Tsutsui, S. Baba, and M. Sasaki, "Influences of point-spread function and time-of-flight reconstructions on standardized uptake value of lymph node metastases in FDG-PET," *Eur. J. Radiol.*,

- vol. 83, no. 1, pp. 226–230, 2014.
- [34] B. W. Jakoby, Y. Bercier, M. Conti, M. E. Casey, and B. Bendriem, “Physical and clinical performance of the mCT time-of-flight PET / CT scanner,” *Phys Med Biol*, vol. 56, pp. 2375–2389., 2011.
- [35] D. J. Kadrmas, M. E. Casey, M. Conti, B. W. Jakoby, C. Lois, and D. W. Townsend, “Impact of Time-of-Flight on PET Tumor Detection,” *J. Nucl. Med.*, vol. 50, no. 8, pp. 1315–1323, 2009.
- [36] L. Presotto, L. Gianolli, M. C. Gilardi, and V. Bettinardi, “Evaluation of image reconstruction algorithms encompassing Time-Of-Flight and Point Spread Function modelling for quantitative cardiac PET : Phantom studies,” vol. 22, pp. 351–363, 2015.
- [37] O. Rousset, A. Rahmim, A. Alavi, and H. Zaidi, “Partial Volume Correction Strategies in PET,” *PET Clin.*, vol. 2, pp. 235–249, 2007.
- [38] O. G. Rousset, Y. Ma, and A. C. Evans, “Principle and Validation,” *J. Nucl. Med.*, vol. 39, no. 5, pp. 904–911., 1998.
- [39] T. Beyer, D. W. Townsend, T. Brun, P. E. Kinahan, M. Charron, R. Roddy, J. Jerin, J. Young, L. Byars, and R. Nutt, “A combined PET/CT scanner for clinical oncology.” *J. Nucl. Med.*, vol. 41, no. 8, pp. 1369–1379, 2000.
- [40] B. W. Jakoby, Y. Bercier, C. C. Watson, B. Bendriem, and D. W. Townsend, “Performance Characteristics of a New LSO PET/CT Scanner With Extended Axial Field-of-View and PSF Reconstruction,” *IEEE Trans. Nucl. Sci.*, vol. 56, no. 3, pp. 633–639, 2009.
- [41] W. W. Moses, “Fundamental Limits of Spatial Resolution in PET,” *Nucl Instrum Methods Phys Res A*, vol. 648 Supple, pp. S236–S240, 2011.
- [42] M. D. Harpen, “Positronium: Review of symmetry, conserved quantities and decay for the radiological physicist,” *Med. Phys.*, vol. 31, pp. 57–61, 2004.
- [43] I. Lajtos, J. Czernin, M. Dahlbom, F. Daver, M. Emri, S. Farshchi-Heydari, A. Forgacs, C. K. Hoh, I. Jozsai, A. K. Krizsan, J. Lantos, P. Major, J. Molnar, G. Opposits, L. Tron, D. R. Vera, and L. Balkay, “Cold wall effect eliminating method to determine the contrast recovery coefficient for small animal PET scanners using the NEMA NU-4 image quality phantom.” *Phys. Med. Biol.*, vol. 59, no. 11, pp. 2727–46, 2014.
- [44] S. R. Cherry, J. A. Sorensen, and M. E. Phelps, *Physics in Nuclear Medicine*, 4th ed. Elsevier, 2012.

- [45] M. Vanderhoek, S. B. Perlman, and R. Jeraj, "Impact of the Definition of Peak Standardized Uptake Value on Quantification of Treatment Response," *J. Nucl. Med.*, vol. 53, no. 1, pp. 4–11, 2012.
- [46] C. Lartizien, C. Comtat, P. E. Kinahan, N. Ferreira, B. Bendriem, and R. Trebossen, "Optimization of Injected Dose Based on Noise Equivalent Count Rates for 2- and 3-Dimensional," *J. Nucl. Med.*, vol. 43, no. 9, pp. 1268–1278, 2002.
- [47] C. C. Watson, "Count Rate Dependence of Local Signal-to-Noise Ratio in Positron Emission Tomography," *IEEE Trans. Nucl. Sci.*, vol. 51, no. 5, pp. 2670–2680, 2004.
- [48] C. Lois, B. W. Jakoby, M. J. Long, K. F. Hubner, D. W. Barker, M. E. Casey, M. Conti, V. Y. Panin, D. J. Kadrmas, and D. W. Townsend, "An Assessment of the Impact of Incorporating Time-of-Flight Information into Clinical PET/CT Imaging," *J. Nucl. Med.*, vol. 51, no. 2, pp. 237–245, 2010.
- [49] D. R. Dance, S. Christofides, A. D. A. Maidment, I. D. Mclean, and K. H. Ng, *Diagnostic Radiology Physics, handbook for Teachers and Students*. 2014.
- [50] M. Dahlbom, "Estimation of Image Noise in PET Using the Bootstrap Method," *IEEE Trans. Nucl. Sci.*, vol. 49, no. 5, pp. 2062–2066, 2002.
- [51] J. B. Solomon, O. Christianson, and E. Samei, "Quantitative comparison of noise texture across CT scanners from different manufacturers Quantitative comparison of noise texture across CT scanners," *Med. Phys.*, vol. 39, no. 10, pp. 6048–6055, 2012.
- [52] I. Sechopoulos, K. Bliznakova, and B. Fei, "Power spectrum analysis of the x-ray scatter signal in mammography and breast tomosynthesis projections Power spectrum analysis of the x-ray scatter signal in mammography and breast tomosynthesis projections," *Med. Phys.*, vol. 40, no. 10, pp. 101905–1 – 101905–7, 2013.
- [53] A. Rahmim and J. Tang, "Noise propagation in resolution modeled PET imaging and its impact on detectability," *Phys Med Biol*, vol. 58, pp. 6945–6968, 2013.
- [54] R. Lecomte, "Novel detector technology for clinical PET," *Eur. J. Nucl. Med. Mol. Imaging*, vol. 36, no. SUPPL. 1, pp. 69–85, 2009.
- [55] M. S. Judenhofer and S. R. Cherry, "Applications for preclinical PET/MRI," *Semin. Nucl. Med.*, vol. 43, no. 1, pp. 19–29, 2013.
- [56] M. S. Judenhofer, H. F. Wehrl, D. F. Newport, C. Catana, S. B. Siegel, M. Becker, A. Thielscher, M. Kneilling, M. P. Lichy, M. Eichner, K. Klingel, G. Reischl, R. E. Nutt, K. Uludag, S. R. Cherry, S. Widmaier, M. Ro, C. D. Claussen, and B. J. Pichler, "Simultaneous PET-MRI : a new approach for functional and morphological imaging," *Nat. Med.*, vol. 14, no. 4, pp. 459–465, 2008.

- [57] A. Aguilar, R. García-Olcina, P. a. Martínez, J. Martos, J. Soret, J. Torres, J. M. Benlloch, A. J. González, and F. Sánchez, “Time of flight measurements based on FPGA and SiPMs for PET-MR,” *Nucl. Instruments Methods Phys. Res. Sect. A Accel. Spectrometers, Detect. Assoc. Equip.*, vol. 734, no. PART B, pp. 127–131, 2014.
- [58] B. Weissler, P. Gebhardt, C. W. Lerche, J. Wehner, T. Solf, B. Goldschmidt, J. E. Mackewn, P. K. Marsden, F. Kiessling, M. Perkuhn, D. Heberling, and V. Schulz, “MR compatibility aspects of a silicon photomultiplier-based PET/RF insert with integrated digitisation.,” *Phys. Med. Biol.*, vol. 59, no. 17, pp. 5119–5139, 2014.
- [59] Y. Lu, K. Yang, K. Zhou, Q. Zhang, B. Pang, and Q. Ren, “Development of a SiPM-based PET imaging system for small animals,” *Nucl. Instruments Methods Phys. Res. Sect. A Accel. Spectrometers, Detect. Assoc. Equip.*, vol. 743, pp. 30–38, 2014.
- [60] S. España, R. Marcinkowski, V. Keereman, S. Vandenberghe, and R. Van Holen, “DigiPET: sub-millimeter spatial resolution small-animal PET imaging using thin monolithic scintillators.,” *Phys. Med. Biol.*, vol. 59, no. 13, pp. 3405–20, 2014.
- [61] H. Philips, “See further. Go Beyond. Philips Vereos PET/CT brochure,” 2015.
- [62] G. El Fakhri, P. A. Santos, R. D. Badawi, C. H. Holdsworth, and A. D. Van Den Abbeele, “Impact of Acquisition Geometry , Image Processing , and Patient Size on Lesion Detection in Whole Body 18F-FDG PET,” *J. Nucl. Med.*, vol. 48, no. 12, pp. 1951–1960, 2007.
- [63] B. S. Halpern, M. Dahlbom, A. Quon, C. Schiepers, C. Waldherr, D. H. Silverman, O. Ratib, and J. Czernin, “Impact of Patient Weight and Emission Scan Duration on PET / CT Image Quality and Lesion Detectability,” *J. Nucl. Med.*, vol. 45, no. 5, pp. 797–801, 2004.
- [64] M. Tatsumi, P. A. Clark, Y. Nakamoto, and R. L. Wahl, “Original article Impact of body habitus on quantitative and qualitative image quality in whole-body FDG-PET,” *Eur. J. Nucl. Med. Mol. Imaging*, vol. 30, no. 1, pp. 40–45, 2003.
- [65] Y. Masuda, C. Kondo, Y. Matsuo, M. Uetani, and K. Kusakabe, “Comparison of Imaging Protocols for 18 F-FDG PET / CT in Overweight Patients : Optimizing Scan Duration Versus Administered Dose,” *J. Nucl. Med.*, vol. 50, no. 6, pp. 844–848, 2009.
- [66] Brisse, J. Herve, L. Madec, G. Gaboriaud, T. Lemoine, A. Savignoni, S. Neuenschwander, B. Aubert, and J.-C. Rosenwald, “Automatic exposure control in multichannel CT with tube current modulation to achieve a constant level of image noise : Experimental assessment on pediatric phantoms,” *Med. Phys.*, vol. 34, pp.

3018–3033, 2007.

- [67] D. Tack and P. A. Gevenois, *Radiation Dose from Adult and Pediatric Multidetector Computed Tomography*. Berlin Heidelberg: Springer, 2007.
- [68] M. K. Kalra, N. Naz, S. M. R. Rizzo, and M. A. Blake, “Computed Tomography Radiation Dose Optimization : Scanning Protocols and Clinical Applications of Automatic Exposure Control,” *Curr. Probl. Diagn. Radiol.*, vol. 34, no. October, pp. 171–181, 2005.
- [69] E. P. Visser, J. a Disselhorst, M. Brom, P. Laverman, M. Gotthardt, W. J. G. Oyen, and O. C. Boerman, “Spatial resolution and sensitivity of the Inveon small-animal PET scanner.,” *J. Nucl. Med.*, vol. 50, no. 1, pp. 139–147, 2009.
- [70] K. Magota, N. Kubo, Y. Kuge, K. I. Nishijima, S. Zhao, and N. Tamaki, “Performance characterization of the Inveon preclinical small-animal PET/SPECT/CT system for multimodality imaging,” *Eur. J. Nucl. Med. Mol. Imaging*, vol. 38, no. 4, pp. 742–752, 2011.
- [71] I. Szanda, J. Mackewn, G. Patay, P. Major, K. Sunassee, G. E. Mullen, G. Nemeth, Y. Haemisch, P. J. Blower, and P. K. Marsden, “National Electrical Manufacturers Association NU-4 Performance Evaluation of the PET Component of the NanoPET/CT Preclinical PET/CT Scanner,” *J. Nucl. Med.*, vol. 52, pp. 1741–1747, 2011.
- [72] Y. Wang, Z. Zhang, D. Li, B. Wang, L. Shuai, B. Feng, P. Chai, S. Liu, H. Tang, T. Li, Y. Liao, X. Huang, Y. Chen, Y. Liu, Y. Zhang, and L. Wei, “Design and performance evaluation of a compact , large-area PET detector module based on silicon photomultipliers,” *Nucl. Instruments Methods Phys. Res. A*, vol. 670, pp. 49–54, 2012.
- [73] P. E. Kinahan, D. W. Townsend, T. Beyer, and D. Sashin, “Attenuation correction for a combined 3D PET / CT scanner,” *Med. Phys.*, vol. 25, no. 10, pp. 2046–2053, 1998.
- [74] H. S. Yoon, G. B. Ko, S. I. Kwon, C. M. Lee, M. Ito, I. Chan Song, D. S. Lee, S. J. Hong, and J. S. Lee, “Initial Results of Simultaneous PET/MRI Experiments with an MRI-Compatible Silicon Photomultiplier PET Scanner,” *J. Nucl. Med.*, vol. 53, no. 4, pp. 608–614, 2012.
- [75] J. Wehner, B. Weissler, P. Dueppenbecker, P. Gebhardt, D. Schug, W. Ruetten, F. Kiessling, and V. Schulz, “PET/MRI insert using digital SiPMs: Investigation of MR-compatibility,” *Nucl. Instruments Methods Phys. Res. Sect. A Accel. Spectrometers, Detect. Assoc. Equip.*, vol. 734, no. PART B, pp. 116–121, 2014.

- [76] J. a Disselhorst, M. Brom, P. Laverman, C. H. Slump, O. C. Boerman, W. J. G. Oyen, M. Gotthardt, and E. P. Visser, “Image-quality assessment for several positron emitters using the NEMA NU 4-2008 standards in the Siemens Inveon small-animal PET scanner.,” *J. Nucl. Med.*, vol. 51, no. 4, pp. 610–617, 2010.
- [77] V. Keereman, R. Van Hoken, S. Vandenberghe, and C. Vanhove, “Temperature dependence of APD-based PET scanners,” *Med. Phys.*, vol. 40, no. 9, p. 092506, 2013.
- [78] E. Roncali and S. R. Cherry, “Application of silicon photomultipliers to positron emission tomography,” *Ann. Biomed. Eng.*, vol. 39, no. 4, pp. 1358–1377, 2011.

12. Online references

[http1] https://en.wikipedia.org/wiki/Positron_emission_tomography

[http2] http://www.nature.com/nrneurol/journal/v10/n1/fig_tab/nrneurol.2013.245_F3.html

[http3] <http://www.usa.philips.com/healthcare/product/HC882446/vereos-digital-pet-ct>

[http4] <https://minipetct.com/m3i>

[http5] <http://www.opengatecollaboration.org/>

[http6] http://depts.washington.edu/simset/html/news/news_index.html

[http7] <http://hpc.unideb.hu/>

13. List of publications that serve as the basis of this dissertation



UNIVERSITY OF DEBRECEN
UNIVERSITY AND NATIONAL LIBRARY



Candidate: Áron Krisztián Krizsán
Neptun ID: JQQZBK
Doctoral School: Doctoral School of Molecular Medicine

Registry number: DEENK/259/2015.PL
Subject: Ph.D. List of Publications

List of publications related to the dissertation

1. **Krizsán, Á.K.**, Lajtos, I., Dahlbom, M., Daver, F., Emri, M., Kis, S.A., Opposits, G., Pohubi, L., Pótári, N., Hegyesi, G., Kalinka, G., Gál, J., Imrek, J., Nagy, F., Valastyán, I., Király, B., Molnár, J., Sanfilippo, D., Balkay, L.: A Promising Future: Comparable Imaging Capability of MRI-Compatible Silicon Photomultiplier and Conventional Photosensor Preclinical PET Systems.
J. Nucl. Med. 56 (12), 1948-1953, 2015.
DOI: <http://dx.doi.org/10.2967/jnumed.115.157677>
IF:6.16 (2014)
2. **Krizsán, Á.K.**, Czernin, J., Balkay, L., Dahlbom, M.: Whole Body PET Imaging Using Variable Acquisition Times.
IEEE Trans. Nucl. Sci. 61 (1), 115-120, 2014.
DOI: <http://dx.doi.org/10.1109/NSSMIC.2011.6153747>
IF:1.283



Address: 1 Egyetem tér, Debrecen 4032, Hungary Postal address: Pf. 39. Debrecen 4010, Hungary
Tel.: +36 52 410 443 Fax: +36 52 512 900/63847 E-mail: publikaciok@lib.unideb.hu, Web: www.lib.unideb.hu

14. List of other publications



UNIVERSITY OF DEBRECEN
UNIVERSITY AND NATIONAL LIBRARY



List of other publications

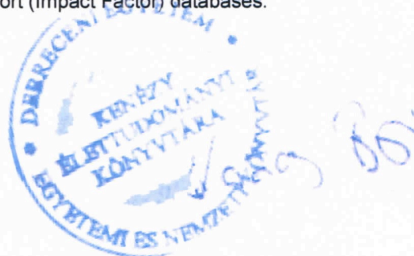
3. Balkay L., Emri M., **Krizsán Á.K.**, Opposits G., Varga J.: Újdonságok és új lehetőségek a funkcionális képképzésben: Leképezéstechnikai újdonságok.
Magyar Onkol. 59 (1), 4-9, 2015.
4. **Krizsán, Á.K.**, Varga, J., Forgács, A., Balkay, L.: Orvosi képképzés: Diagnosztika a képelemek mögött.
Fizikai Szle. 65 (3), 88-91, 2015.
5. Lajtos, I., Czernin, J., Dahlbom, M., Daver, F., Emri, M., Farshchi-Heydari, S., Forgács, A., Hoh, C.K., Jósza, I., **Krizsán, Á.K.**, Lantos, J., Major, P., Molnár, J., Opposits, G., Trón, L., Vera, D.R., Balkay, L.: Cold wall effect eliminating method to determine the contrast recovery coefficient for small animal PET scanners using the NEMA NU-4 image quality phantom.
Phys. Med. Biol. 59 (11), 2727-2746, 2014.
DOI: <http://dx.doi.org/10.1088/0031-9155/59/11/2727>
IF:2.761
6. Lajtos I., Emri M., Trón L., Kis S.A., Opposits G., Márián T., Trencsényi G., Mikecz P., Spisák T., **Krizsán Á.K.**: A debreceni kisállat PET program eredményei: A MiniPET-1, MiniPET-2 és a MiniPET-3 kamerák leképezési tulajdonságai.
IME. 12 (különszám), 33-38, 2013.

Total IF of journals (all publications): 10,204

Total IF of journals (publications related to the dissertation): 7,443

The Candidate's publication data submitted to the iDEa Tudóstér have been validated by DEENK on the basis of Web of Science, Scopus and Journal Citation Report (Impact Factor) databases.

11 December, 2015



Address: 1 Egyetem tér, Debrecen 4032, Hungary Postal address: Pf. 39. Debrecen 4010, Hungary
Tel.: +36 52 410 443 Fax: +36 52 512 900/63847 E-mail: publikaciok@lib.unideb.hu, Web: www.lib.unideb.hu

15. List of further publications and abstracts

2015

Nagy, G., **Krizsán, Á.K.**, Forgács, A., Szolik, M., Dahlbom, M., Balkay, L.: Image noise estimation using sub-reconstructions of clinical Whole Body PET/CT data. *Eur. J. Nucl. Med. Mol. Imaging* 42 (Suppl. 1), S372., 2015.

2014

Jonsson, H.P., Pap, L.D., Forgács, A., Nagy, V., Dahlbom, M., Opposits, G., **Krizsán, Á.K.**, Garai, I., Czernin, J., Balkay, L.: Validation of intensity based tumor heterogeneity parameters in human PET diagnostics (P077). *Eur. J. Nucl. Med. Mol. Imaging* 41 (S2), S380., 2014.

Krizsán, Á.K., Lajtos, I., Emri, M., Kis, S.A., Opposits, G., Hegyesi, G., Kalinka, G., Gál, J., Király, B., Imrek, J., Valastyán, I., Molnár, J., Sanfilippo, D., Dahlbom, M., Balkay, L.: Performance Comparison of SiPM and PMT Based Preclinical PET Systems with Same Detector Geometries (P004). *Eur. J. Nucl. Med. Mol. Imaging* 41 (S2), S360., 2014.

2013

Krizsán, Á.K., Forgács, A., Garai, I., Balkay, L.: Reliability study of the calculated textural parameters for heterogenic activity distribution in PET investigation using special designed phantom. *Eur. J. Nucl. Med. Mol. Imag* 40 (Suppl. 2), S407., 2013.

Balkay, L., Forgács, A., **Krizsán, Á.K.**, Lajtos, I., Lengyel, Z., Garai, I., Azeez, A.: Accreditation quality control performances of different PET scanners. *Nucl. Med. Rev. Cent. East. Eur* 16 (Suppl. A), A18., 2013.

Krizsán, Á.K., Szolik, M., Nagy, G., Dahlbom, M., Balkay, L.: Noise analysis of whole body FDG PET images. *Nucl. Med. Rev. Cent. East. Eur* 16 (Suppl. A), A17-A18., 2013.

Spisák, T., Opposits, G., Kis, S.A., Lajtos, I., **Krizsán, Á.K.**, Pohubi, L., Balkay, L., Emri, M.: BrainMOD: 4-dimensional multimodal medical image analysis software. In: Electronic presentation online system : ECR Congress 2013 / [ed. ESR], European Society of Radiology, [S. 1.], C-2586, 2013.

2012

Balkay, L., Oszlászki, A., **Krizsán, Á.K.**: Comparison of patient doses at different CT scanners with same acquisition protocol. *IEEE 2012* 3644-3645., 2012.

Krizsán, Á.K., Kis, S.A., Gál, J., Hegyesi, G., Balkay, L.: Simulation studies with SiPM arrays and LYSO crystal matrix analyzing a new readout scheme. In: *IEEE Nuclear Science Symposium and Medical Imaging Conference : 19th International Workshop on room-temperature semiconductor x-ray and gamma-ray detectors* / [ed. Nuclear and Plasma Sciences Society], Nuclear and Plasma Sciences Society, [S. l.], 205, 2012.

2011

Krizsán, Á.K., Czernin, J., Dahlbom, M.: Whole Body PET using variable acquisition times. *IEEE Trans. Nucl. Sci* M-200 1., 2011.

2008

Krizsán, Á.K., Füredi, A., Véső, T., Zalatnai, A., Valastyán, I., Balkay, L., Molnár, J., Molnár, J.: Effect of a new organosilicon multidrug resistance modifier on the metabolism of human pancreatic cancer xenografts: Positron emission tomography study (PO 255). In: *ICACT : Abstract Book : 19th International Congress of Anticancer treatment* / [ed. D. Khayat, G. N. Hortobagyi], [S. n.], [S. l.], 342-343, 2008.

16. Prints of publications that serve as the basis of this dissertation